Nanoscale Effects of Strontium on Calcite Growth: A Baseline for Understanding Biomineralization in the Absence of Vital Effects

Darren Scott Wilson

Thesis submitted to the Faculty of the Virginia Polytechnic Institute and State University in partial fulfillment of the requirements for the degree of

Master of Science
in
Geological Sciences

Patricia M. Dove, Chair

J. Donald Rimstidt

James. J. De Yoreo

May 8, 2003
Blacksburg, Virginia

Keywords: Biomineralization, Calcite, Strontium, Growth, Atomic Force Microscopy

Copyright 2003, Darren Scott Wilson

Nanoscale Effects of Strontium on Calcite Growth: A Baseline for Understanding Biomineralization in the Absence of Vital Effects

Darren Scott Wilson

(ABSTRACT)

This study uses in situ atomic force microscopy (AFM) to directly observe the atomic scale effects of Sr on the monomolecular layer growth of abiotic calcite. These insights are coupled with quantitative measurements of the kinetics and thermodynamics of growth to determine the direction-specific effects of Sr on the positive and negative surface coordination environments that characterize calcite step edges.

Low concentrations of strontium enhance calcite growth rate through changes in kinetics. A new conceptual model is introduced to explain this behavior. Higher concentrations of strontium inhibit and ultimately stop calcite growth by a step blocking mechanism. The critical supersaturation required to initiate growth (σ^*) increases with increasing levels of strontium. At higher supersaturations, strontium causes growth rates to increase to levels greater than those for the pure system. The step blocking model proposed by Cabrera and Vermilyea in 1958 does not predict the experimental data reported in this study because the dependence of σ^* upon strontium concentration is not the same for all supersaturations.

Strontium inhibits calcite growth by different mechanisms for positive and negative step directions. Preliminary evidence indicates that strontium is preferentially incorporated into the positive step directions suggesting that impurity concentrations are not homogeneous throughout the crystal structure. Despite geochemical similarities, this study demonstrates that strontium and magnesium have different surface interaction mechanisms.

The findings of this study demonstrate the importance of understanding microscopic processes and the significance of interpreting biominerals trace element signatures in the context of direction-specific interactions.

Acknowledgements

I would like to thank my advisor, Dr. Patricia Dove, for giving me the opportunity to work on this exciting research project. Her guidance and patience were remarkable throughout my graduate school experience. She has made the last two years of my life not only educational, but enjoyable as well.

I thank Dr. James J. De Yoreo for his contributions to this research. His knowledge and experience were incredibly useful for the completion of this work and he was a pleasure to work with.

Thanks to Dr. J. Donald Rimstidt for being an excellent professor and member of my committee. Your suggestions regarding this research as well as other issues were greatly appreciated.

I would also like to thank the members of my lab group, Meg Grantham, Nizhou Han, Mariano Velázquez and Laura Wasylenki whose ideas and shared experiences were invaluable.

A special thanks goes to my family for their love and support. They have always believed in me and made me feel that I could accomplish anything I set out to do. They have given me the opportunities to be successful throughout my life.

Thank you to my fiancée Amanda, for her love and friendship. I would not be where I am today without her. She truly is my better half, and I am incredibly lucky to have her in my life.

This study was supported by the NSF Division of Chemical Oceanography (OCE-0083173) and the DOE Office of Basic Energy Sciences, Division of Chemical Sciences, Geosciences, and Biosciences (FG02-00ER15112).

Table of Contents

Abstract **ii**

Acknowledgements **iii**

List of Tables **vi**

List of Figures **vii**

Chapter 1. Introduction to Biomineralization **1**

1.1 Background 1

1.2 Macroscopic Structure of Calcium Carbonate 3

1.3 Growth Hillocks (Microscopic Structure) 5

1.4 Trace Element Signatures 7

1.5 Strontium Interaction with Calcium Carbonate 10

1.6 Research Goals 14

Chapter 2. Materials and Experimental Procedures **15**

2.1 AFM Sample and Solution Preparation 15

2.2 AFM Solution Chemistry 16

2.3 Fluid Contact AFM Imaging 19

2.4 AFM Data Collection and Step Velocity Measurements 20

2.5 Long-term Growth Sample Preparation 23

2.6 Microprobe Analysis 25

Chapter 3. Experimental Results and Discussion **26**

3.1 Step Velocity Measurements 26

3.2 Crystal Growth Impurity Models 31

3.2.1 Step Blocking 31

3.2.2 Incorporation 34

3.2.3 Rate Enhancement 35

3.3 Step Velocity Measurements Revisited 37

3.4 Kinetic Coefficients 40

3.5 Terrace Widths 46

3.6 Hillock Morphology 50

3.7 Electron Probe Microanalysis (EPMA) 52

3.8 Modeling 55

Chapter 4. Conclusions **66**

References **69**

Appendix A. AFM Images of Calcite Growth Hillocks **72**

List of Tables

Table

2-1	Growth Solution Recipes	17
3-1	Step Velocity Data	27
3-2	Kinetic Coefficients	43
3-3	Terrace Widths	47
3-4	Microprobe Results of Strontium Concentrations	53
3-5	$\alpha B^{1/2} C_{Sr}^{1/2}$ for Positive Step Directions	58
3-6	Modeled Step Velocities for Positive Step Directions	60

List of Figures

Figure

1-1	Calcite Growth Hillock Structure	6
2-1	Supersaturation Conditions with Respect to Strontianite	18
2-2	Example of Image Used for Calculating Step Velocity	22
3-1	Step Velocities as a Function of Sr Concentration for Positive Steps	28
3-2	Step Velocities as a Function of Sr Concentration for Negative Steps	29
3-3	Crystal Growth Impurity Models	33
3-4	Step Velocities as a Function of σ Concentration for Positive Steps	38
3-5	Step Velocities as a Function of σ Concentration for Negative Steps	39
3-6	Slopes used to Determine β for Positive Step Directions	41
3-7	Slopes used to Determine β for Negative Step Directions	42
3-8	Kinetic Coefficients as a Function of Sr Concentration	44
3-9	Normalized Terrace Widths for Positive Step Directions	48
3-10	Normalized Terrace Widths for Negative Step Directions	49
3-11	Strontium and Magnesium Effects on Hillock Morphology	51
3-12	Graphical Microprobe Results of Strontium Concentrations	54
3-13	Modeled Step Velocity Plot for Positive Step Directions	61
3-14	σ^* as a Function of C_{Sr} for Positive Step Directions	62
3-15	σ^* as a Function of C_{Sr} for Negative Step Directions	63
3-16	Comparison of Modeled to Measured Step Velocities for + Directions	64
3-17	Comparison of Modeled to Measured Step Velocities for – Directions	65

Chapter 1

Introduction to Biomineralization

1.1 Background

Biomineralization is the process by which organisms precipitate minerals of inorganic-based materials. Over 60 different types of minerals with biological origins are known (Lowenstam and Weiner, 1989). Of the many essential elements required by living organisms, calcium is the most common of those found in biological minerals. For example, familiar skeletal structures such as shells are built from calcium carbonate whereas the bones of higher organisms are composed of calcium phosphate. A closer look reveals that the biomineralization of calcium carbonate is found across many forms of life from the cell wall scales of coccolithophores to the inner ears of mammals (Mann, 2001). These diverse structures are formed by a wide variety of organisms that utilize substantially different biological processes to result in polymorphs of $CaCO_3$ with distinctive mineralogies and compositions (Morse and Mackenzie, 1990).

Organisms have evolved the ability to direct the formation of minerals into morphologies not naturally found in their inorganically derived counterparts. The resulting biominerals have specific functions and often exhibit remarkable properties. For example, the individual segments of *E. huxleyi* are single calcite crystals with unusual morphologies. An example of a specific function is to provide mechanical strength to skeletal hard parts and teeth (Lowenstam and Weiner, 1989). These unique processes and

products of biomineralization are of interest throughout many scientific disciplines from biogeochemistry and sedimentology to materials and dentistry.

Some biogenic minerals are formed on a large scale in the biosphere to the extent that they have a major impact on ocean chemistry (Lowenstam and Weiner, 1989). In the surface ocean, mineralization of calcium carbonate by microorganisms is one example of an extensive process that influences seawater chemistry. Although much of the mineral product is dissolved and biologically recycled in the water column, a small portion accumulates as sediment on the ocean floor. Over time, this material becomes a significant fraction of the total amount of marine sediments.

Recently, the compositions of biominerals have become the subject of much interest because of their use as a proxy to interpret paleoenvironments. Previous studies have shown that the form and chemistry of biogenic carbonates are affected by environmental factors, such as temperature, salinity, water turbidity, and dissolved oxygen. These environmental conditions are believed to be reflected in biogenic carbonates through effects on trace component concentrations, stable isotope ratios and mineralogy. In recent years, the trace component and stable isotope chemistries have received the most attention as proxies of paleotemperature in climate reconstruction studies (Morse and Mackenzie, 1990).

1.2 Macroscopic Structure of Calcium Carbonate

Before there can be a detailed discussion of biogenic calcium carbonates, it is appropriate to first explore the structure and crystal chemistry of abiotic $CaCO_3$. Calcite can be considered a framework of carbonate (CO_3) anions that create sites into which calcium cations fit. Calcite is rhombohedral with the point group $\bar{3}2/m$ and space group $R\bar{3}c$. The structure can be derived from the NaCl structure in which CO_3 groups replace the Cl, and Ca is in place of Na. The triangular shape of the carbonate group causes the rhombohedral configuration instead of isometric as found for halite. The plane of CO_3 groups is perpendicular to the 3-fold *c*-axis. Consecutive carbonate layers are offset with respect to the carbon, giving rise to a cubic close packing arrangement, repeating positions every third layer. The corners of the triangular carbonate groups alternate every layer by a mirror plane, therefore, duplicate layers repeat only every sixth layer. As a result, the unit cell is six carbonate layers thick, which leads to a *c*-axis dimension 17.06 Å, while the two *a*-axes are only 4.99 Å. The Ca^{2+}, in alternate planes, are in 6-coordination (occupy octahedral sites) with the oxygens of the CO_3 groups. Each oxygen is coordinated to two Ca^{2+} cations as well as a C at the center of the carbonate group (Reeder, 1983)

Examining the layered structure of calcite, one might expect cleavage to occur between the layers of CO_3 groups. However, the bonding from the CO_3 to the Ca^{2+} is significantly stronger than bonds between CO_3 groups within their layer. Due to the fact that consecutive carbonate layers are offset with respect to the carbon, the cleavage is

inclined to the *c*-axis. The three cleavage directions form a rhomb with its surfaces parallel to the three edges of the CO_3 groups.

The rhombohedral cleavage has traditionally been given the indices {101}. Following that convention, a *c*-axis dimension of 1/4 the length actually measured in X-ray diffraction studies is required. Based on the correct unit cell dimensions, the Miller indices should be reassigned as {104} as the index for cleavage. However, this is not done because it would create inconsistencies in literature from different sources.

The strontium carbonate, strontianite ($SrCO_3$), has the orthorhombic structure of the other common polymorph of $CaCO_3$, aragonite. The structure of the orthorhombic carbonates can be described as layers of pseudohexagonally arranged metal atoms parallel to (001) with an ABA layer sequence along *c*. The metal layers are separated by layers of CO_3 groups, which have pseudohexagonal arrangement in the *ab* plane. There are two distinct layers of CO_3 groups, which are "corrugated" because of differing heights along *c*. Each CO_3 group is surrounded by six metal atoms, and each metal has nine nearest oxygen neighbors (Speer, 1983).

1.3 Growth Hillocks (Microscopic Structure)

Scanning probe microscopy has opened the door to quantifying the fundamental material properties and dynamic behaviors of surfaces that were previously immeasurable, including high-resolution imaging of crystal growth at Angstrom scales. The detailed interactions of step edges on crystal surfaces with solutes in aqueous solutions are important in controlling growth rate and morphology. Real-time observations and measurements can be made to directly test the BCF (Burton, Cabrera and Frank) theories of crystal growth (Burton et al., 1951). Of special interest is the spiral growth mechanism, which occurs on crystal surfaces at near equilibrium, by the advancement of monomolecular steps nucleated at screw dislocations. More generally is the process of layer growth when individual steps advance by addition of material at energetically favorable kinks (Gratz et al., 1993).

Calcite pyramids, or "hillocks" develop during spiral growth when 3.1Å monomolecular risers of steps oriented parallel to the edges $[\bar{4}41]$ and $[48\bar{1}]$ flow outward from their dislocation source. The resulting growth hillock features express the anisotropy of the calcite crystal structure (Figure 1-1). Two pairs of crystallographically equivalent step directions show kink site-specific surface structures. Obtuse (positive) and acute (negative) step-edge geometries are caused by the tilt of CO_3 groups, which leads to distinct environments that exhibit different reactivity. Along the positive step directions, the calcite surface has larger and geometrically more open kink sites compared to the smaller and more shielded sites along negative directions.

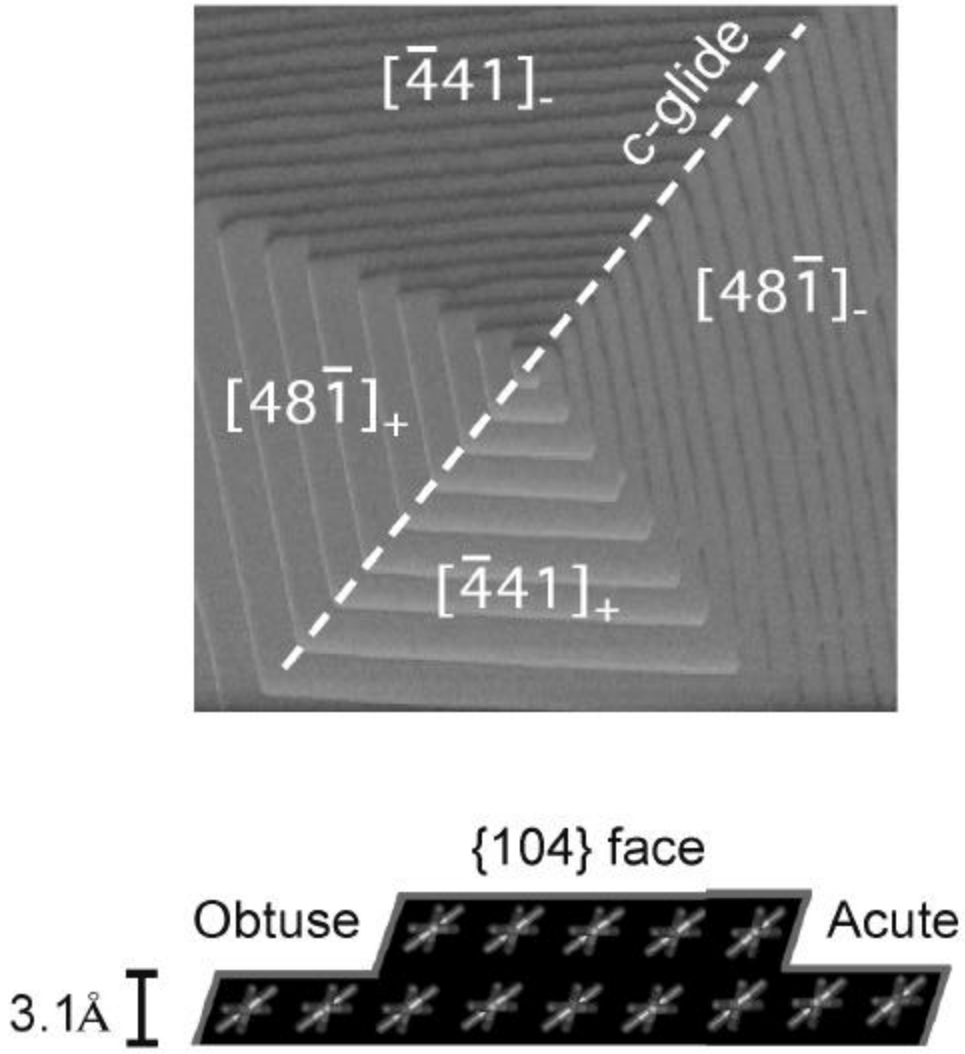

Figure 1-1 Example of calcite growth hillock showing two pairs of crystallographically equivalent step directions (above) and a cross-sectional view (below) showing the difference between obtuse and acute kink-site environments (from Davis *et al.*, submitted).

1.4 Trace Element Signatures

Now that a basic understanding of both the macro and microscopic structures of $CaCO_3$ has been presented, attention is now be given to biominerals. Natural carbonate minerals form in the aqueous solutions of terrestrial and marine environments. These fluids contain a number of dissolved constituents that can be incorporated into the solid at trace to minor concentrations. Trace element studies have been largely confined to cations, with strontium in aragonitic corals receiving the most attention (Morse and Mackenzie, 1990). The incorporation of cations with smaller radii than calcium are believed to be favored in calcite and those larger than calcium are favored in aragonite. However, Mg^{2+}, Sr^{2+} and several other cations with both larger and smaller radii than Ca^{2+} can be accommodated in various amounts in the crystal structure of calcite (Lea, 1999; Reeder, 1983; Mucci & Morse, 1983).

In recent years, numerous coprecipitation studies have investigated the interaction of a wide variety of ions and compounds with calcite (Elderfield et al., 1996; Reeder, 1996; Rosenthal et al., 1997; Rathburn & Deckker, 1997; Stoll et al., 2002; De Leeuw et al., 2002). In particular, the strontium and magnesium contents in biogenic calcite have received considerable attention in the earth sciences as probable robust proxies of paleotemperature. Results of these studies have demonstrated the complexity of the processes involved and need for a more detailed knowledge of the mechanisms involved in carbonate biomineral formation (Morse and Mackenzie, 1990).

Of the *minor* dissolved elements found in seawater, strontium has been the most thoroughly investigated impurity in calcite and aragonite (Morse and Mackenzie, 1990).

The average concentration of strontium in the oceans is 8 ppm, which is quite low compared to average levels of major constituents such as Mg^{2+} (1,350 ppm) and Ca^{2+} (400 ppm) (Berner and Berner, 1996).

Attempts to infer the seawater Sr/Ca ratio from that of biogenic calcite rest in the assumption that the Sr/Ca ratio in calcite is proportional to the Sr/Ca ratio in seawater. This assumption is supported by the following arguments. First, the Sr partition coefficient, D_{Sr} (= $(Sr/Ca)_{calcite}$ / $(Sr/Ca)_{seawater}$) in biogenic calcite is relatively constant, about 0.16 +/- 0.02, for a variety of organisms including mollusks, coccolithophorids and foraminifera. Second, this value of the partition coefficient is found over a wide range of solution Sr/Ca, Mg/Ca and Na/Ca ratios. Finally, the empirical biogenic partition coefficient of 0.16 is close to the inorganic distribution coefficient determined experimentally for high $CaCO_3$ precipitation rates (characteristic of biogenic calcite) in dilute solutions (Graham et al., 1982).

Although chemical principles are fundamental to the controls on incorporation of trace elements into calcite, these processes cannot be adequately described using equilibrium thermodynamics. Active biomineral precipitation by organisms affects both its structure and chemistry suggesting additional kinetic controls on trace element substitution (Lea, 1999). The complex biological processes that influence the formation of skeletal materials are termed ‘vital effects’. Given the growing number of parameters such as temperature, reaction rate, solution composition, and vital effects, which have been found to exert major influences on partition coefficients of metals in calcite, variables to interpret natural systems should be applied with considerable caution.

Partition coefficients are not equivalent to thermodynamic constants and generally represent measurements under a given set of conditions (Morse and Bender, 1990).

1.5 Strontium Interaction with Calcium Carbonates

Strontium is a conservative element in seawater with a long residence time of about 5 My. Therefore, the ratio of Sr/Ca is nearly fixed in seawater. Sr/Ca is much more uniform than Mg/Ca in planktonic foraminifera, varying from about 1.2 to 1.6 mmol/mol. Sr occurs at levels up to 0.25% by weight in foraminifer shells (1-2 x 10^{-3} mol/mol Ca) making it a minor element (Lea, 1999). Investigation using XANES and EXAFS show that strontium is incorporated in calcite by substitution at Ca^{2+} structural sites, forming a dilute solid solution (Pingitore et al., 1992). These techniques further eliminate such modes of incorporation as adsorption, occlusion, and the presence of trace amounts of strontianite or other Sr-rich phases.

The growth rate of calcite can be significantly inhibited by impurities, many of which can have a substantial effect at very low concentrations. Berner (1975), Reddy and Wang (1980), Mucci and Morse (1983), and Davis et al. (2000) state that Mg^{2+} strongly inhibits precipitation. Meyer (1984), showed that a strontium concentration of 1 x 10^{-5} mol/L reduced the growth rate of calcite by 20%.

The Sr/Ca ratios in biomineral $CaCO_3$ have been regarded as more reliable than $\delta^{18}O$ values as a proxy for paleotemperature because they are less affected by salinity or polar ice volume. It was argued by Purton et al. (1999), however, that vital effects can exert a greater control than paleotemperature over fossil Sr/Ca. Measurements of Sr/Ca increased through the origin and development of the Eocene bivalve *Venericardia planicosta* suggesting that more Sr was incorporated as growth rate slowed rather than as a result in changing paleotemperature. Sr/Ca data from the marine gastropod *Clavilithes*

macrospira, which exhibits a linear growth rate through ontogeny, also showed a significant increase in Sr concentration with age as well as seasonal, possibly temperature-related variations. Therefore, neither growth rate, calcification rate, nor temperature can be the sole factor controlling Sr incorporation. It was concluded that metabolic activity, related to factors such as temperature, salinity, age, and growth rate, were likely to exert the primary control over Sr/Ca ratios.

A number of studies have investigated the relationship between growth rates and the strontium contents of calcium carbonates. Tesoriero & Pankow (1996), stated that for precipitation rates (R) greater than 30 nmols/mg-min, the Sr partition coefficient (D_{Sr}) increased with R. For R<30 nmols/mg-min, D_{Sr} remained nearly constant. It was estimated that the miscibility limit for strontianite in calcite occurred at a mole fraction of about 0.0035. According to a study by Mucci & Morse (1983), the concentration of Sr incorporated within calcite overgrowths precipitated from seawater and related solutions were independent of the precipitation rate or the saturation state of the solution. The concentration of $SrCO_3$ incorporated in the overgrowths were linearly related to the $MgCO_3$ content of the overgrowths, and was attributed to increased solubility of $SrCO_3$ in calcite due to the incorporation of the smaller Mg^{2+} ions. It was suggested that the addition of Sr^{2+} in the calcite crystal lattice may have relieved some of the stress caused by the incorporation of Mg^{2+} and consequently partially compensated for the destabilizing effect of magnesium.

The role of step-edge geometry in controlling the strontium levels that are incorporated into calcite has been found important. Due to the difference in positive and negative step-edge geometries in calcite, a larger amount of strontium will become

incorporated into the positive flanks of a hillock. Paquette and Reeder (1995) said that the magnitude of the partitioning difference for Sr into the positive sites over the negative sites is nearly always less than a factor of two and more commonly a factor of 1.2 – 1.4. A published data set showed that Sr incorporation was about 1200 ppm on a negative flank compared to about 2400 ppm on a positive flank. A later study that used similar methods to Paquette and Reeder (1995) included an experiment which showed that Sr incorporation was about 1800 ppm on a negative flank compared to about 3750 ppm on a positive flank (Reeder, 1996).

In contrast with work showing that ion size (relative to host Ca) controls the preference of ions between surface sites of different size and geometry, other studies suggest more complex influences. For example, the smaller zinc ion exhibits step-specific preferences similar to those of the larger ions Ba and Sr, which may reflect its strong association with ligands such as chloride or nitrate in solution or a particular interaction with surface sites (Reeder 1996).

Theoretical methods have also been used to probe the roles of step geometry on strontium levels in calcite. The molecular dynamics simulations conducted by De Leeuw et al. (2002), modeled the incorporation of strontium ions at $(10\bar{1}4)$ calcite surfaces. Growth of a row of $SrCO_3$ occurring at the acute edges was said to release a large amount of energy (-420 kJ/mol), which they proposed should be the preferential step direction for incorporation of complete $SrCO_3$ edges. On the basis of cation size Leeuw et al. predicted that the larger Sr^{2+} ion was preferentially incorporated at the obtuse step edge, where the cation sites are less enclosed and, therefore, more accessible to the larger ions. However, the model calculations show that even initial growth of $SrCO_3$ was exothermic for both

step directions, with especially large energies released upon incorporation at the acute step edge. However, the calculations were based upon a physical model that considered only a row of $SrCO_3$ forming a new step edge rather than the incorporation of Sr^{2+} into an existing kink. It was concluded that additional detailed calculations on the incorporation at kink sites were necessary for a more complete theoretical model.

1.6 Research Goals

This study quantifies the kinetics and thermodynamics of calcite growth in the presence of Sr^{2+} to determine the mechanisms by which strontium influences $CaCO_3$ mineralization. Monomolecular step migration rates are measured using in-situ Atomic Force Microscopy. These data are evaluated using crystal growth impurity models. Kinetic coefficients are calculated and terrace widths are measured for additional insight into growth mechanisms.

This study also quantifies the effect of Sr^{2+} on the morphology of $CaCO_3$ growth hillocks by determining the kink site-specific interactions of strontium with calcite. Microprobe analysis of calcite hillocks grown in solutions of carefully chosen supersaturations and strontium levels are conducted to determine trace element concentrations at different positions within a hillock.

The findings from this study show the microscopic role of strontium in modifying calcite growth. The behavior of this minor seawater solute provides a baseline of knowledge that is essential to developing a comprehensive model of biogenic calcite growth.

Chapter 2

Materials and Experimental Procedures

2.1 AFM Sample and Solution Preparation

To obtain a calcite surface substrate for the growth experiments, fragments of approximately 2 x 2 x 0.5 mm in size were cleaved along {104} faces from laboratory specimens of calcite. Crystals used in these experiments were from Ward's Natural Science. These crystals were handled with tweezers to avoid surface contamination and were subjected to quick bursts of nitrogen gas to remove any small particles from the surfaces. The freshly cleaved sample was mounted to an acid-washed glass cover slip using sealing wax. The cover slip was thereafter mounted to a magnetic steel puck again using sealing wax. The fragments were observed at approximately 466x magnification to ensure a flat, smooth surface suitable to be used as a substrate for growth.

Solutions that were supersaturated with respect to $CaCO_3$ were prepared by dissolving high-purity sodium bicarbonate (99.99%) and calcium chloride dihydrate (99.99%) into distilled and deionized water. The ionic strength of the solutions was fixed to approximately 0.1 M using ultra high-purity NaCl (99.999%). When Sr^{2+} was desired in the system, high-purity strontium chloride hexahydrate (99.995%) was added to the solutions as well. All reagents were obtained from Sigma-Aldrich, Inc. The pH of the solutions was adjusted to approximately 8.5 using 1.005 N NaOH just prior to transfer into 60 ml polypropylene syringes to be injected into a fluid cell of an AFM at ambient temperature.

2.2 AFM Solution Chemistry

The chemical speciation of each growth solution was determined using the computer software package, *Geochemist's Workbench*, assuming that the AFM flow-through set-up approximated a closed system. The supersaturation, σ, was calculated by:

$$s = \ln\left(\frac{a_{Ca^{2+}} a_{CO_3^{2-}}}{K_{sp}}\right)$$

(Eqn. 2.1)

where $a_{Ca^{2+}}$ and $a_{CO_3^{2-}}$ are the actual activities of the Ca^{2+} and CO_3^{2-} ionic species, and K_{sp} is the solubility product of pure calcite at zero ionic strength. All of the growth solutions used chemistries that set the activity ratio of Ca^{2+} to CO_3^{2-} to near unity (1.0 ± 0.085) by adjusting the amounts of sodium bicarbonate and calcium chloride dihydrate. The Plummer and Busenberg (1982) value of $10^{-8.48}$ for K_{sp} at 25°C was used. In this study, the solution supersaturations were varied from 0.55 to 1.16 using the solution compositions and activities presented in Table 2-1. Sr^{2+} concentrations ranged from 0 to 3 x 10^{-4} m. Figure 2-1 is a graphical representation of the range of supersaturation conditions with respect to strontianite at each calcite supersaturation level.

Table 2-1 Summary of salt concentrations (m = mol/kg) used in each growth experiment and the corresponding solute activities and supersaturations.

Solution	$[CaCl_2]$ (m)	$[NaHCO_3]$ (m)	[NaCl] (m)	Activity (Ca^{2+})	Activity (CO_3^{2-})	S	Range of C^{Sr} (m)
1	2.45×10^{-4}	7.45×10^{-3}	0.10	7.56×10^{-5}	7.62×10^{-5}	0.55	$0 – 4.50 \times 10^{-5}$
2	2.60×10^{-4}	7.85×10^{-3}	0.10	7.99×10^{-5}	8.02×10^{-5}	0.66	$0 – 1.80 \times 10^{-4}$
3	2.75×10^{-4}	8.25×10^{-3}	0.10	8.41×10^{-5}	8.43×10^{-5}	0.76	$0 – 2.25 \times 10^{-4}$
4	3.00×10^{-4}	9.00×10^{-3}	0.10	9.10×10^{-5}	9.18×10^{-5}	0.93	$0 – 3.00 \times 10^{-5}$
5	3.42×10^{-4}	10.10×10^{-3}	0.10	10.24×10^{-5}	10.28×10^{-5}	1.16	$0 – 3.00 \times 10^{-5}$

Figure 2-1 Range of supersaturation conditions with respect to strontianite at each calcite supersaturation level. Diagram shows that most experiments were supersaturated with respect to $SrCO_3$.

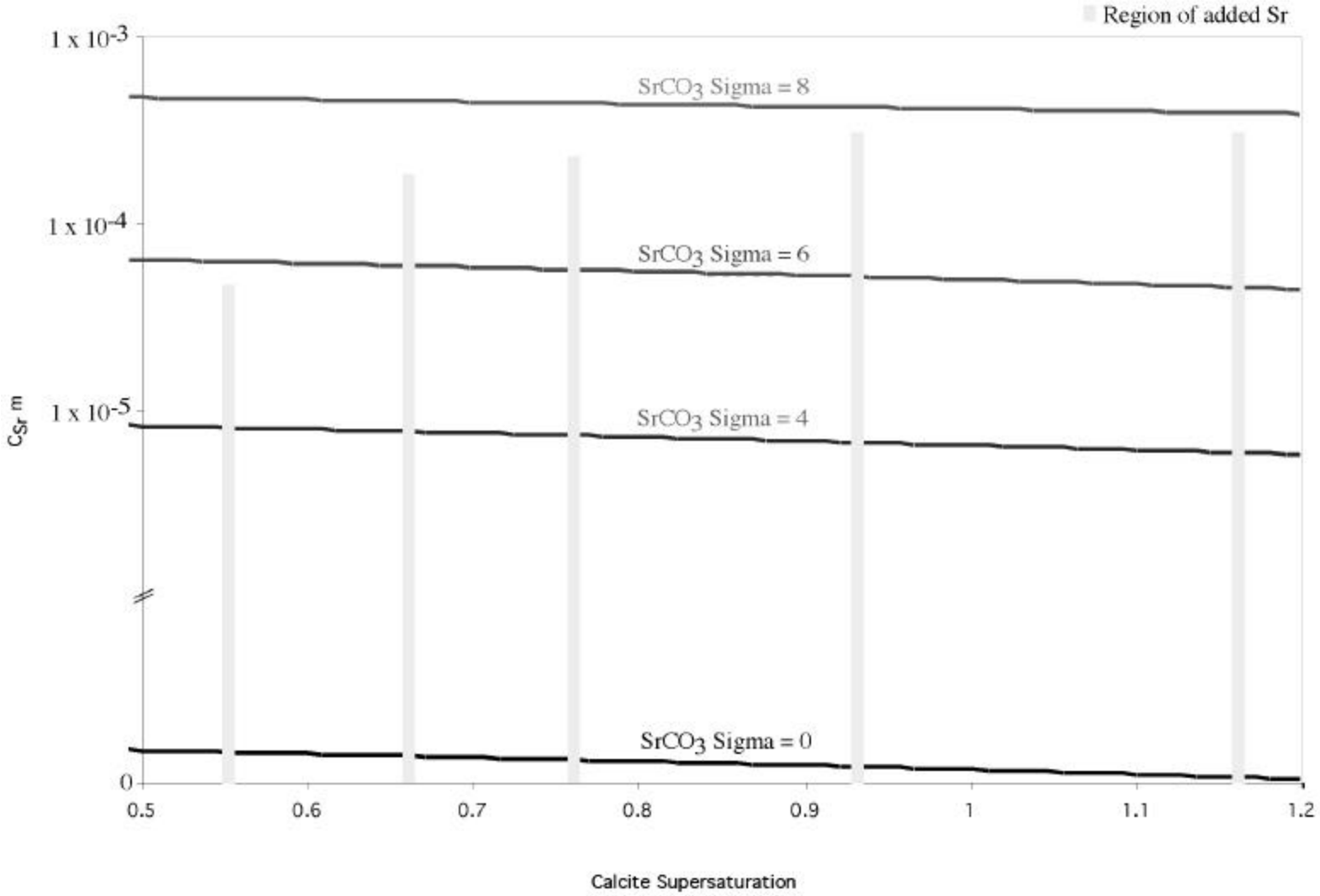

2.3 Fluid Contact AFM Imaging

Observations of calcite growth were made in situ using a Nanoscope® IIIa AFM equipped with a piezoelectric scanner with the ability to raster over areas as large as 120 x 120 μm. A magnetic puck containing the sample rested on top of the piezoelectric scanner. Surfaces were imaged using Si_3N_4 cantilevers attached to the AFM fluid cell, which was mounted over the sample. An o-ring sealed the fluid cell compartment creating a 50 μL volume for solution interaction with the sample. A syringe pump running at 30 mL/hr forced solutions through the fluid cell compartment such that the average residence time of fluid in the cell was approximately 6 seconds assuming ideal mixing. Step velocities are independent of flow rate at 30 mL/hr (Teng et al., 2000), thus ensuring that growth was not limited by mass transport to the surface. Images were collected after at least 45 minutes of initial contact with solution to ensure steady state of the system in addition to observations of constant step edge structures and velocities over time.

2.4 AFM Data Collection and Step Velocity Measurements

The AFM experiments were conducted by first locating a spiral hillock and allowing the step velocities to reach a steady state for a given solution composition. The scan angle was adjusted to orient the step train parallel to the y-axis. The y-axis scan direction was disabled when the cantilever had reached the hillock apex. A minimum of four images with the y-axis scan direction disabled were collected for each growth solution, along with an image of the hillock with both scan directions enabled for later analysis. In order to reduce the possibility of artificial changes in hillock microtopography by tip-surface interactions, the interactive force was minimized by reducing the setpoint value as much as possible, without disengaging the tip. There were 512 sampling points per scan line and scan rates ranged from 1 to 5 Hz depending on the step advancement velocity.

Measurements of step velocity, ν_{s+} and ν_{s-}, were made for the positive and negative directions. Step velocities were determined by measuring step displacement over time using the images collected with the y-axis scan direction disabled. These images recorded the movement of steps as the evolution of individual points at step edges over the imaging area as shown in Figure 2-2. Using the measured angle ϖ, ν_s was calculated on both sides of the hillock using the equation:

$$n_s = \frac{S_r \times A}{N \times \tan \nu}$$

(Eqn. 2.2)

where S_r is the scan rate (lines/second), A the scan size, and N the sampling rate (lines/scan, 512 in this study).

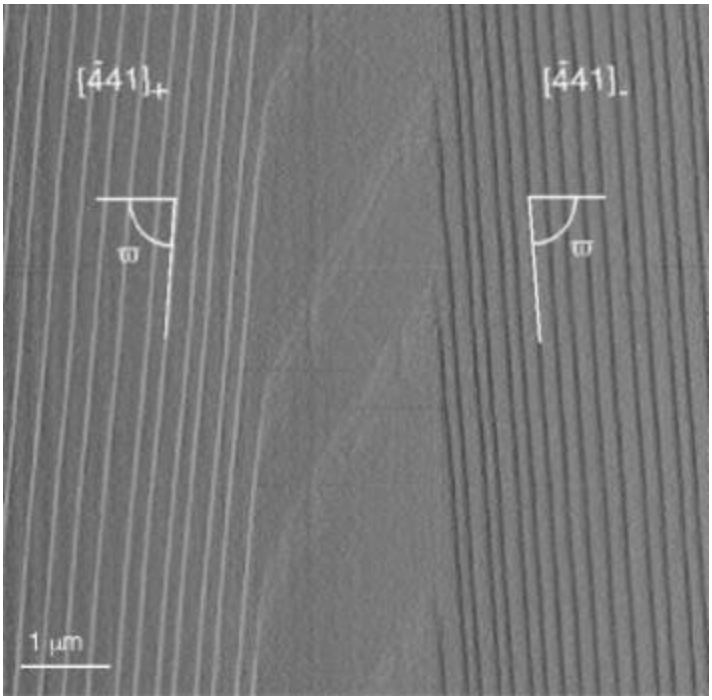

Figure 2-2 AFM image of spiral hillock on calcite surface with the slow scanning direction disabled across the apex. The angle formed by the step train and y-axis, designated by ϖ, was measured at both sides to estimate the step velocities for the positive and negative directions (from Teng, 2000).

2.5 Long-term Growth Sample Preparation

To conduct the long-term growth experiments, fragments of approximately 2 x 2 x 0.5 mm in size were cleaved along {104} faces from laboratory specimens of calcite to serve as seeds for crystallization. These crystals were handled with tweezers to avoid surface contamination and were subject to quick bursts of nitrogen gas to remove any small particles from the surfaces. The fragments were observed at approximately 466x magnification to ensure a flat, smooth surface suitable to be used as a substrate for growth. The freshly cleaved sample was placed in a fluid cell identical to the AFM fluid cell, but without the imaging equipment. To stimulate the formation of hillocks, the experiment began by flowing a growth solution with a supersaturation of approximately $\sigma = 2$ through the simulated fluid cell compartment for 12 hours at 30 mL/hr. A freshly made, supersaturated growth solution was introduced and pumped through for an additional 12 hours. The samples were again observed at approximately 466x magnification while still in the fluid cell to confirm the growth of hillocks.

The crystal fragments were removed from the acrylic chambers with tweezers and transferred into acid-washed 2 x 2 cm bags of fine nylon mesh. The nylon bags containing the calcite fragments were then transferred into 250-mL volumetric flasks. The flasks were filled with approximately 200 mL of selected growth solutions identical to those in table 2-1 used for AFM experiments. The flasks were placed on a shaker table and were stirred at 125 rpm inside an incubator at 23.3^{o}C to approximate the ambient temperature of the AFM experiments.

Every 12 hours for 10 days, flasks were removed from the shaker table to replace the growth solutions with fresh ones. After samples were submersed in growth solutions for 120 hours, the nylon bags were removed from the flasks. The bags were cut open and the samples removed with tweezers and rested on a glass slide. The corner of the calcite fragment was touched with a Kimwipe to remove any solution that was on the surface.

2.6 Microprobe Analysis

Calcite samples were mounted on a glass slide using cyanoacrylate glue and coated with approximately 200-250 Å of carbon to prepare for electron microprobe analysis. Concentrations of strontium were determined using a Cameca SX-50 electron microprobe in the Department of Geological Sciences at Virginia Tech. A grid of approximately 60 x 60 microns was selected around a calcite hillock for spot analyses at 4 micron intervals. An analysis was performed for Ca, Mg, Mn and Sr using an accelerating voltage of 15 kV with a beam current of 5 nA. The count time for strontium was 100 seconds and all other count times were a minimum of 20 seconds. High and low backgrounds were counted for 20 seconds each on every point for strontium and 10 seconds each for other elements. Synthetic $SrCO_3$ was analyzed as a standard for strontium at 15 kV and 20 nA. Data reduction is based on the methods of Pouchou and Pichoir (1985).

Chapter 3

Experimental Results and Discussion

3.1 Step Velocity Measurements

Step velocities (v_s) of calcite growth hillocks were measured for positive and negative step directions as described by the methods in section 2.4. These were collected using five supersaturations (σ = 0.55, 0.66, 0.76, 0.93 and 1.16) across a range of strontium concentrations including a control of $C_{Sr} = 0$ to a maximum of 3×10^{-4} m.

A summary of step velocity data as a function of supersaturation and strontium concentration is presented in Table 3-1. Figures 3-1 and 3-2 show graphical representations of step velocities as a function of strontium concentration at constant supersaturation for the positive and negative step directions, respectively. The AFM images of the growth hillocks that were used to determine these step velocity measurements are found in Appendix A.

In the absence of strontium, step velocities for the positive direction were greater than for the negative direction at a given supersaturation. In addition, step velocities increased with increasing supersaturation. These observations are consistent with the findings of Davis, 2000.

In this investigation, we find that there is a rate *enhancing* effect with the addition of low concentrations of strontium to the system. This rate enhancement may occur through changes in thermodynamics by forming a solid solution with strontium to yield a

Table 3-1 Summary of step velocity data as a function of supersaturation and strontium concentration. Numbered images can be found in Appendix A.

Sigma	Date	C_{Sr} (m)	n_+ (nm/s)	n_- (nm/s)	Hillock #	Image #
1.16	10/16/02	0	12.38	5.98	1	10161309
1.16	10/17/02	0	13.03	6.95	3	10171153
1.16	10/22/02	0	13.98	6.98	6	10221357
1.16	10/16/02	9.89×10^{-5}	17.21	9.05	1	10161403
1.16	10/17/02	1.50×10^{-4}	15.92	11.94	4	10171249
1.16	10/16/02	1.98×10^{-4}	15.83	11.10	1	10161504
1.16	10/17/02	2.25×10^{-4}	15.73	14.58	5	---
1.16	3/26/03	2.55×10^{-4}	14.65	10.68	7	03261357
1.16	10/16/02	3.00×10^{-4}	13.07	9.94	2	10161607
1.16	3/26/03	3.00×10^{-4}	15.34	12.89	8	03261450
0.93	11/16/02	0	10.76	4.75	9	11161333
0.93	12/27/02	0	9.89	4.72	10	12271141
0.93	11/16/02	8.99×10^{-5}	10.44	6.32	9	11161420
0.93	11/16/02	1.80×10^{-4}	10.74	7.65	9	11161506
0.93	12/27/02	2.40×10^{-4}	9.31	7.24	10	12271235
0.93	12/27/02	2.70×10^{-4}	7.66	7.43	10	12271331
0.93	12/27/02	3.00×10^{-4}	0.45	2.80	10	12271433
0.76	10/29/02	0	8.17	5.49	11	10291502
0.76	10/29/02	3.00×10^{-5}	8.13	5.92	11	10291600
0.76	10/29/02	6.00×10^{-5}	8.82	6.64	11	10291653
0.76	10/30/02	8.99×10^{-5}	8.92	6.16	12	10301356
0.76	10/30/02	1.20×10^{-4}	9.51	7.84	12	10301454
0.76	10/30/02	1.50×10^{-4}	8.85	7.80	12	10301546
0.76	10/30/02	1.80×10^{-4}	7.42	7.90	12	10301644
0.76	10/31/02	1.80×10^{-4}	8.43	6.77	13	10311515
0.76	10/31/02	1.95×10^{-4}	7.78	7.58	13	10311555
0.76	10/30/02	2.10×10^{-4}	6.16	7.24	12	10301746
0.76	10/31/02	2.10×10^{-4}	0.78	3.38	13	10311652
0.76	10/31/02	2.25×10^{-4}	0.09	0.92	14	10311805
0.66	1/2/03	0	7.57	3.91	15	01021234
0.66	1/2/03	3.00×10^{-5}	7.28	4.87	15	01021328
0.66	1/2/03	6.00×10^{-5}	7.93	4.50	15	01021421
0.66	1/2/03	8.99×10^{-5}	7.38	5.22	15	01021512
0.66	1/2/03	1.20×10^{-4}	8.62	5.11	15	01021610
0.66	1/2/03	1.50×10^{-4}	5.60	4.70	15	01021702
0.66	1/2/03	1.80×10^{-4}	0.31	2.03	15	01021819
0.55	11/8/02	0	4.41	4.09	16	11081528
0.55	11/9/02	0	4.59	3.30	18	11091439
0.55	11/8/02	3.00×10^{-5}	1.51	1.83	17	11081650
0.55	11/9/02	3.00×10^{-5}	4.75	4.18	18	11091534
0.55	11/9/02	4.50×10^{-5}	0.06	0.57	18	11091641

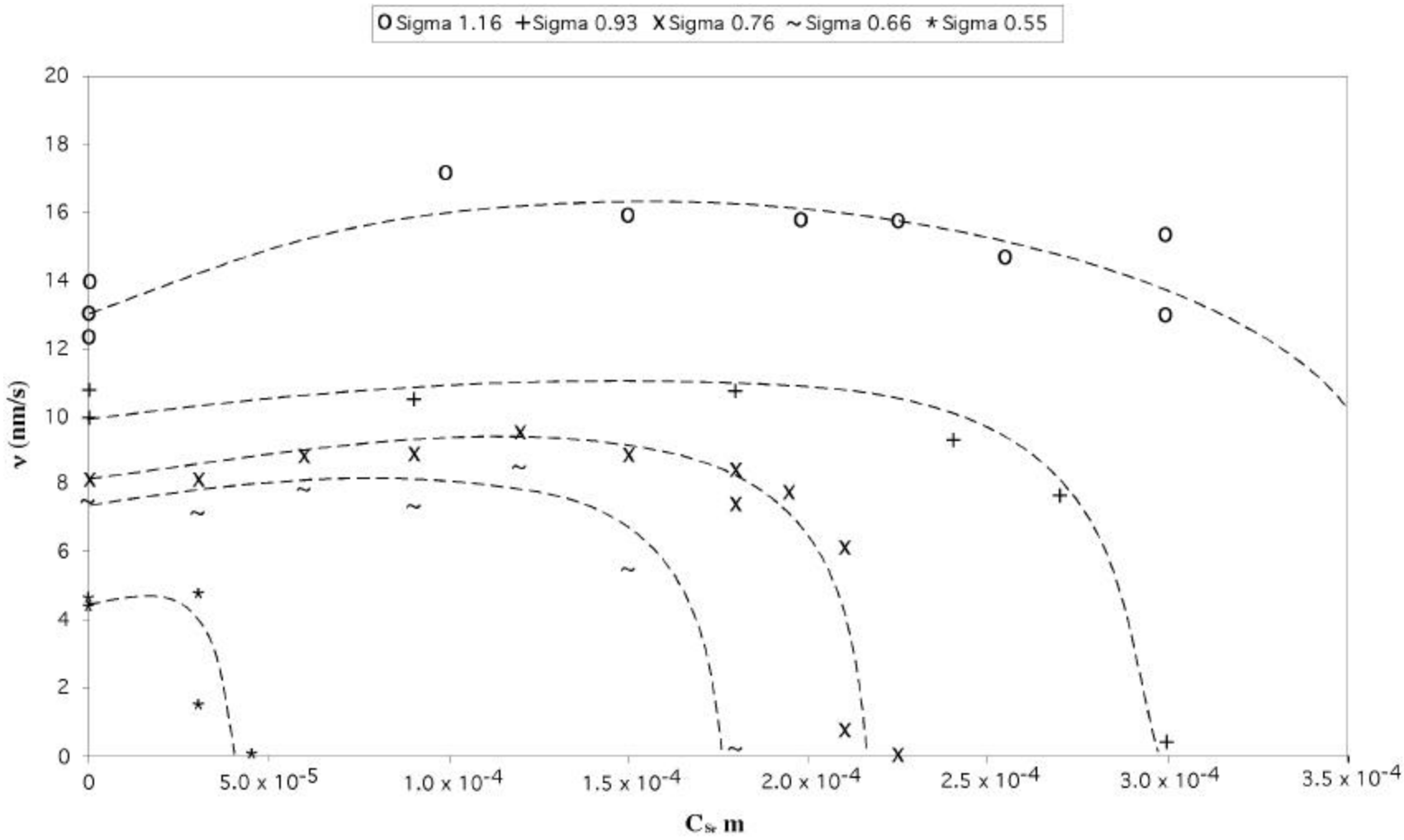

Figure 3-1 Step velocities as a function of strontium concentration at constant supersaturation for positive step directions. Dashed lines represent a visual fit of the data.

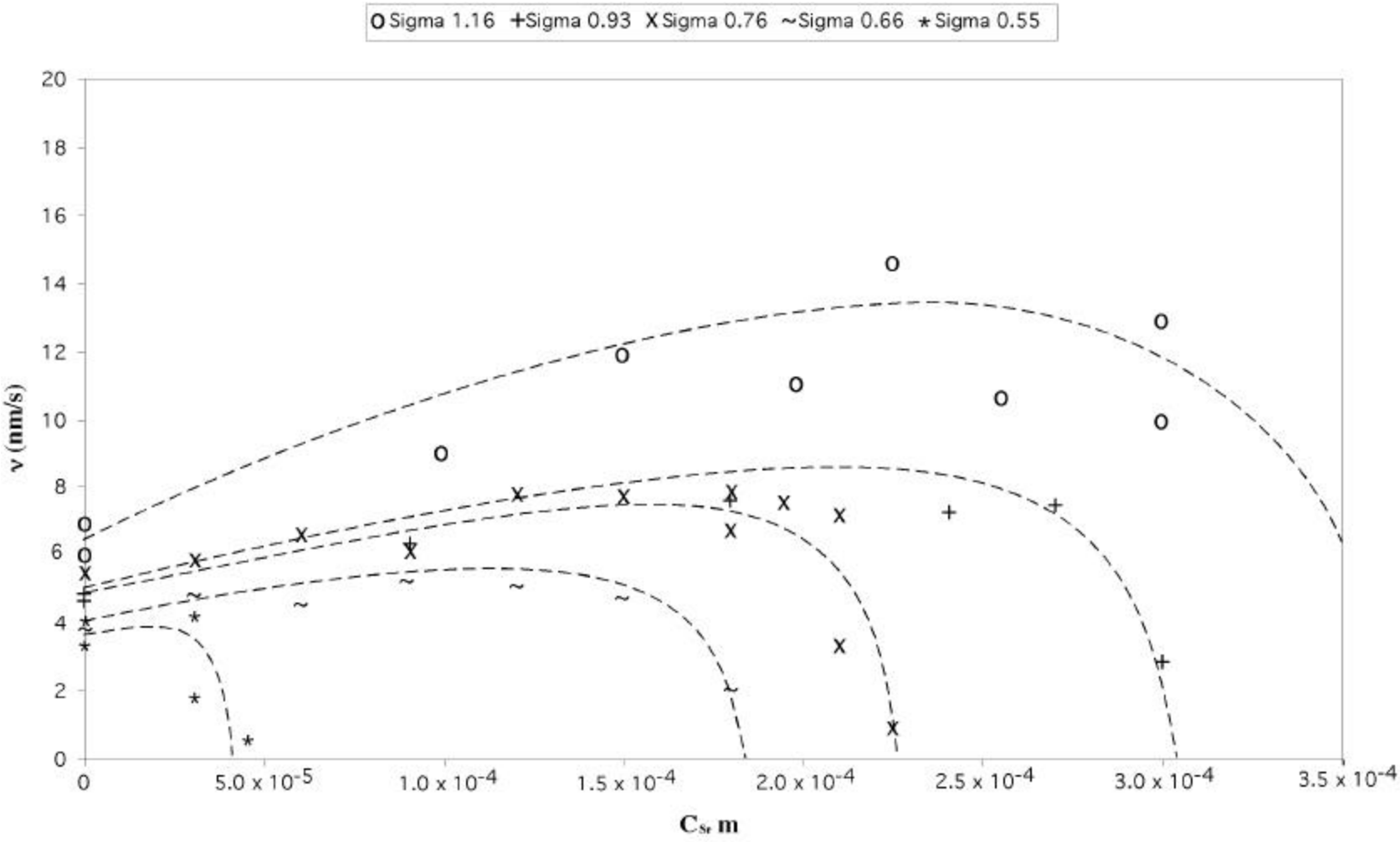

Figure 3-2 Step velocities as a function of strontium concentration at constant supersaturation for negative step directions. Dashed lines represent a visual fit of the data.

material with a lower solubility, thus increasing the chemical potential of the system. Rates may also be enhanced by an increase in the kinetics of growth unit attachment.

At higher Sr levels, there is a very strong rate *inhibiting* effect that may occur by short- or long-lived adsorption and pinning at step edges to kinetically impede step flow during layer growth. This blocking behavior could also be caused by an accumulation of strontium at step edges due to the limited solid solution of Sr into calcite.

3.2 Crystal Growth Impurity Models

The mechanisms by which small molecules affect mineral formation by inhibiting growth can be summarized within the framework of impurity models established by the crystal growth community. These models begin with the assumption that growth is occurring by the advancement of step edges as monomolecular units or small groups of steps. Assuming a constant supersaturation, ions or molecules can inhibit step flow by incorporation or step blocking or can enhance step flow through changes in kinetics or thermodynamics. Both of these mechanisms for growth inhibition exhibit a characteristic dependence of step migration velocity upon supersaturation and upon the impurity concentration of the growth solution (Dove and Davis, 2003).

The findings of this study, however, show that low levels of strontium increase growth rates. This behavior, to our knowledge, is unprecedented. Thus, an established theoretical model to fully explain our findings does not yet exist. In this thesis, we suggest the introduction of a new model to account for small molecule interactions that can increase the rate of crystal growth.

The following discussion summarizes the mechanisms by which small molecules can modify growth. First, two established rate-inhibiting models are described. We then introduce our preliminary construct for a rate enhancement model.

3.2.1 Step blocking

Step "pinning" or "blocking" occurs when impurity molecules adsorb to step-edges or accumulate on terraces ahead of migrating steps, thereby decreasing the velocity of those steps. Theoretical step velocities as a function of impurity concentration at different supersaturations are presented in Figure 3-3a. In the case of step blocking, step velocity is unaffected by the impurities in solution until a threshold impurity concentration is met that causes a sudden decrease in growth rate. The threshold impurity concentration required for retardation of growth is characteristic of the supersaturation of the solution, where higher supersaturations (where $\sigma_3>\sigma_2>\sigma_1$) require a greater impurity concentration for a cessation of growth to occur (Dove and Davis, 2003).

The effect of impurities on kinetic behavior is normally expressed in the crystal growth literature as v_s versus σ. Figure 3-3b shows the relationship between the various supersaturation regimes and step velocity. At some system-dependent threshold supersaturation, σ^*, the steps break through the chain of adsorbed impurities to result in a sharp rise in v_s. This theory explains the nonlinear dependence of v_s on σ that is often observed at lower supersaturations in the presence of impurities. At still lower supersaturations, no growth is observable and the regime is termed the "dead zone" of supersaturation. Above σ^* the linear relationship between v_s and σ, characteristic of the pure system, is reassumed. The width of the "dead zone" of supersaturation increases with increasing impurity concentration. The greater the concentration of impurities in solution (C_i), the higher the threshold supersaturation (σ^*) that is needed for steps to break through the impurity fence (where $C_3>C_2>C_1$). Accordingly, higher impurity concentrations result in a wider "dead zone" of supersaturation (Dove and Davis, 2003).

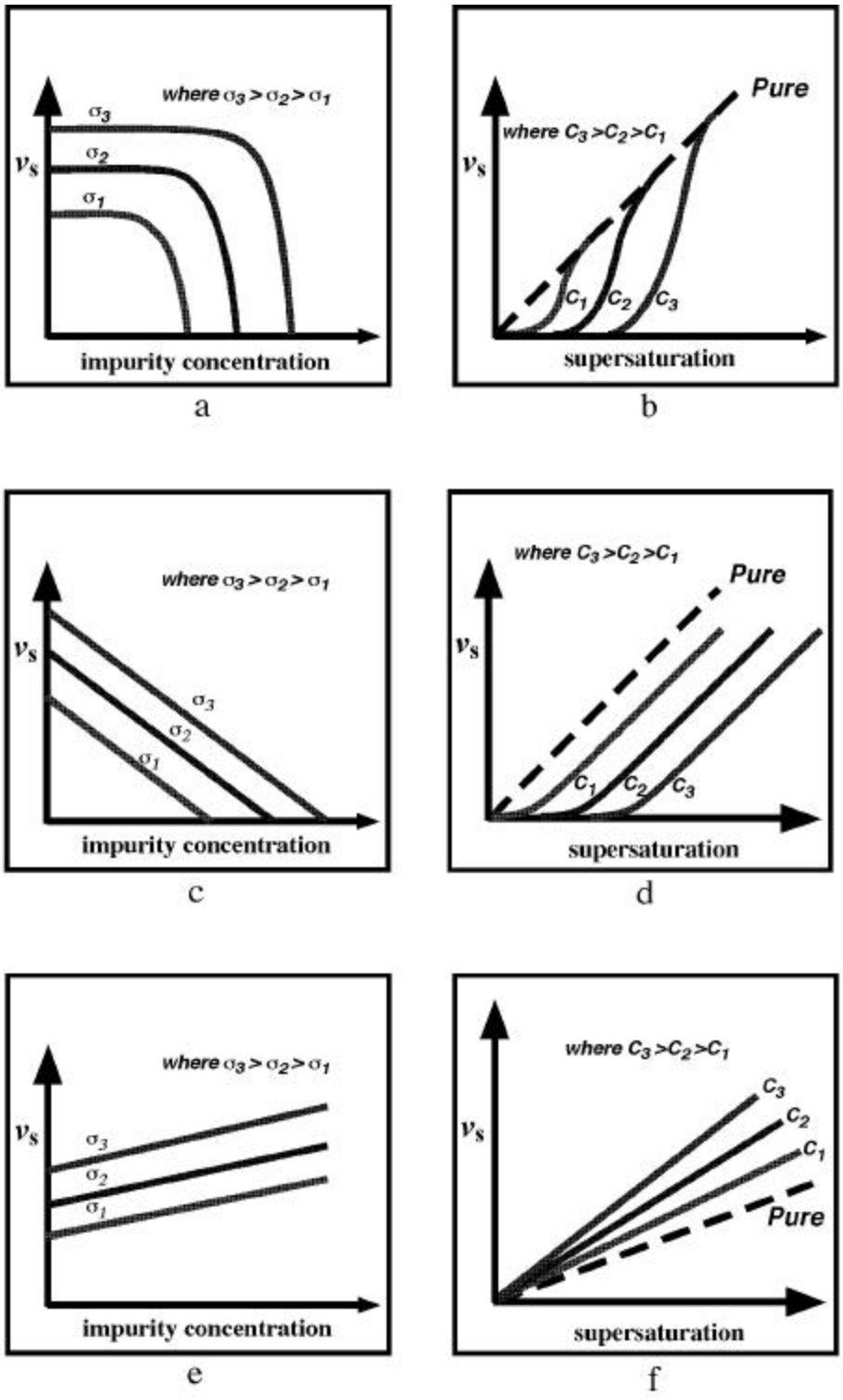

Figure 3-3 Crystal growth impurity models for step blocking (a and b) incorporation (c and d) and rate enhancement (e and f).

3.2.2 Incorporation

Impurity incorporation occurs when foreign ions or molecules become captured by advancing steps or otherwise incorporate at kink sites along a step edge to become part of the growing crystal. The dependence of step velocity on impurity concentration during incorporation is shown in Figure 3-3c. The theoretical model predicts that step velocity decreases linearly with increasing impurity concentration. Higher supersaturations (where $\sigma_3>\sigma_2>\sigma_1$) result in a faster growth rate at the same impurity concentration (Dove and Davis, 2003).

Typically, the impurity molecules distort the crystal structure, thereby increasing the internal surface free energy of the solid through an enthalpic contribution (Voronkov and Rashkovich, 1992; van Enckevort and van der Berg, 1998). The resulting increase in free energy is manifested as an increase in the solubility (K_{sp}) of the crystal, leading to a lower effective supersaturation. Since σ is defined as the natural logarithm of the ion activity product divided by the solubility constant, an increase in the solubility of the crystal reduces the effective supersaturation. As seen in Figure 3-3d, this result shifts step velocity curves to higher equilibrium activities, resulting in an apparent "dead zone" of supersaturation. Above σ^*, the linear relationship between step velocity and σ characteristic of the pure system is regained. However, the absolute magnitude of the step velocity always remains below that of the pure system at the same supersaturation (Dove and Davis, 2003).

It is useful to note that the kinetic behavior of the system, upon incorporation of impurities, does not significantly deviate from the linear dependence of v_s on σ. Instead,

the kinetic curves are simply shifted over to the higher supersaturations needed to achieve the same growth rate that is observed in the pure system (Figure 3-3d). The greater the impurity concentration in solution, the wider the dead zone and the farther the curve is shifted away from that of the pure system. In this situation, growth rates at supersaturations above σ^* under conditions of impurity incorporation yield lower growth rates than does the pure system for the same σ (Dove and Davis, 2003).

It is not always the case that incorporation results in decreasing growth rates. In systems where incorporation results in a large entropic contribution to the free energy of the system, growth rates can exceed that of the pure system.

3.2.3 Rate Enhancement

A theoretical model for the enhancement of growth rates has not been previously discussed. To our knowledge, there are no experimental examples of this behavior. Our investigation of strontium controls on calcite growth suggests, however, that such an effect must exist. Using a simple construct, we propose a theoretical model whereby step velocities increase linearly with increasing impurity concentration as shown in Figure 3-3e. Higher supersaturations (where $\sigma_3>\sigma_2>\sigma_1$) result in a faster growth rate at the same impurity concentration.

Figure 3-3f shows the corresponding relationship between step flow velocity and supersaturation for those impurity levels. The higher the concentration of impurities in solution (C_i), the faster the steps advance at a rate greater than the pure system (where $C_3>C_2>C_1$).

At this time, the rate enhancement model cannot distinguish between thermodynamic or kinetic effects. There are two possible explanations for this accelerated growth. First, changes in surface thermodynamics may occur when growth results in the formation of a solid solution with the impurity to yield a material with a lower solubility, thus increasing the chemical potential of the system. Rates may also be enhanced by an increase in the kinetics of growth unit attachment.

3.3 Step Velocity Measurements Revisited

The graphical representations of step velocities as a function of strontium concentration can be compared to the qualitative form expressed by the crystal growth impurity models. At low strontium concentrations, the data in Figures 3-1 and 3-2 agree best with the theoretical rate enhancement model shown in Figure 3-3e. At higher levels of strontium, step velocity measurements closely resemble the step-blocking mechanism in Figure 3-3a. This suggests that at a constant supersaturation, there is a shift from a rate-enhancing mechanism to a step-blocking rate-inhibiting mechanism with the addition of strontium into the system.

Step velocity measurements are also presented as v_s versus σ for further comparison to the theoretical impurity models. Figures 3-4 and 3-5 show graphical representations of measured step velocities as a function of supersaturation at constant strontium concentrations for the positive and negative step directions, respectively. The critical concentration required to initiate growth increases with increasing levels of strontium. When supersaturations exceed σ^*, growth rates further increase to levels that are greater than those measured for the pure calcite system.

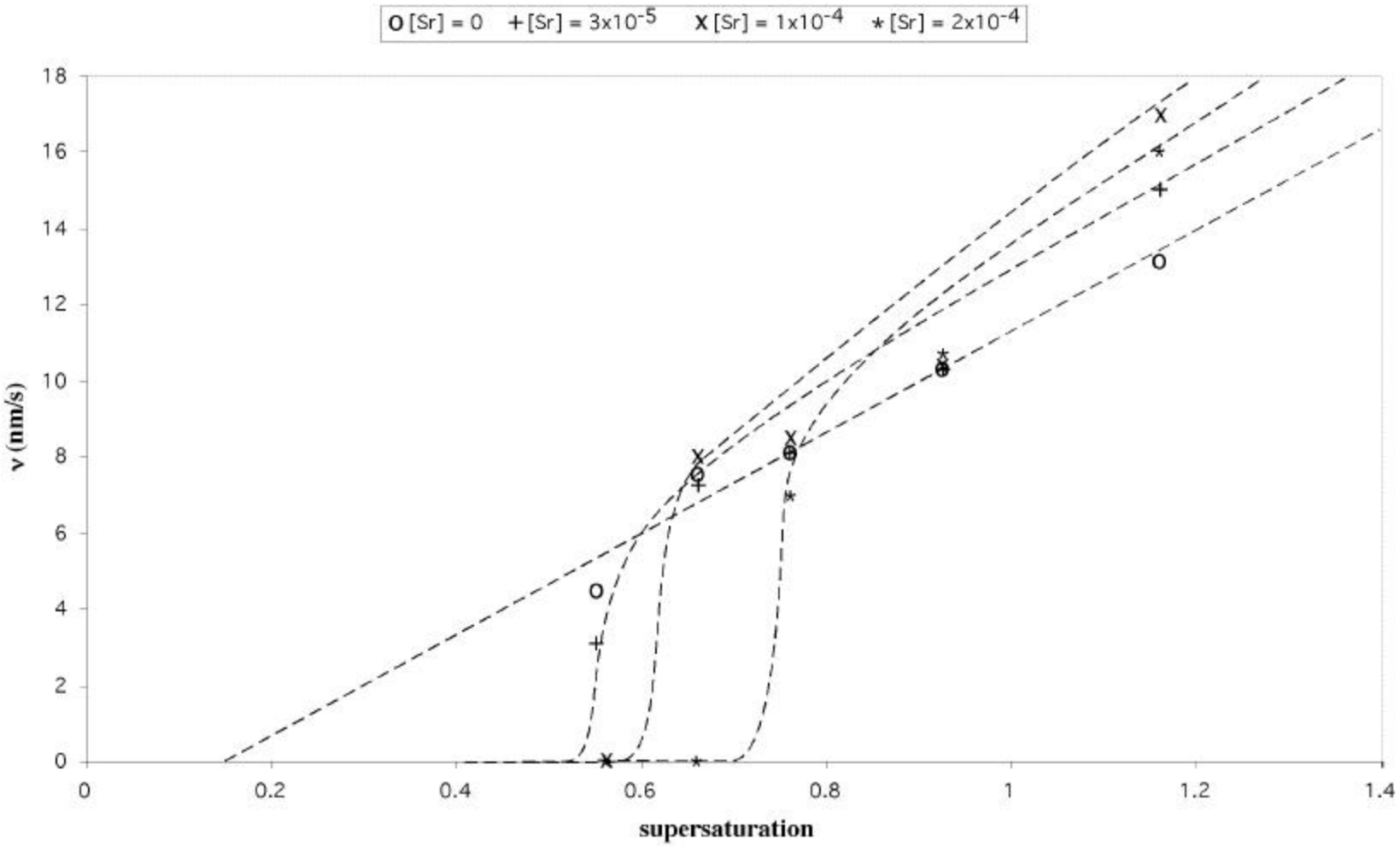

Figure 3-4 Step velocities as a function of supersaturation at a constant strontium concentration for positive step directions. Dashed lines represent a visual fit of the data.

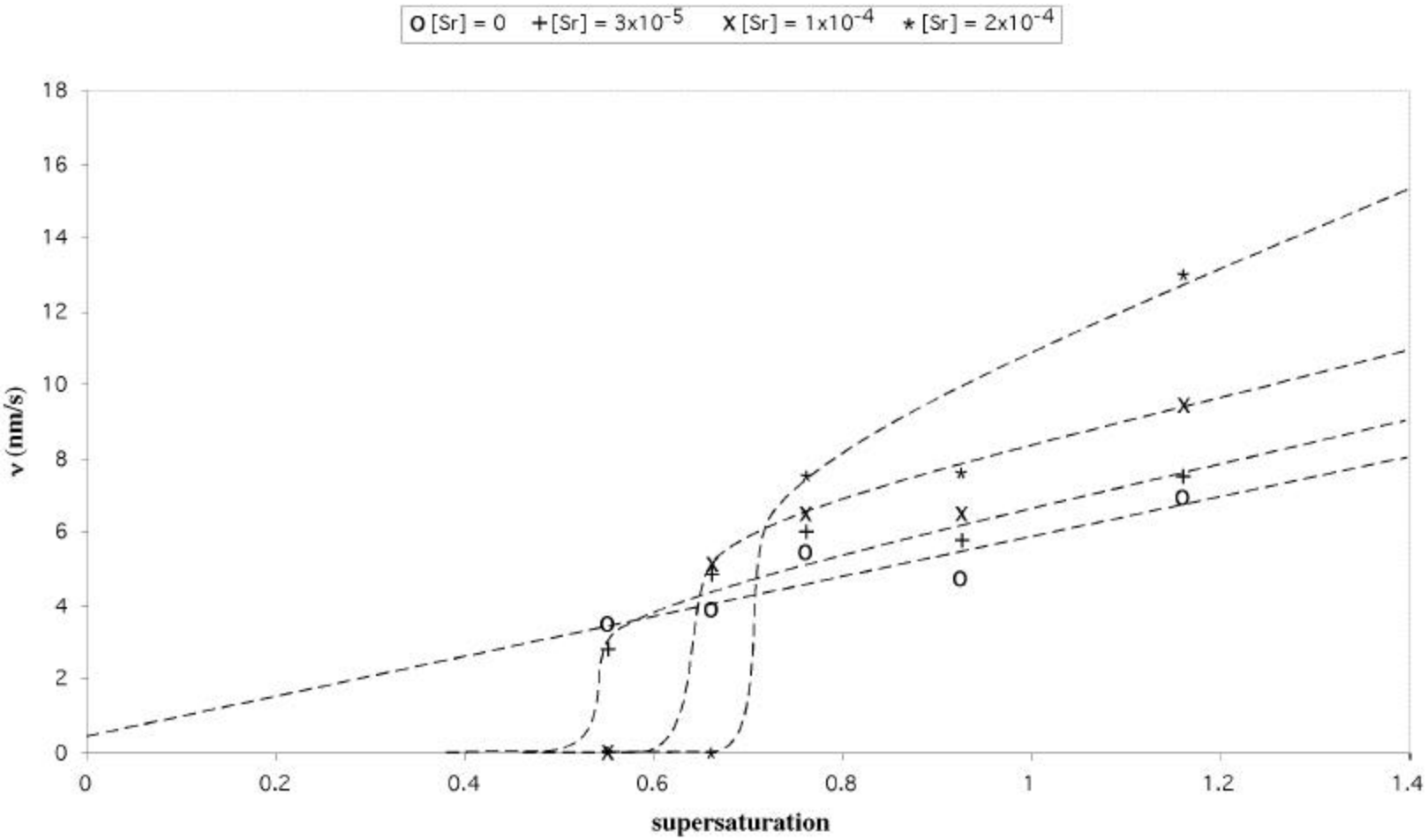

Figure 3-5 Step velocities as a function of supersaturation at a constant strontium concentration for negative step directions. Dashed lines represent a visual fit of the data.

3.4 Kinetic Coefficients

Kinetic coefficients (β) were calculated using step velocity measurements corresponding to those experiments conducted at the low levels of strontium that caused an increase in crystal growth rate. Figures 3-6 and 3-7 show step velocities as a function of $a - a_e$ for positive and negative step directions, respectively, which is proportional to supersaturation and given by the relation:

$$(a - a_e) = a_{Ca^{2+}} - \frac{K_{sp}}{a_{CO_3^{2-}}}$$

(Eqn. 3.1)

From the slopes of the lines in Figures 3-6 and 3-7, kinetic coefficients were calculated using the formula:

$$n_s = bw(a - a_e)$$

(Eqn. 3.2)

from classical crystal growth theory (Burton et al., 1951; Chernov, 1961) where ω is the specific molecular volume of calcite (6.3 X 10^{-23} cm^3/molecule). A summary of kinetic coefficients as a function of strontium concentration is presented in Table 3-2. Figure 3-8 shows kinetic coefficients increasing with the addition of strontium for positive and negative step directions. Increased kinetic coefficients suggest that rate enhancement is caused by changes in kinetics of growth. The relationships for β as a function of strontium concentration for the positive and negative step directions are given by:

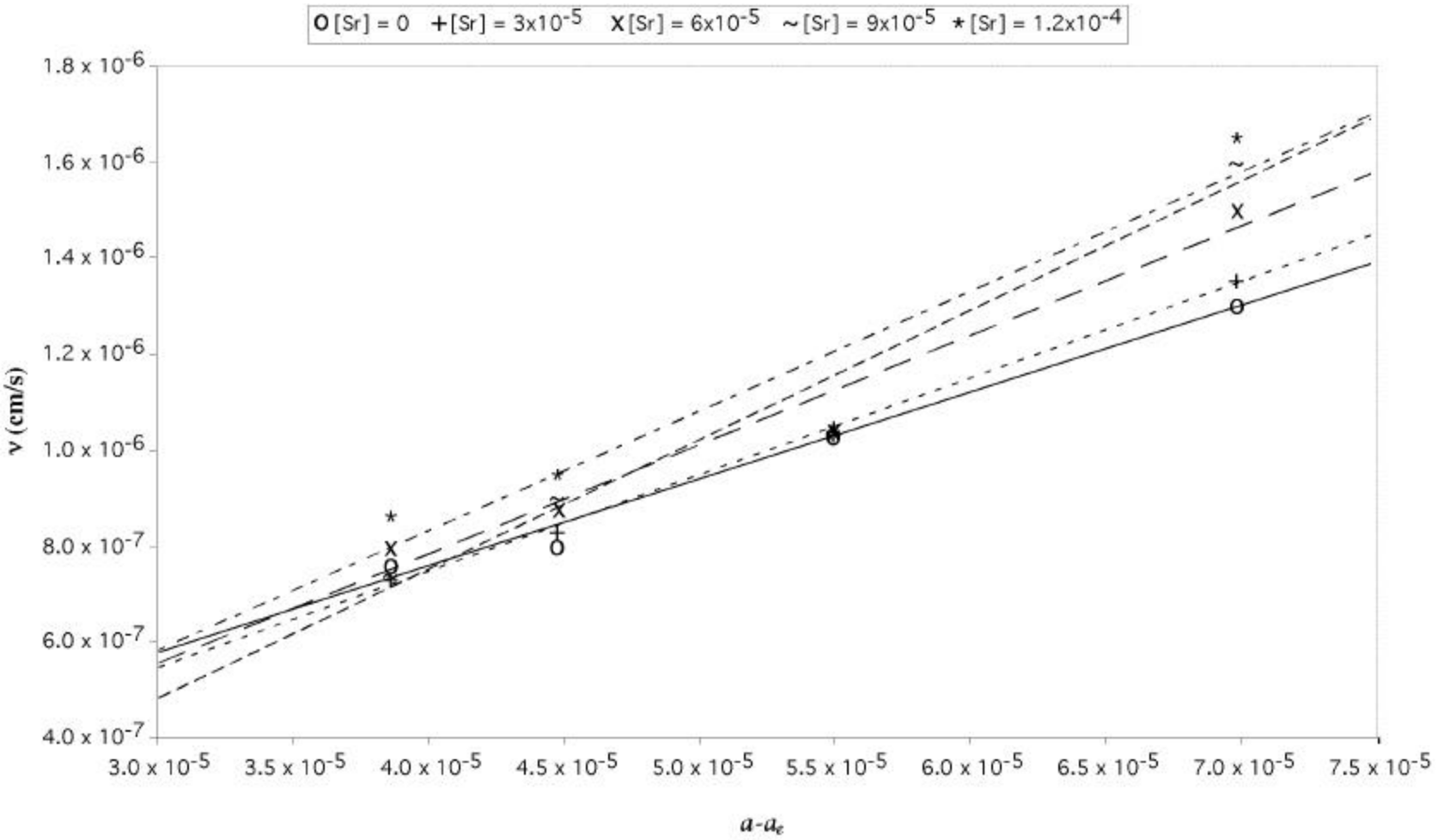

Figure 3-6 Slopes used to calculate β at different Sr concentrations for positive step directions.

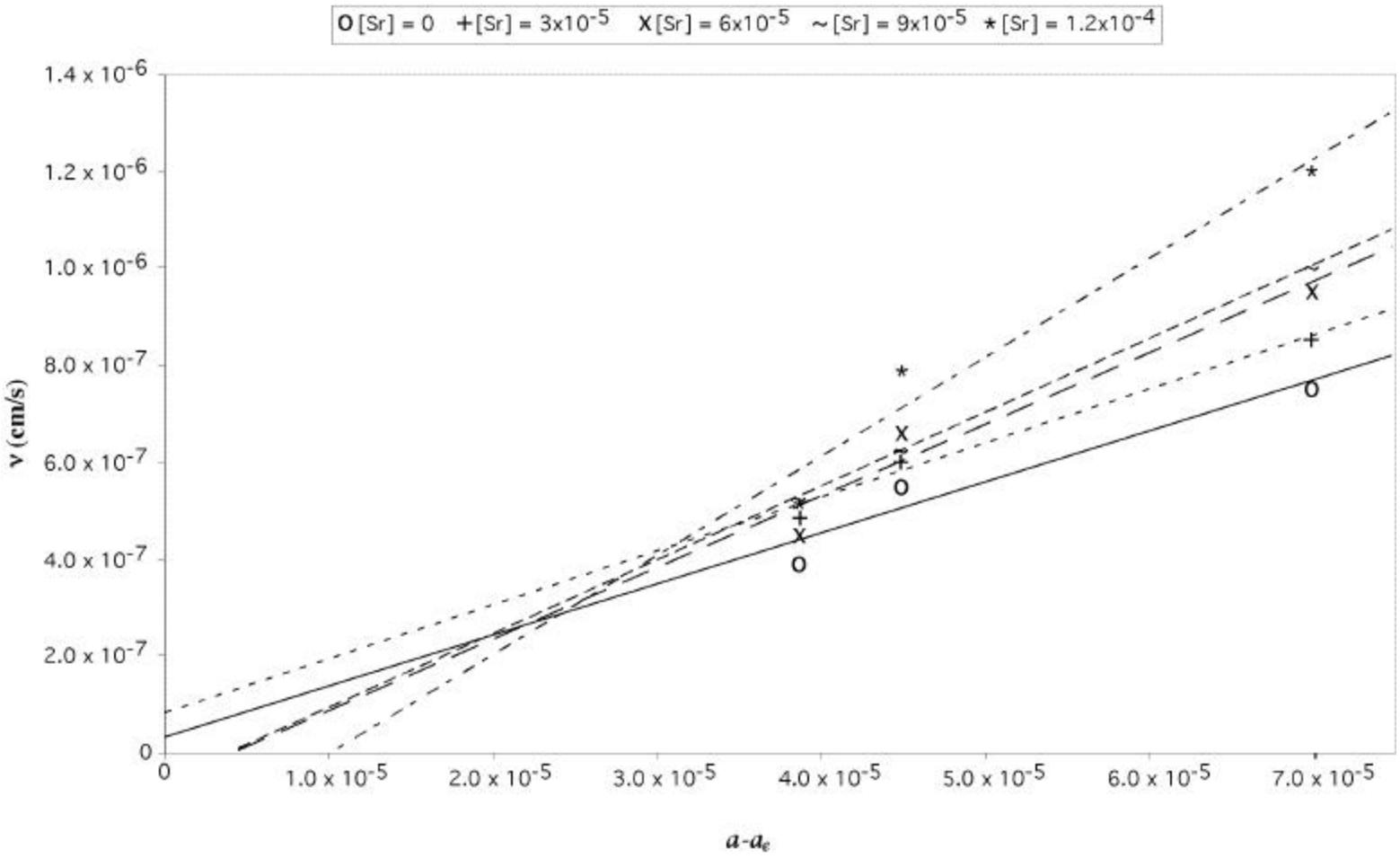

Figure 3-7 Slopes used to calculate β at different Sr concentrations for negative step directions.

Table 3-2 Summary of kinetic coefficients as a function of strontium concentration for + and - step directions.

Step Direction	C_{Sr} **(m)**	n /**a - a**$_e$	b **(cm/s)**
+	0	0.018	0.493
+	3.0×10^{-5}	0.020	0.547
+	6.0×10^{-5}	0.023	0.618
+	9.0×10^{-5}	0.027	0.732
+	1.2×10^{-4}	0.025	0.677
-	0	0.011	0.285
-	3×10^{-5}	0.011	0.304
-	6.0×10^{-5}	0.015	0.398
-	9.0×10^{-5}	0.017	0.461
-	1.2×10^{-4}	0.021	0.569

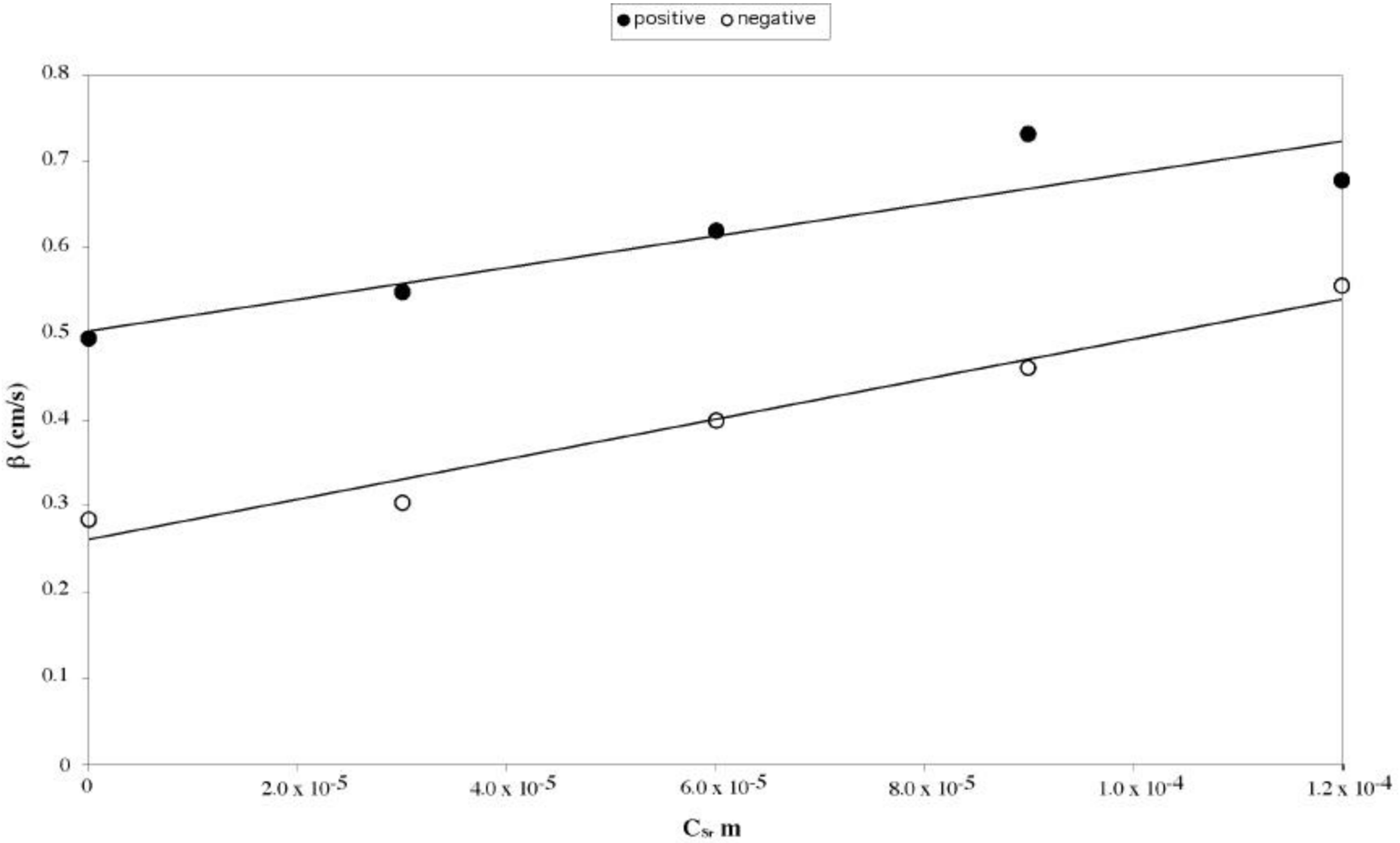

Figure 3-8 Kinetic coefficients as a function of strontium level for + and - step directions.

$$b_{+} = 1842.7C_{Sr} + 0.5029$$

(Eqn. 3.3a)

$$b_{-} = 2330.5C_{Sr} + 0.2607$$

(Eqn. 3.3b)

where C_{Sr} is the strontium concentration in moles/L of the system. The higher intercept value for β_{+} reflects the faster growth rate observed for the positive step edge directions. This is consistent with the previous results of Davis (2000).

3.5 Terrace Widths

The distances between the monomolecular step edges, known as terrace widths (λ), were measured on growth hillocks for the subset of data that showed increased step velocities with the addition of low concentrations of strontium. For a given hillock, larger terrace widths generally were observed for steps corresponding to the positive direction compared to the negative direction. A summary of terrace width data as a function of strontium concentration is presented in Table 3-3 for all supersaturations. Figures 3-9 and 3-10 show normalized terrace widths increasing with the addition of strontium for positive and negative step directions, respectively, at several different supersaturations. In general, the slopes of the lines decrease with increasing supersaturation. Since increasing λ correlates with a lower apparent supersaturation by the relation $\lambda \propto 1/\sigma$, rate enhancement is *not* caused by the formation of a material with a lower solubility. Therefore, it appears that the origin of the observed increased step velocities is primarily a kinetic effect that outweighs possible changes in the surface thermodynamics of growth.

Table 3-3 Summary of terrace width measurements as a function of strontium level for + and - step directions.

Hillock #	s	C_{Sr} **m**	l_+ **(nm)**	l_- **(nm)**
1	1.16	0	153	75
1	1.16	9.89×10^{-5}	172	92
1	1.16	1.98×10^{-4}	218	158
2	0.93	0	131	53
2	0.93	8.99×10^{-5}	166	100
2	0.93	1.80×10^{-4}	198	126
3	0.76	0	187	115
3	0.76	3.00×10^{-5}	197	146
3	0.76	6.00×10^{-5}	273	215
4	0.76	0	67	37
4	0.76	8.99×10^{-5}	136	99
4	0.76	1.20×10^{-4}	168	129
4	0.76	1.50×10^{-4}	230	193
5	0.66	0	97	66
5	0.66	3.00×10^{-5}	216	137
5	0.66	6.00×10^{-5}	224	156
5	0.66	8.99×10^{-5}	304	187
5	0.66	1.20×10^{-4}	302	201
6	0.55	0	151	112
6	0.55	3.00×10^{-5}	170	157

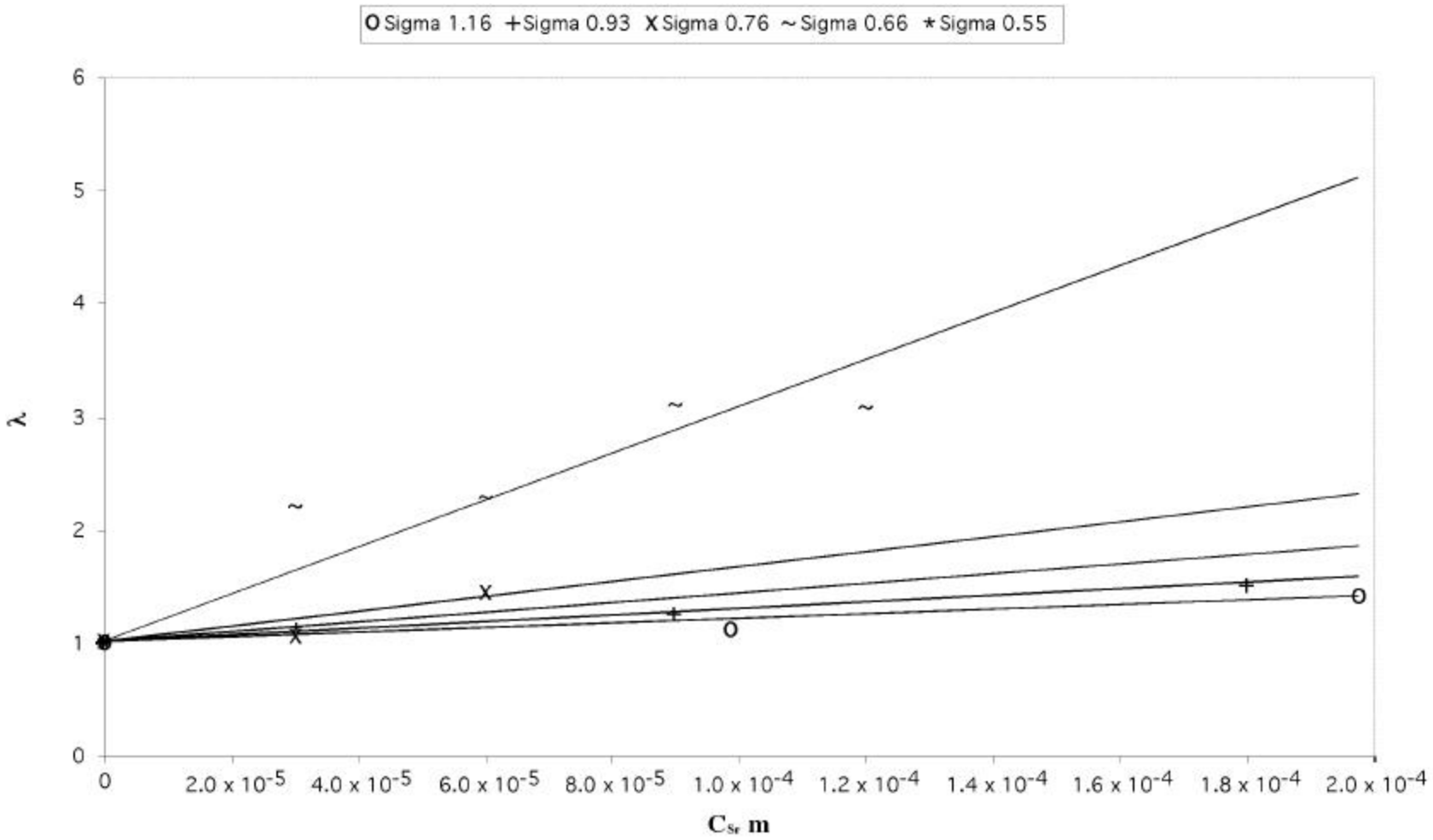

Figure 3-9 Normalized terrace widths as a function of strontium concentration for positive step directions.

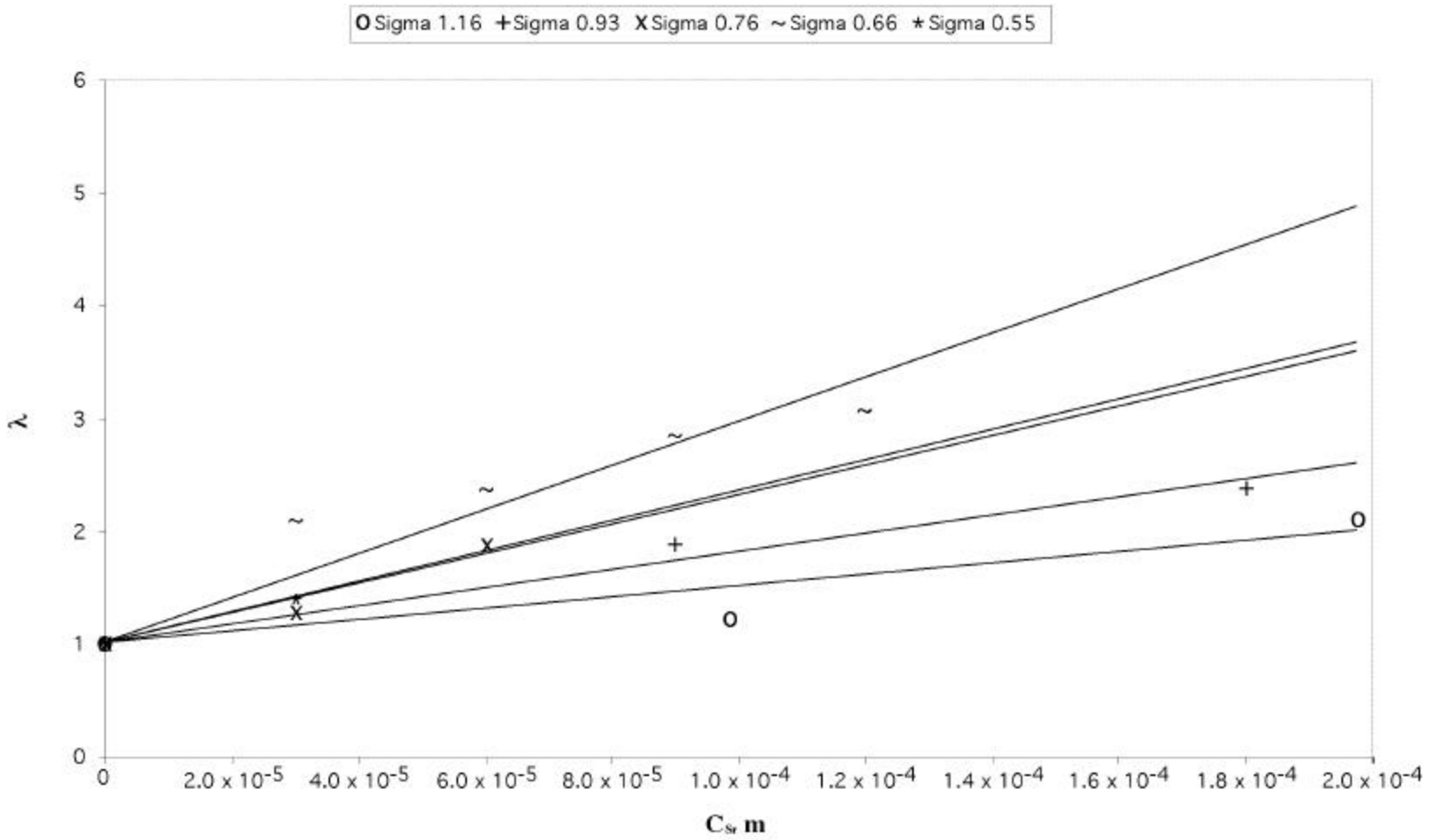

Figure 3-10 Normalized terrace widths as a function of strontium concentration for negative step directions.

3.6 Hillock Morphology

Calcite growth in the pure system generated spiral-sourced hillocks with straight step edges. Small additions of strontium led to significant changes in hillock morphology. As seen in Figure 3-11a, hillocks elongate perpendicular to the c-glide plane with the addition of strontium suggesting greater inhibition of the +/+ and -/- step direction boundaries. For a given hillock grown in a solution with concentrations of strontium that cause growth rate inhibition, the steps along negative directions are roughened whereas the steps along positive directions appear smoother. This step edge morphology, along with comparison to crystal growth impurity models, suggests that the rate-inhibition mechanism for the negative direction is the result of long-lived adsorption and pinning at step edges to impede step flow. The smoother step edge morphology seen along positive directions suggests either a short-lived adsorption and pinning mechanism at step edges to impede step flow or blocking caused by an accumulation of strontium at step edges due to limited solid solution.

In contrast, Davis (2000) noted that small additions of magnesium led to roughening of the step edges along the negative directions of the growth hillock. Increasing additions of magnesium led to further roughening of step edges along negative directions, in addition to roughening along positive directions. In contrast with strontium, the addition of magnesium causes hillocks to elongate parallel to the c-glide plane, as shown in Figure 3-11b (Davis, 2000). This is attributed to preferential incorporation of magnesium into negative step directions thus causing strain due to lattice mismatch along the +/- step direction boundaries.

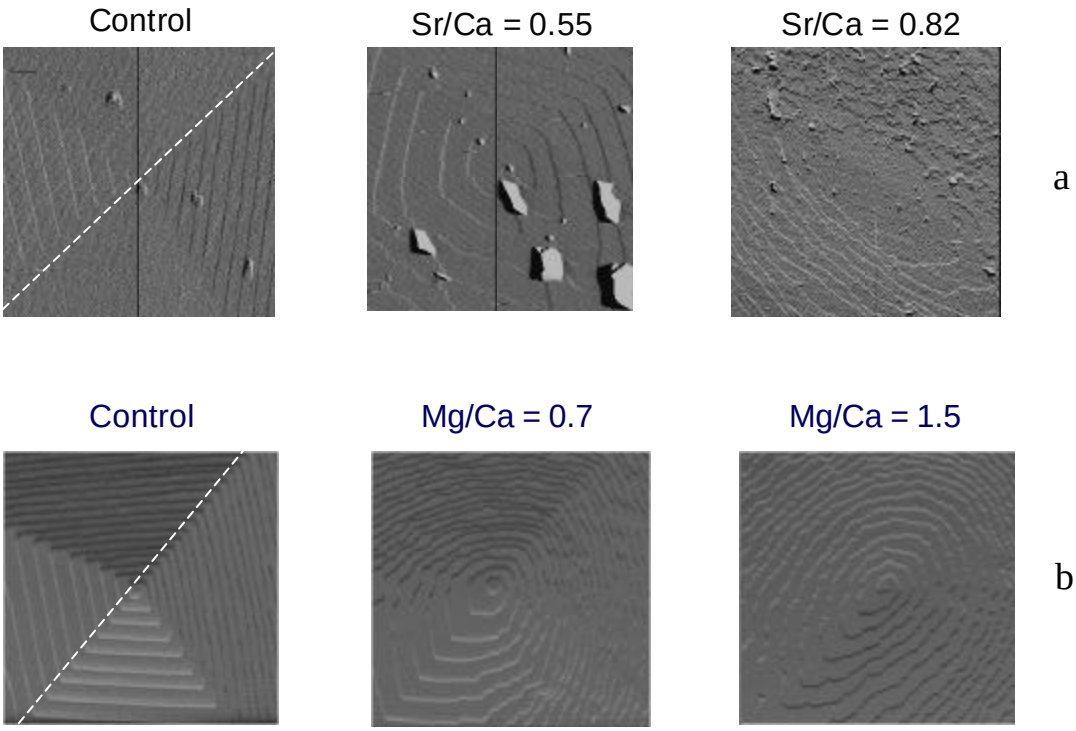

Figure 3-11 Contrast between the effect of Sr and Mg on hillock morphology demonstrated in a series of AFM images that increase in impurity activity form left to right. The addition of Sr (a) causes hillock elongation perpendicular to the c-glide plane, whereas, the addition of Mg (b) causes elongation parallel to the c-glide plane (from Davis et al. 2000).

3.7 Electron Probe Microanalysis (EPMA)

As described in section 2.5, calcite fragments were grown in $CaCO_3$-supersaturated solutions containing a known amount of strontium for 10 days. The resulting surfaces were examined for a sizable hillock to use for measurements of the strontium concentration in the calcite structure as a function of x and y directions. In this thesis, we show data for a hillock that was grown in a solution with a supersaturation of 0.66, a strontium concentration of $1x10^{-4}$ M and a temperature of approximately $23.3^{o}C$. This structure was centered under a grid consisting of 196 points spaced 4 microns apart for measurement of Sr levels using an electron microprobe. Results of this analysis are reported as two-dimensional coordinates with measured strontium concentrations in Table 3-4.

The EPMA data in Table 3-4 are represented graphically in Figure 3-12. The strontium map shows a general trend of higher Sr levels in the lower left corner of the plot and lower strontium concentrations in the upper right portion. The bottom left part of the graph corresponds with the two positive step directions while the top right corresponds to the negative directions. Therefore, Sr appears to be preferentially incorporated into the obtuse step directions. This observation agrees with the experimental findings of Paquette & Reeder (1994) and Reeder (1996). It should be noted that the levels of strontium incorporated into calcite hillocks under these experimental conditions were on the order of the detection limits of the microprobe. Long count times were used to improve the signal to noise ratio, but other analyses may give better results.

Table 3-4 Summary of microprobe results of strontium concentrations at each point of a grid centered over a calcite hillock grown in a solution at $\sigma = 0.66$ and $C_{Sr} = 1 \times 10^{-4}$ m.

x (mm)	y (mm)	C_{Sr} (ppm)	x (mm)	y (mm)	C_{Sr} (ppm)	x (mm)	y (mm)	C_{Sr} (ppm)	x (mm)	y (mm)	C_{Sr} (ppm)
0	58	1070	31	45	440	0	27	0	31	13	220
4	58	0	35	45	480	4	27	210	35	13	0
9	58	440	39	45	870	9	27	570	39	13	10
13	58	290	44	45	100	13	27	670	44	13	750
18	58	850	48	45	440	18	27	670	48	13	0
22	58	1070	53	45	150	22	27	230	53	13	0
26	58	920	57	45	650	26	27	1560	57	13	320
31	58	2230	0	40	210	31	27	410	0	9	970
35	58	720	4	40	350	35	27	860	4	9	1530
39	58	640	9	40	840	39	27	860	9	9	1130
44	58	2190	13	40	1030	44	27	0	13	9	540
48	58	2020	18	40	360	48	27	470	18	9	1380
53	58	1380	22	40	1770	53	27	0	22	9	2070
57	58	940	26	40	800	57	27	220	26	9	1500
0	54	1180	31	40	850	0	22	620	31	9	850
4	54	850	35	40	810	4	22	770	35	9	1620
9	54	270	39	40	480	9	22	960	39	9	760
13	54	540	44	40	0	13	22	1330	44	9	260
18	54	990	48	40	0	18	22	1650	48	9	0
22	54	1330	53	40	0	22	22	1260	53	9	290
26	54	570	57	40	430	26	22	1560	57	9	400
31	54	0	0	36	50	31	22	1090	0	4	1300
35	54	0	4	36	0	35	22	760	4	4	830
39	54	220	9	36	150	39	22	360	9	4	500
44	54	630	13	36	700	44	22	810	13	4	300
48	54	510	18	36	890	48	22	480	18	4	1340
53	54	510	22	36	1060	53	22	70	22	4	3180
57	54	950	26	36	800	57	22	550	26	4	2030
0	49	1140	31	36	770	0	18	1350	31	4	1750
4	49	1050	35	36	210	4	18	1460	35	4	810
9	49	1400	39	36	340	9	18	0	39	4	11880
13	49	1560	44	36	470	13	18	1670	44	4	900
18	49	70	48	36	0	18	18	2020	48	4	1090
22	49	540	53	36	0	22	18	1370	53	4	390
26	49	430	57	36	300	26	18	960	57	4	400
31	49	450	0	31	0	31	18	160	0	0	870
35	49	610	4	31	0	35	18	0	4	0	540
39	49	700	9	31	0	39	18	480	9	0	700
44	49	0	13	31	130	44	18	80	13	0	440
48	49	130	18	31	1830	48	18	690	18	0	700
53	49	750	22	31	480	53	18	20	22	0	1100
57	49	1180	26	31	860	57	18	180	26	0	2260
0	45	790	31	31	970	0	13	530	31	0	1580
4	45	640	35	31	0	4	13	780	35	0	1690
9	45	1360	39	31	0	9	13	60	39	0	420
13	45	1540	44	31	580	13	13	1800	44	0	1640
18	45	1000	48	31	820	18	13	2540	48	0	1460
22	45	190	53	31	350	22	13	2040	53	0	900
26	45	0	57	31	390	26	13	320	57	0	690

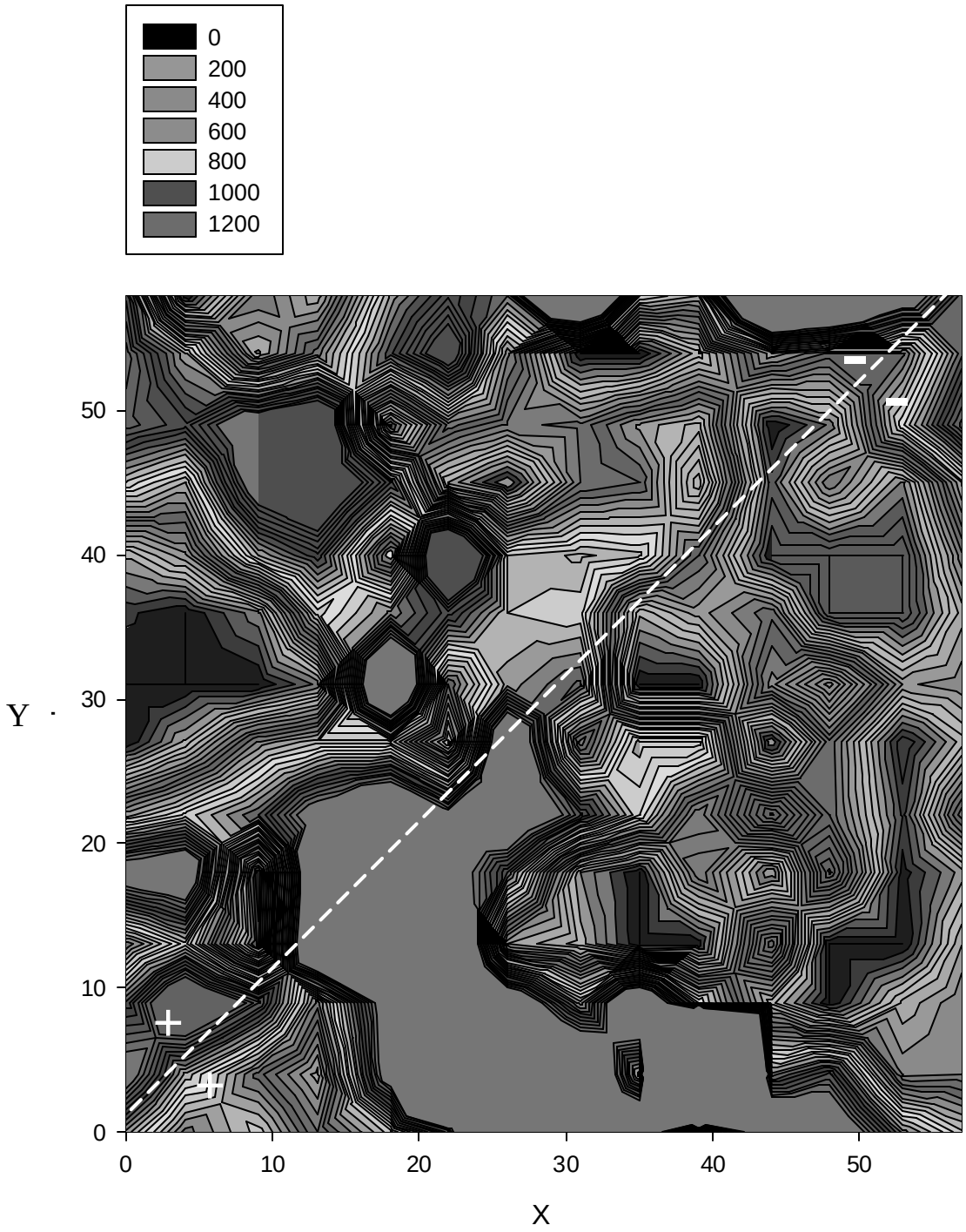

Figure 3-12 Graphical representation of microprobe results of strontium concentrations from Table 3-4.

3.8 Modeling

The experimental data collected in this study offer a unique opportunity to test the theoretical model of Cabrera and Vermilyea (1958). Their construct proposes that when impurities inhibit growth by a step-blocking mechanism, the relation can be quantified by expanding equation 3.2 to the expression:

$$n_s = bw(a - a_e)(1 - \frac{s^*}{s})$$

(Eqn. 3.4)

This theoretical model states that when an impurity ion interacts with the surface to block growth at high concentrations, the growth rate is inhibited by the critical supersaturation for growth, σ*. They showed that an expression for σ* is obtained by considering that the surface coverage of strontium ions (n, molecules/cm^2) is related to the concentration of strontium in solution (C_{Sr}, molecules/cm^3) by a partition coefficient (B, cm) according to:

$$n = BC_{Sr}$$

(Eqn. 3.5)

The average spacing of strontium ions on the surface ($n^{-1/2}$, cm/molecule) is given by:

$$n^{-1/2} = \frac{Awa}{kTs^*}$$

(Eqn. 3.6)

where A is a constant related to curvature (1.5), α is the step edge energy in ergs/cm^2, k is the Boltzmann constant (1.38 x 10^{-16} ergs/K) and T is temperature (298 K). Combining equations 3.5 and 3.6 and solving for σ^* obtains:

$$s^* = \frac{Awa B^{1/2} C_{Sr}^{1/2}}{kT}$$

(Eqn. 3.7)

This expression predicts that the critical supersaturation for growth to proceed is proportional to the square root of the impurity concentration. Substituting equation 3.7 into equation 3.4 obtains:

$$n_s = bw(a - a_e)\left(1 - \frac{Awa B^{1/2} C_{Sr}^{1/2}}{skT}\right)$$

(Eqn. 3.8)

This is the theoretical crystal growth model for the dependence of step flow rate upon supersaturation when an impurity ion is present to modify growth by the blocking mechanism (Cabrera and Vermilyea, 1958). Equation 3.8 is expected to show a pattern of step velocity versus impurity concentration shown previously in Figures 3-3a and 3-3b.

To test this predictive model using the data reported in this study for the positive step directions, equation 3.8 is first evaluated to determine the dependence of α on strontium concentration and to estimate a value of B. Rewriting equation 3.8 produces the expression:

$$aB^{1/2}C_{Sr}^{1/2} = \frac{skT\left(1-\frac{n_s}{bw(a-a_e)}\right)}{Aw}$$

(Eqn. 3.9)

Substituting σ, ν_s, β and $(a\text{-}a_e)$ for each experiment gives the values of $\alpha B^{1/2}C_{Sr}^{1/2}$ as a function of strontium concentration, summarized in Table 3-5. Assuming that α is a linear function of strontium concentration, the expression can be written as:

$$a = SC_{Sr} + I$$

(Eqn. 3.10)

where S is the slope and I is the intercept of this relation. Substituting equation 3.10 into equation 3.9 produces:

$$SB^{1/2}C_{Sr}^{3/2} + IB^{1/2}C_{Sr}^{1/2} = \frac{skT\left(1-\frac{n_s}{bw(a-a_e)}\right)}{Aw}$$

(Eqn. 3.11)

After setting the intercept of the left portion of equation 3.11 to zero, the coefficients $SB^{1/2}$ and $IB^{1/2}$ were estimated by the computer software package *JMP*. Six of the 41 data points were determined to be outliers and therefore were omitted from the fit. The results give $SB^{1/2} = 2.707 \times 10^{-18}$ and $IB^{1/2} = 0.135$. Assuming that the value of α = 1421 ergs/cm^2 (Teng et al., 1998) for the pure system ($C_{Sr} = 0$) gives I. This allows us to determine that $B = 9.06 \times 10^{-9}$ cm. Dividing the coefficient $SB^{1/2}$ by this value for B, results in $S = 2.83 \times 10^{-14}$. Substituting the values for S and I into equation 3.10 gives:

Table 3-5 Summary of $\alpha B^{1/2} C_{Sr}^{1/2}$ as a function of strontium concentration for positive step directions.

s	C_{Sr} (m)	b (cm/s)	n (cm/s)	$\alpha B^{1/2} C_{Sr}^{1/2}$
0.55	0	0.503	4.41×10^{-7}	6.46×10^{7}
0.55	0	0.503	4.59×10^{-7}	5.71×10^{7}
0.55	3.00×10^{-5}	0.558	1.51×10^{-7}	1.91×10^{8}
0.55	3.00×10^{-5}	0.558	4.75×10^{-7}	7.00×10^{7}
0.55	4.50×10^{-5}	0.586	6.00×10^{-9}	2.46×10^{8}
0.66	0	0.503	7.57×10^{-7}	-1.65×10^{7}
0.66	3.00×10^{-5}	0.558	7.28×10^{-7}	2.52×10^{7}
0.66	6.00×10^{-5}	0.613	7.93×10^{-7}	2.76×10^{7}
0.66	8.99×10^{-5}	0.669	7.38×10^{-7}	6.67×10^{7}
0.66	1.20×10^{-4}	0.724	8.62×10^{-7}	4.88×10^{7}
0.66	1.50×10^{-4}	0.779	5.60×10^{-7}	1.47×10^{8}
0.66	1.80×10^{-4}	0.835	3.10×10^{-8}	2.88×10^{8}
0.76	0	0.503	8.17×10^{-7}	6.05×10^{6}
0.76	3.00×10^{-5}	0.558	8.13×10^{-7}	4.06×10^{7}
0.76	6.00×10^{-5}	0.613	8.82×10^{-7}	4.45×10^{7}
0.76	8.99×10^{-5}	0.669	8.92×10^{-7}	6.58×10^{7}
0.76	1.20×10^{-4}	0.724	9.51×10^{-7}	7.01×10^{7}
0.76	1.50×10^{-4}	0.779	8.85×10^{-7}	1.07×10^{8}
0.76	1.80×10^{-4}	0.835	7.42×10^{-7}	1.57×10^{8}
0.76	1.80×10^{-4}	0.835	8.43×10^{-7}	1.33×10^{8}
0.76	1.95×10^{-4}	0.862	7.78×10^{-7}	1.55×10^{8}
0.76	2.10×10^{-4}	0.890	6.16×10^{-7}	1.98×10^{8}
0.76	2.10×10^{-4}	0.890	7.80×10^{-8}	3.22×10^{8}
0.76	2.25×10^{-4}	0.918	9.00×10^{-9}	3.38×10^{8}
0.93	0	0.503	1.08×10^{-6}	-2.30×10^{7}
0.93	0	0.503	9.89×10^{-7}	1.23×10^{7}
0.93	8.99×10^{-5}	0.669	1.04×10^{-6}	9.50×10^{7}
0.93	1.80×10^{-4}	0.835	1.07×10^{-6}	1.51×10^{8}
0.93	2.40×10^{-4}	0.945	9.31×10^{-7}	2.13×10^{8}
0.93	2.70×10^{-4}	1.000	7.66×10^{-7}	2.58×10^{8}
0.93	3.00×10^{-4}	1.056	4.50×10^{-8}	4.05×10^{8}
1.16	0	0.503	1.21×10^{-6}	2.56×10^{7}
1.16	0	0.503	1.30×10^{-6}	-1.64×10^{5}
1.16	0	0.503	1.40×10^{-6}	-3.79×10^{7}
1.16	9.89×10^{-5}	0.685	1.72×10^{-6}	1.56×10^{7}
1.16	1.50×10^{-4}	0.779	1.59×10^{-6}	1.09×10^{8}
1.16	1.98×10^{-4}	0.868	1.58×10^{-6}	1.53×10^{8}
1.16	2.25×10^{-4}	0.918	1.57×10^{-6}	1.75×10^{8}
1.16	2.55×10^{-4}	0.973	1.47×10^{-6}	2.17×10^{8}
1.16	3.00×10^{-4}	1.056	1.31×10^{-6}	2.70×10^{8}
1.16	3.00×10^{-4}	1.056	1.53×10^{-6}	2.27×10^{8}

$$a = 2.83 \times 10^{-14} C_{Sr} + 1421$$

(Eqn. 3.12)

Substituting equation 3.12 into 3.8, results in a quantitative prediction of step velocity as a function of strontium concentration. With all variables now determined, the Cabrera-Vermilyea model is used to predict step velocities at constant supersaturations as a function of strontium concentration as seen in Table 3-6 and Figure 3-13.

An examination of Figure 3-13 shows that the theoretical model gives a poor prediction of the experimental behavior for most conditions of the data set. The model particularly breaks down at high strontium levels where the blocking effect is pronounced. Uncertainties in the estimate of $B^{1/2}$ and I, cannot explain the discrepancy.

One important shortcoming of the theoretical model may be that it assumes that the dependence of σ^* upon strontium concentration is independent of supersaturation. This is clearly not the case for the strontium-calcite system. Figures 3-14 and 3-15 show that supersaturation affects the σ^* versus strontium concentration relationship for positive and negative step directions, respectively. These data were calculated by separately fitting the measured step velocities at constant supersaturation to equation 3.4 as opposed to the previous model that fit all supersaturations simultaneously.

The aforementioned shortcoming of the model leads us to fit each supersaturation separately. This gives a much better correlation between the measured and calculated data as seen in Figures 3-16 and 3-17. The predicted step velocities as a function of strontium concentration better reproduce the experimental behavior for the positive and negative step directions, respectively.

Table 3-6 Summary of modeled step velocities as a function of strontium concentration for positive step directions.

C_{Sr}	n **(nm/s)**	n **(nm/s)**	n **(nm/s)**	n **(nm/s)**	n **(nm/s)**
m	s = 1.16	s = 0.93	s = 0.76	s = 0.66	s = 0.55
0	13.03	10.19	8.32	7.17	5.97
1.0×10^{-5}	13.09	10.17	8.23	7.04	5.79
2.0×10^{-5}	13.32	10.29	8.28	7.06	5.77
3.0×10^{-5}	13.54	10.41	8.34	7.07	5.74
4.0×10^{-5}	13.74	10.52	8.38	7.07	5.70
5.0×10^{-5}	13.92	10.60	8.39	7.05	5.63
6.0×10^{-5}	14.08	10.66	8.39	7.00	5.54
7.0×10^{-5}	14.21	10.70	8.36	6.93	5.43
8.0×10^{-5}	14.32	10.71	8.31	6.84	5.30
9.0×10^{-5}	14.40	10.70	8.22	6.72	5.14
1.0×10^{-4}	14.45	10.65	8.12	6.57	4.95
1.1×10^{-4}	14.47	10.58	7.98	6.40	4.73
1.2×10^{-4}	14.47	10.48	7.82	6.19	4.49
1.3×10^{-4}	14.43	10.35	7.62	5.96	4.21
1.4×10^{-4}	14.36	10.19	7.40	5.70	3.91
1.5×10^{-4}	14.26	10.01	7.15	5.41	3.58
1.6×10^{-4}	14.13	9.79	6.86	5.08	3.22
1.7×10^{-4}	13.97	9.53	6.55	4.73	2.83
1.8×10^{-4}	13.78	9.25	6.20	4.35	2.40
1.9×10^{-4}	13.55	8.93	5.82	3.93	1.95
2.0×10^{-4}	13.29	8.58	5.41	3.48	1.46
2.1×10^{-4}	12.99	8.20	4.96	3.00	0.94
2.2×10^{-4}	12.66	7.78	4.48	2.48	0.38
2.3×10^{-4}	12.30	7.33	3.97	1.93	0.00
2.4×10^{-4}	11.89	6.85	3.42	1.35	0.00
2.5×10^{-4}	11.46	6.33	2.84	0.73	0.00
2.6×10^{-4}	10.98	5.77	2.22	0.08	0.00
2.7×10^{-4}	10.47	5.18	1.57	0.00	0.00
2.8×10^{-4}	9.92	4.55	0.88	0.00	0.00
2.9×10^{-4}	9.34	3.88	0.15	0.00	0.00
3.0×10^{-4}	8.71	3.17	0.00	0.00	0.00

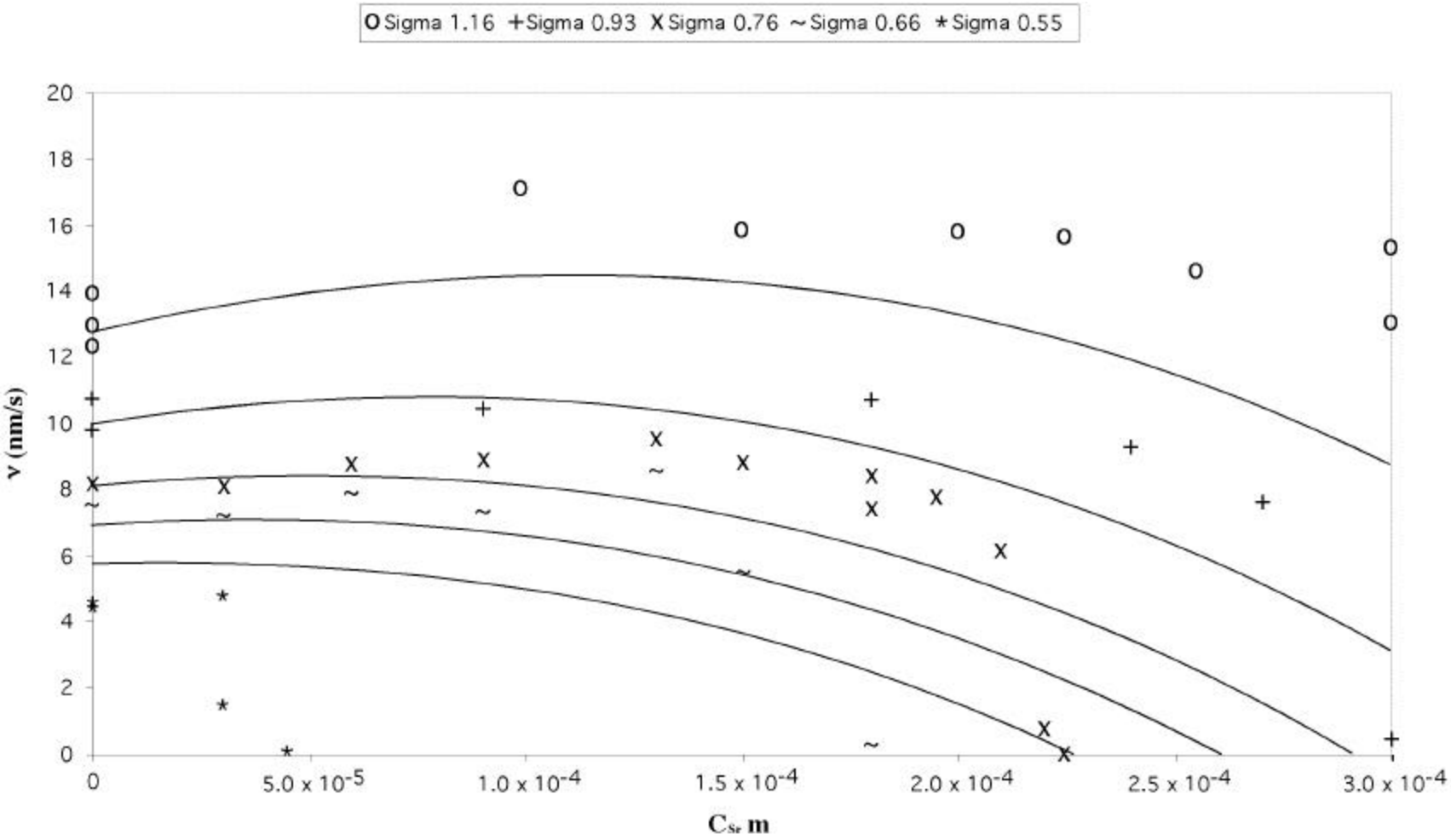

Figure 3-13 Modeled calculations of step velocities as a function of strontium concentration along with measured velocities for positive step directions (lines are calculated values).

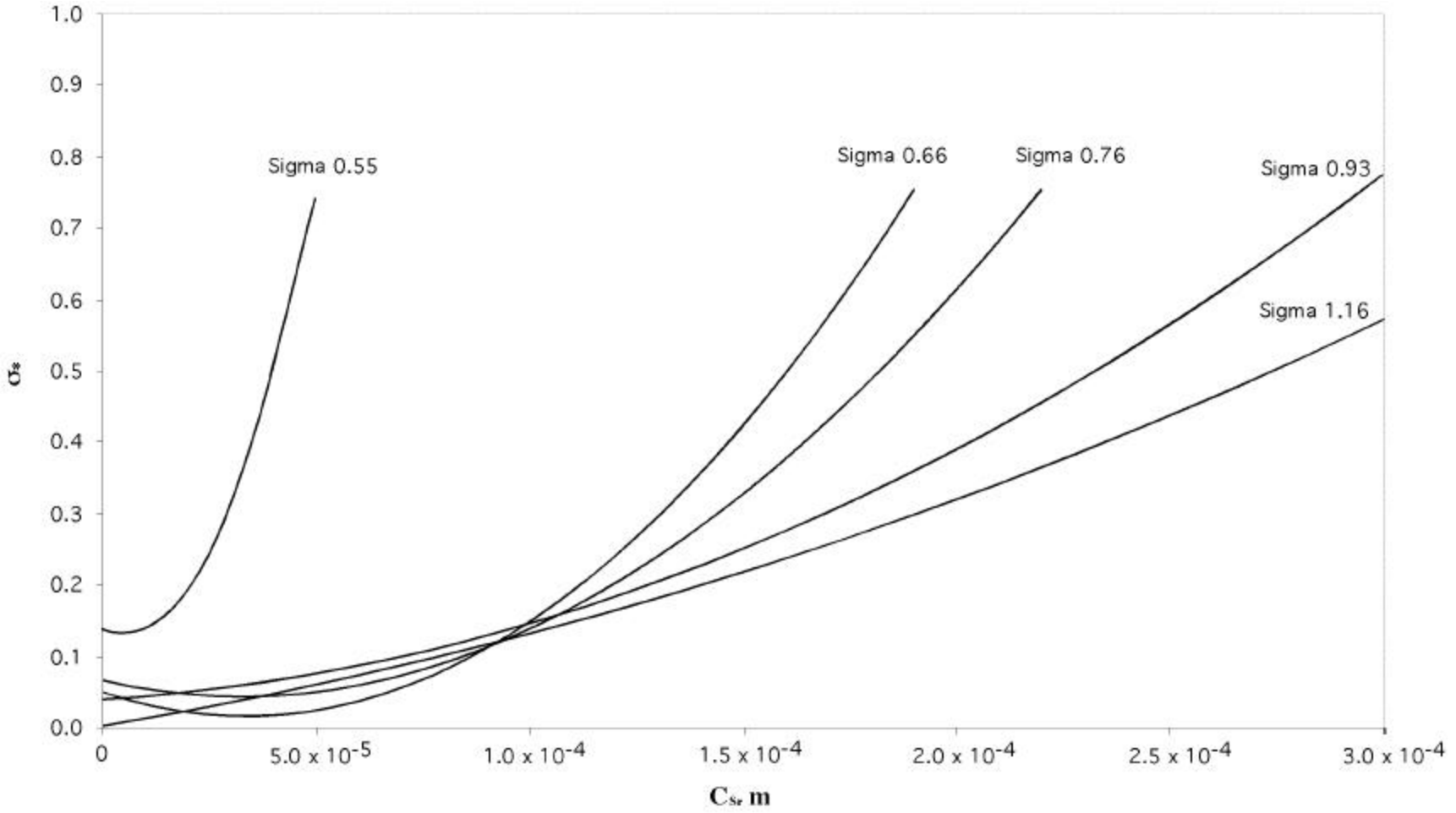

Figure 3-14 Calculated values for σ^* as a function of C_{Sr} for positive step directions.

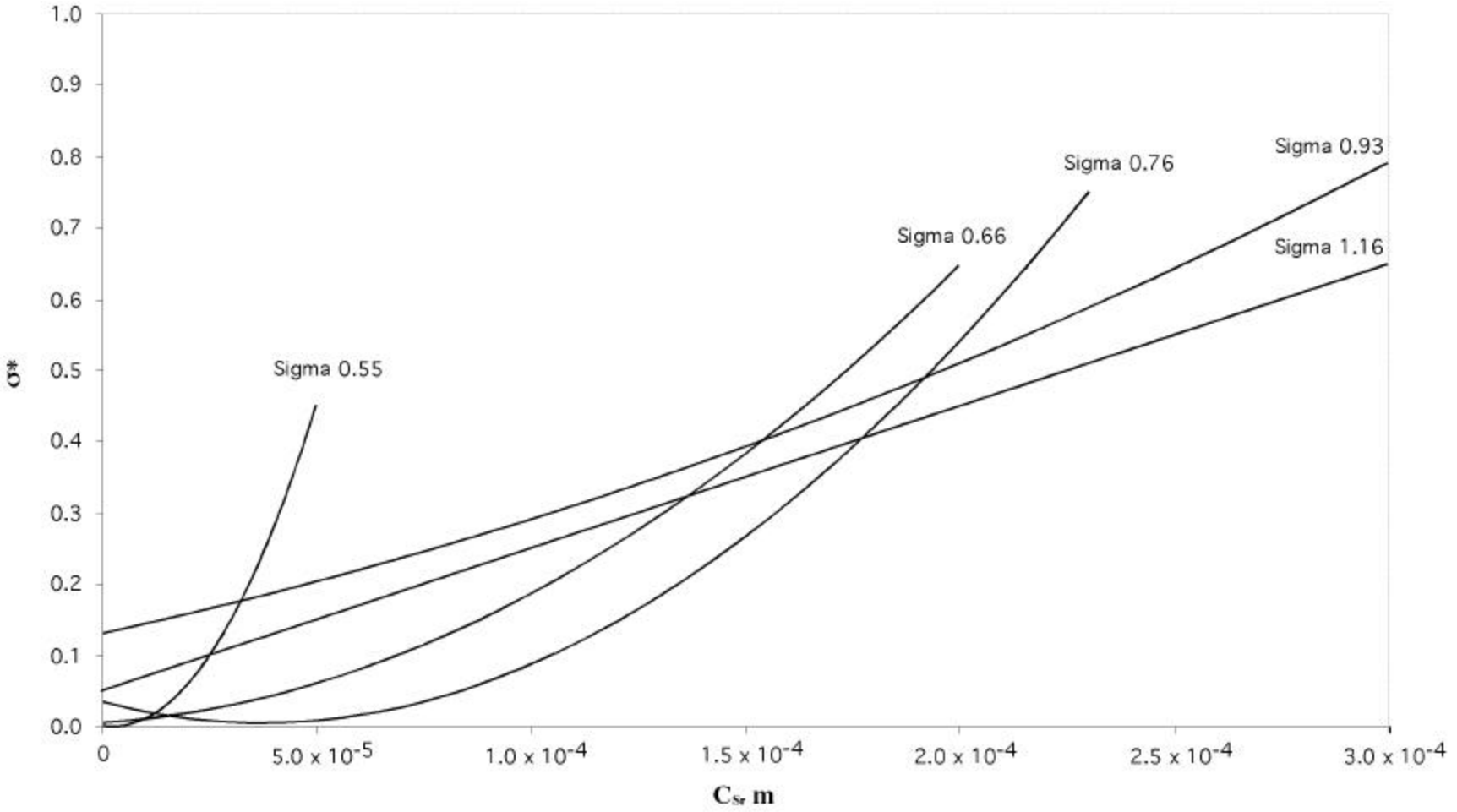

Figure 3-15 Calculated values for σ^* as a function of C_{Sr} for negative step directions.

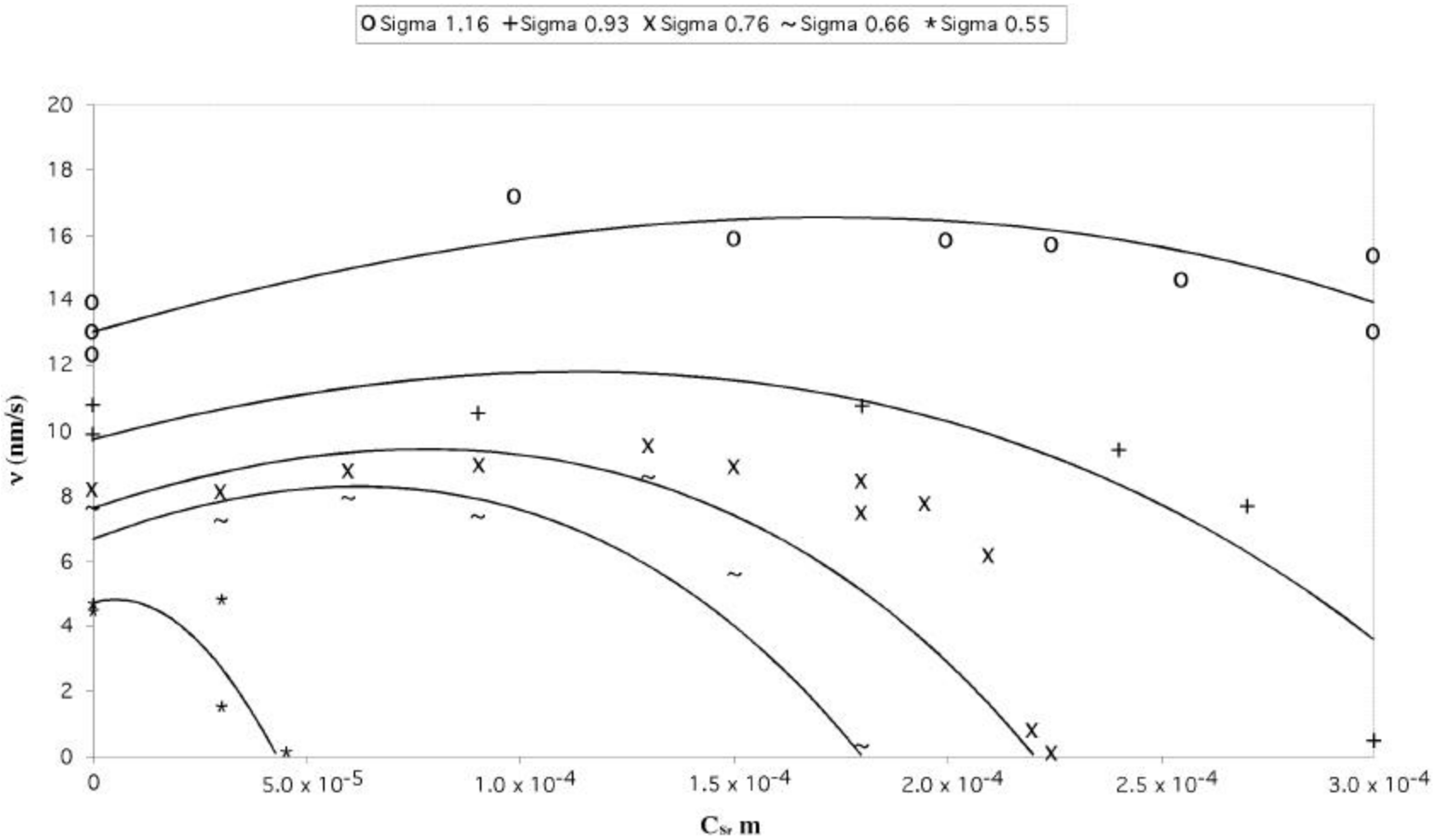

Figure 3-16 Modified modeled calculations of step velocities as a function of strontium concentration along with measured velocities for positive step directions (lines are calculated values).

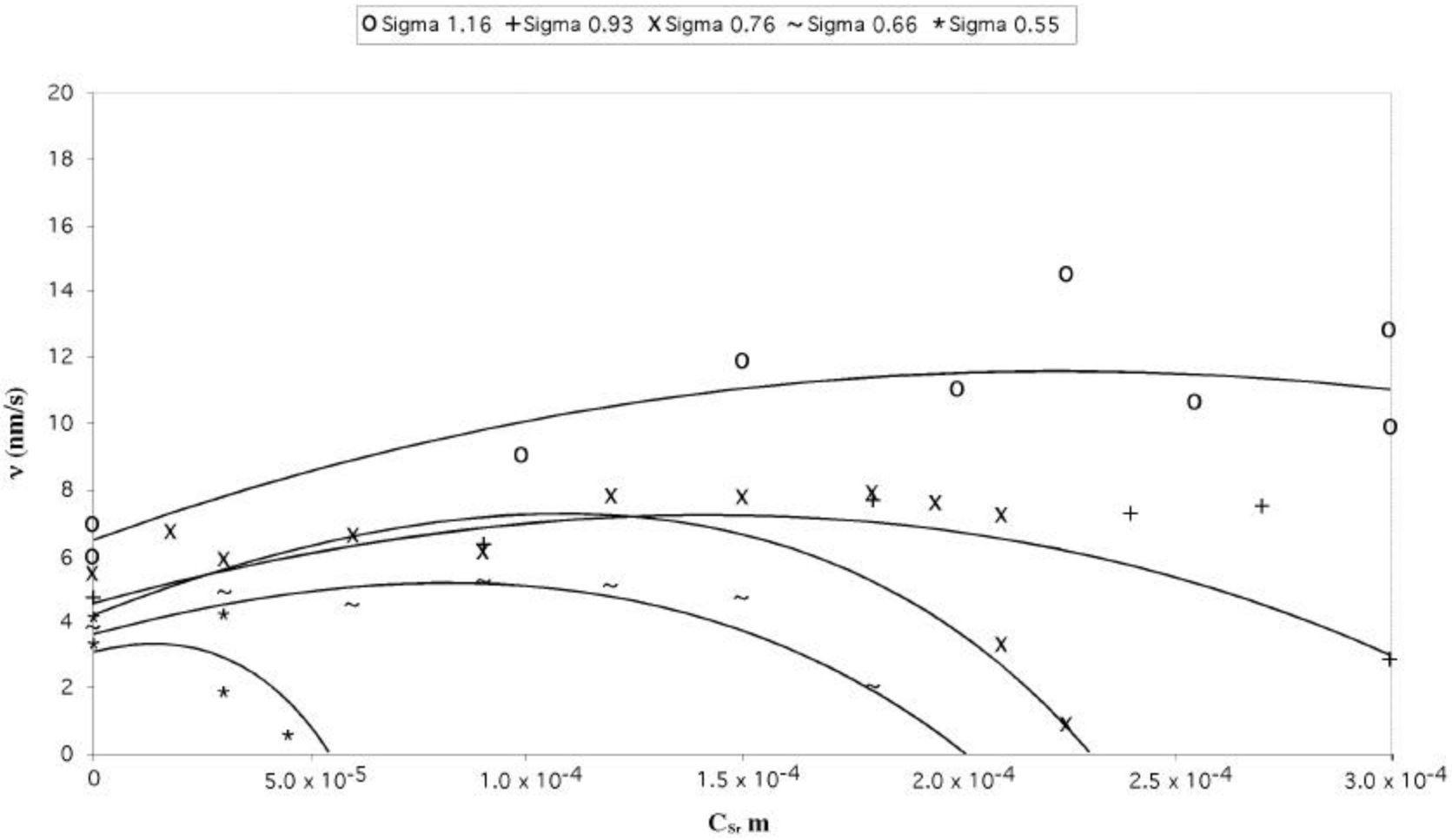

Figure 3-17 Modified modeled calculations of step velocities as a function of strontium concentration along with measured velocities for negative step directions (lines are calculated values).

Chapter 4

Conclusions

This study investigated the nanoscale effects of strontium on calcite growth. By obtaining direct measurements of the growth hillock structure, the surface thermodynamics and kinetics of molecular-scale processes were determined using in situ atomic force microscopy (AFM).

The general behavior of the system in the control solutions (absence of strontium) showed that step velocities for the positive direction were greater than for the negative direction at a given supersaturation. In addition, step velocities increased with increasing supersaturation. This is consistent with previous results.

In the presence of low concentrations of strontium, there is a rate *enhancing* effect. At higher Sr levels, a very strong rate *inhibiting* effect becomes dominant to sharply decrease growth rates to zero over a small incremental increase in strontium concentration. The critical concentration required to initiate growth increases with increasing levels of strontium. When supersaturations exceed σ^*, growth rates further increase to levels that are greater than those measured for the pure calcite system.

To explore reasons for rate enhancement, kinetic and thermodynamic properties were measured and calculated. Kinetic coefficients increase with the addition of low levels of strontium suggesting that rate enhancement is caused by changes in kinetics of growth. Terrace widths (λ) also increase with the addition of low concentrations of strontium. Since increasing λ correlates with a lower apparent supersaturation, rate enhancement is *not* caused by the formation of a material with a lower solubility.

Therefore, strontium appears to affect thermodynamics of growth less than kinetics in causing the observed increase in step velocities.

Established crystal growth impurity models for incorporation and step blocking mechanisms were compared to the findings reported in this study as a qualitative framework for understanding the mechanisms by which strontium modifies growth. The observed rate enhancement at low concentrations of strontium does not fit any of the theoretical models. We propose the introduction of a new model to account for small molecule interactions that can increase the rate of crystal growth. The experimental data that shows rate inhibition at higher strontium concentrations is in agreement with the qualitative step-blocking theoretical model.

Small additions of Sr led to significant changes in hillock morphology. Strontium causes hillocks to elongate perpendicular to the c-glide plane, in contrast with the addition of magnesium, which causes hillocks to elongate parallel to the c-glide plane (Davis, 2000). For a given hillock grown in a solution with a significant concentration of strontium (levels that cause growth rate inhibition), the steps along negative directions appear rough whereas the steps along positive directions appear smoother. This difference in the step edge morphology, along with comparison to crystal growth impurity models, suggests that the rate-inhibition mechanism for the negative direction is the result of long-lived adsorption and pinning at step edges to impede step flow. The smoother step edges seen along positive directions suggests a short-lived adsorption and pinning mechanism at step edges to impede step flow or blocking caused by an accumulation of strontium at step edges due to limited solid solution. This is further explored using Electron Probe Microanalysis (EPMA). According to the results of the

EPMA, strontium appears to be preferentially incorporated into the obtuse step directions, which agrees with observations of Paquette & Reeder (1994) and Reeder (1996).

The data obtained in this study allows us to test the theoretical model for the dependence of step flow rate upon supersaturation when an impurity ion is present to modify growth by the blocking mechanism proposed by Cabrera and Vermilyea (1958). This model does not fit the data set because σ^* as a function of strontium concentration is not independent of supersaturation, as the model assumes.

The findings of this study demonstrate the importance of understanding microscopic processes and the significance of interpreting impurity signatures in the context of step-specific interactions.

References

Berner, R.A. (1975) The role of magnesium in the crystal growth of calcite and aragonite from sea water. *Geochimica et Cosmochimica Acta* **39**, 489-504.

Berner, E.K. and Berner, R.A. (1996) *Global Environment*, Prentice Hall

Burton, W.K., Cabrera, N. and Frank, F.C. (1951) The Growth of Crystals and the Equilibrium Structure of their Surfaces *Phil. Trans. R. Soc.* **243**, 299.

Cabrera, N. and Vermilyea, D.A. (1958) The Growth of Crystals from Solution. In *Growth and Perfection of Crystals* (eds. R.H. Doremus, B.W. Roberts and D. Turnbull), 393-410, Wiley, New York.

Chernov, A.A. (1961) The spiral growth of crystals. *Soviet Phys.* **4**, 116-148.

Davis, K.J. (2000) *Magnesium as an Impurity in Calcite Growth: Thermodynamic and Kinetic Controls on Biomineral Formation.* MS Thesis. Georgia Institute of Technology.

Davis, K.J., Dove, P.M., Wasylenki, L.E. and De Yoreo, J.J. (in review) Morphological consequences of differential Mg^{2+} incorporation at structurally distinct steps on calcite. *American Mineralogist*.

De Leeuw, N.H., Harding, J.H. and Parker, S.C. (2002) Molecular dynamics simulations of the incorporation of Mg^{2+}, Cd^{2+} and Sr^{2+} at calcite growth steps: Introductions of $SrCO_3$ potential model. *Molecular Simulation*, **28**, 573-589.

Dove, P.M., and Davis, K.J. (in press) Inorganic controls on biominerals formation. In *From Fluid-Solid Interfaces to Nanostructural Engineering* (eds. J.J. De Yoreo and X.Y. Liu), Plenum/Kluwer Academic Press.

Elderfield, H., Bertram, C.J. and Erez, J. (1996) A biomineralization model for the incorporation of trace elements into foraminiferal calcium carbonate. *Earth and Planetary Science Letters* **142**, 409-423.

Graham, D.W., Bender, M.L., Williams, D.F. and Keigwin, L.D. (1982) Strontium-calcium ratios in Cenozoic planktonic foraminifera. *Geochim. Cosmochim. Acta* **46**, 1281-1292.

Gratz, A.J., Hillner, P.E. and Hansma, P.K. (1993) Step dynamics and spiral growth on calcite. *Geochim. Cosmochim. Acta* **57**, 491-495.

Lea, D.W. (1999) *Modern Foraminifera*, Springer-Verlag, Berlin.

Lowenstam, H. A. and Weiner, S. (1989) *On Mineralization*, Oxford Uni. Press, New York.

Mann, S. (2001) *Biomineralization – Principles and Concepts in Bioinorganic Materials Chemistry*, Oxford Uni. Press, New York.

Meyer, H.J. (1984) The influence of impurities on the growth rate of calcite. *Journal of Crystal Growth*, **66**, 639-646.

Morse, J.W. and Bender, M.L. (1990) Partition coefficients in calcite: Examination of factors influencing the validity of experimental results and their application to natural systems. *Chemical Geology*, **82**, 265-277.

Morse, J.W. and Mackenzie, F.T. (1990) *Geochemistry of Sedimentary Carbonates*, Elsevier, Amsterdam.

Mucci, A. and Morse, J.W. (1983) The incorporation of Mg^{2+} and Sr^{2+} into calcite overgrowths: influences if growth rate and solution composition. *Geochim. Cosmochim. Acta* **47**, 217-233.

Paquette, J. and Reeder, R.J. (1995) Relationship between surface structure, growth mechanism, and trace element incorporation in calcite. *Geochim. Cosmochim. Acta* **59**, 735-749.

Pingitore, N.E., Lytle, F.W., Davies, B.M., Eastman, M.P., Eller, P.G. and Larson, E.M. (1992) Mode of incorporation of Sr^{2+} in calcite: Determination by X-ray absorption spectroscopy. *Geochim. Cosmochim. Acta* **56**, 1531-1538.

Plummer, L.N. and Busenberg, E. (1982) The solubilities of calcite, aragonite and vaterite in CO_2-H_2O solutions between 0 and 90^{o}C, and an evaluation of the aqueous model for the system $CaCO_3$-CO_2-H_2O. *Geochimica et Cosmochimica Acta* **46**, 1011-1040.

Pouchou, J. L. and Pichoir, F. (1985) "PAP" $\Phi(\rho Z)$ Procedure for Improved Quantitative Microanalysis. In *Microbeam Analysis* (ed. J. T. Armstrong), 104, San Francisco Press, Inc., San Francisco, California.

Purton, L.M.A., Shields, G.A., Brasier, M.D. and Grime, G.W. (1999) Metabolism controls Sr/Ca ratios in fossil aragonitic mollusks. *Geology*, **27**, 1083-1086.

Rathburn, A.E. and De Deckker, P. (1997) Magnesium and strontium compositions of Recent benthic foraminifera from the Coral Sea, Australia and Prydz Bay, Antarctica. *Marine Micropaleontology* **32**, 231-248.

Reddy, M.M. and Wang, K.K. (1980) Crystallization of Calcium Carbonate in the Presence of Metal Ions. I. Inhibition by Magnesium ion at pH 8.8 and 25°C. *Journal of Crystal Growth* **50**, 470-480.

Reeder, R.J. (1983) Crystal Chemistry of the Rhombohedral Carbonates. In *Reviews in Mineralogy: Carbonates: Mineralogy and Chemistry* (ed. R.J. Reeder), **11**, 1-47, Mineralogical Society of America, Washington, DC.

Reeder, R.J. (1996) Interaction of divalent cobalt, zinc, cadmium, and barium with calcite Surface during layer growth. *Geochim. Cosmochim. Acta* **60**, 1543-1552.

Rosenthal, Y., Boyle, E.A. and Slowey, N. (1997) Temperature control on the incorporation of magnesium, strontium, fluorine, and cadmium into benthic foraminiferal shells from Little Bahama Bank: Prospects for thermocline paleoceanography. *Geochim. Cosmochim. Acta* **61**, 3633-3643.

Speer, J.A. (1983) Crystal Chemistry and Phase Relations of Orthorhombic Carbonates. In *Reviews in Mineralogy: Carbonates: Mineralogy and Chemistry* (ed. R.J. Reeder), **11**, 145-190, Mineralogical Society of America, Washington, DC.

Stoll, H.M., Rosenthal, Y. and Falkowsky, P. (2002) Climate proxies from Sr/Ca of coccolith calcite: Calibrations from continuous culture of Emiliania huxleyi. *Geochim. Cosmochim. Acta* **66**, 927-936.

Teng, H.H., Dove, P.M., Orme, C.A., and De Yoreo, J.J. (1998) The thermodynamics of calcite growth: A baseline for understanding biomineral formation. *Science* **282**, 724-727.

Teng, H.H., Dove, P.M. and De Yoreo, J.J. (2000) Kinetics of calcite growth: Surface processes and relationships to macroscopic rate laws. *Geochimica et Cosmochimica Acta* **64**, 2255-2266.

Tesoriero, A.J. and Pankow, J.F. (1996) Solid solution partitioning of Sr^{2+}, Ba^{2+}, and Cd^{2+} to calcite. *Geochim. Cosmochim. Acta* **60**, 1053-1063.

van Enckevort, W.J.P. and van der Berg, A.C.J.F. (1998) Impurity blocking of crystal growth: a Monte Carlo study. *J. Crystal Growth* **183**, 441-455.

Voronkov, V.V. and Rashkovich, L.N. (1992) Influence of a mobile adsorbed impurity on the motion of steps. *Sov. Phys. Crystallogr.* **37**, 289-295.

Appendix A

Atomic Force Microscopy (AFM) Images of Calcite Growth Hillocks

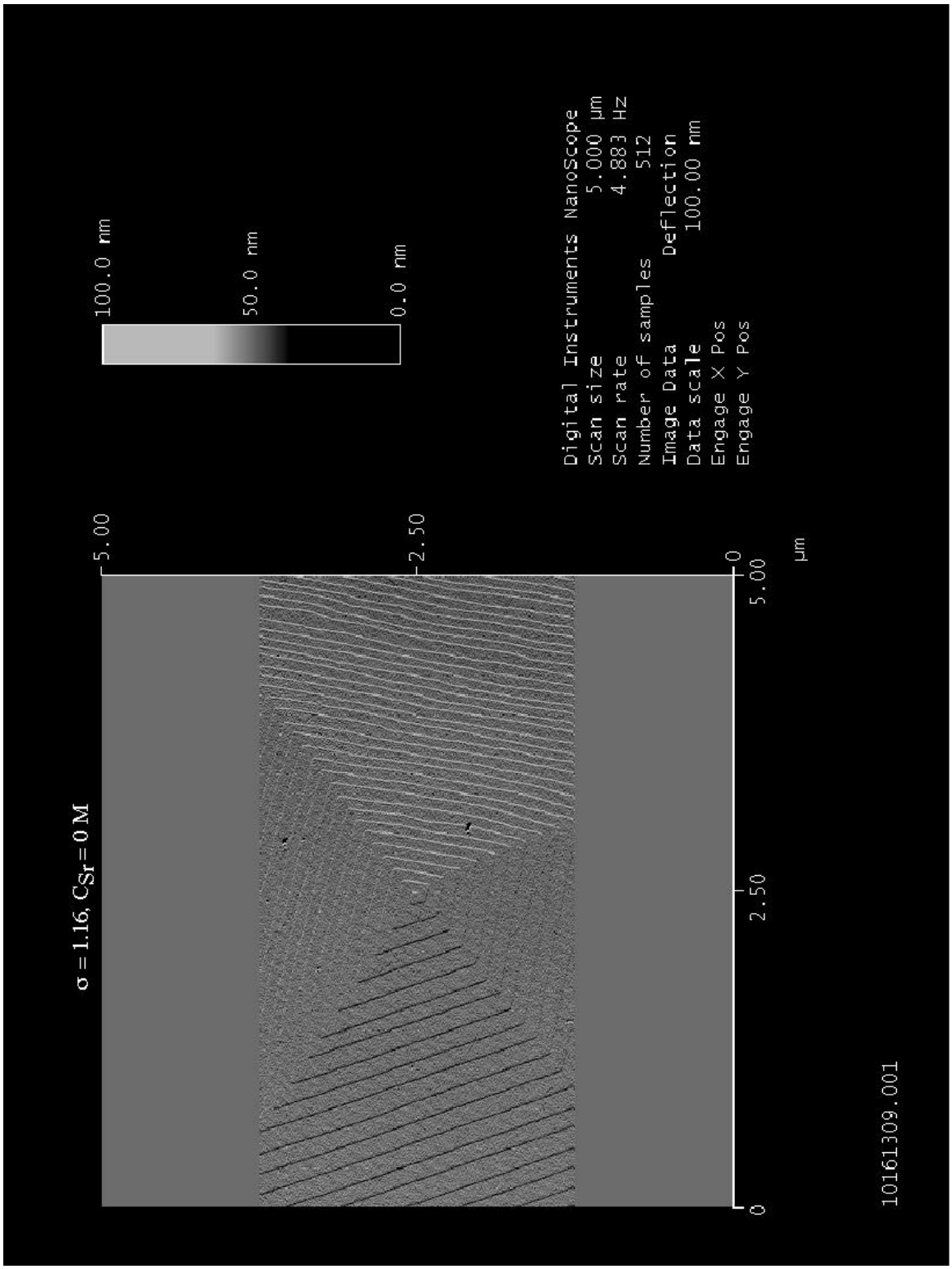
σ = 1.16, CSr = 0 M
100.0 nm
50.0 nm
0.0 nm
Digital Instruments NanoScope
Scan size 5.000 µm
Scan rate 4.883 Hz
Number of samples 512
Image Data Deflection
Data scale 100.00 nm
Engage X Pos
Engage Y Pos
5.00
2.50
0
0
2.50
5.00
µm
10161309.001

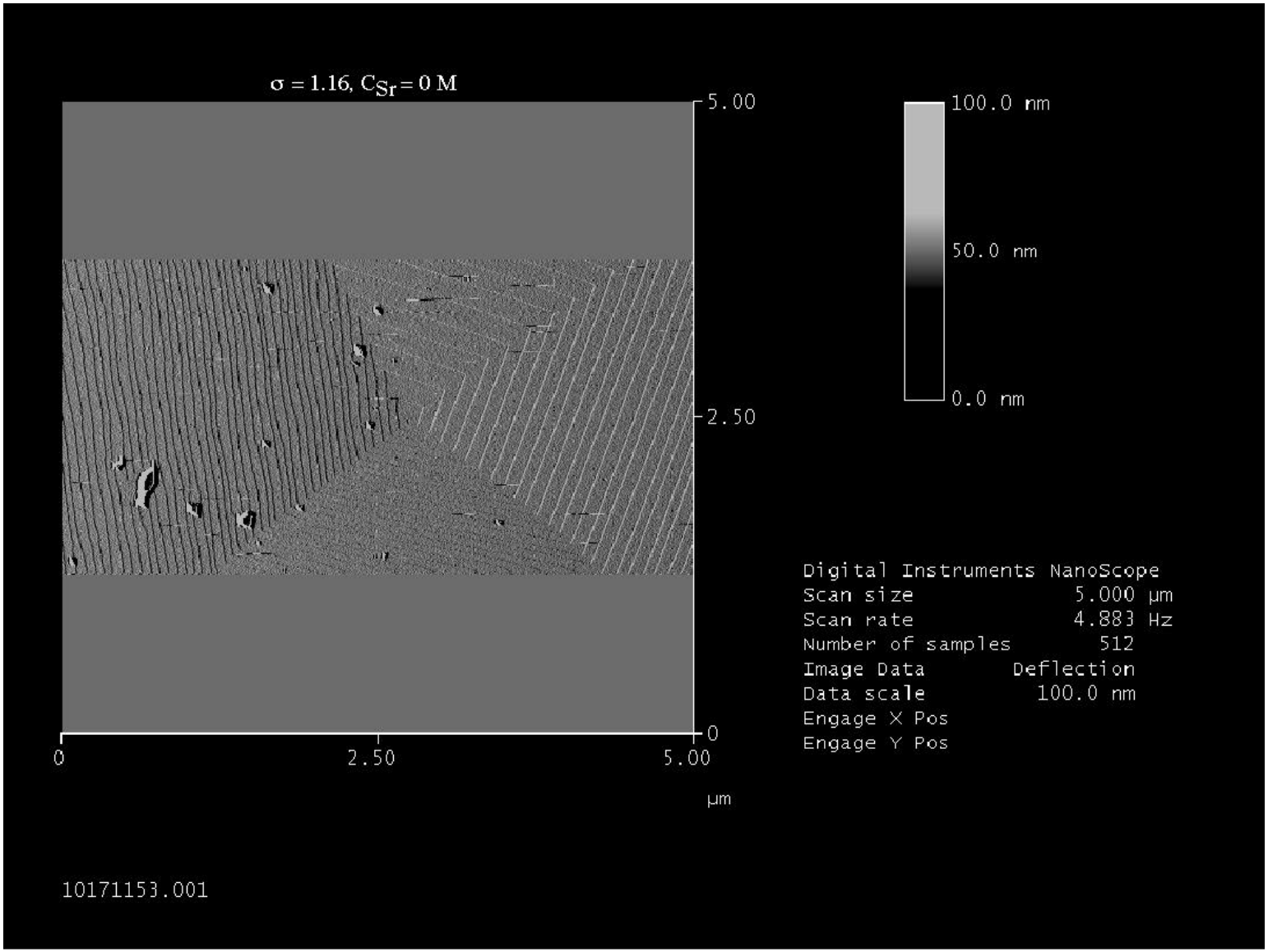
σ = 1.16, C_{Sr} = 0 M
5.00
2.50
0
0
2.50
5.00
µm
100.0 nm
50.0 nm
0.0 nm
Digital Instruments NanoScope
Scan size 5.000 µm
Scan rate 4.883 Hz
Number of samples 512
Image Data Deflection
Data scale 100.0 nm
Engage X Pos
Engage Y Pos
10171153.001

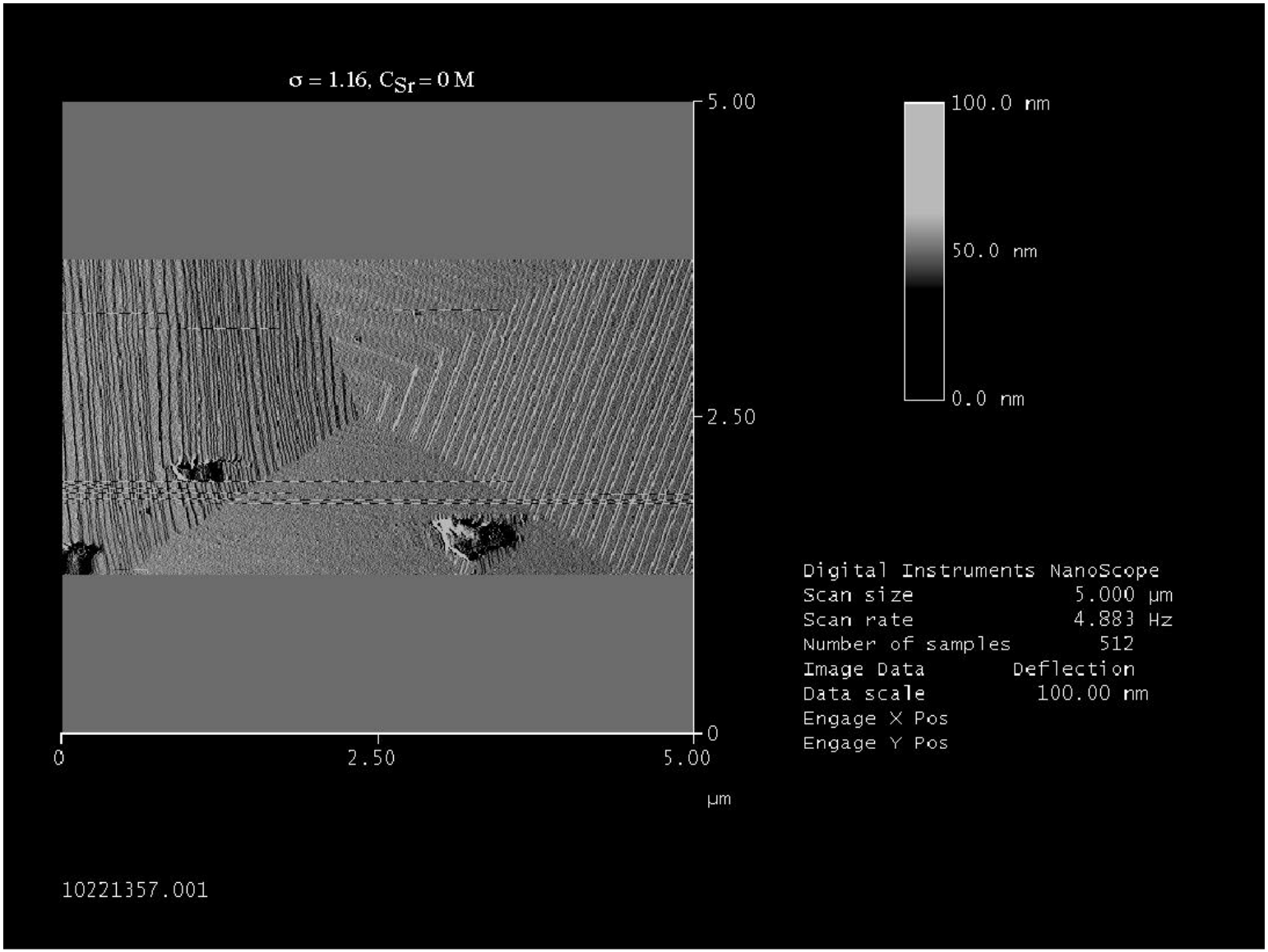
σ = 1.16, C_{Sr} = 0 M
5.00
2.50
0
0
2.50
5.00
µm
100.0 nm
50.0 nm
0.0 nm
Digital Instruments NanoScope
Scan size 5.000 µm
Scan rate 4.883 Hz
Number of samples 512
Image Data Deflection
Data scale 100.00 nm
Engage X Pos
Engage Y Pos
10221357.001

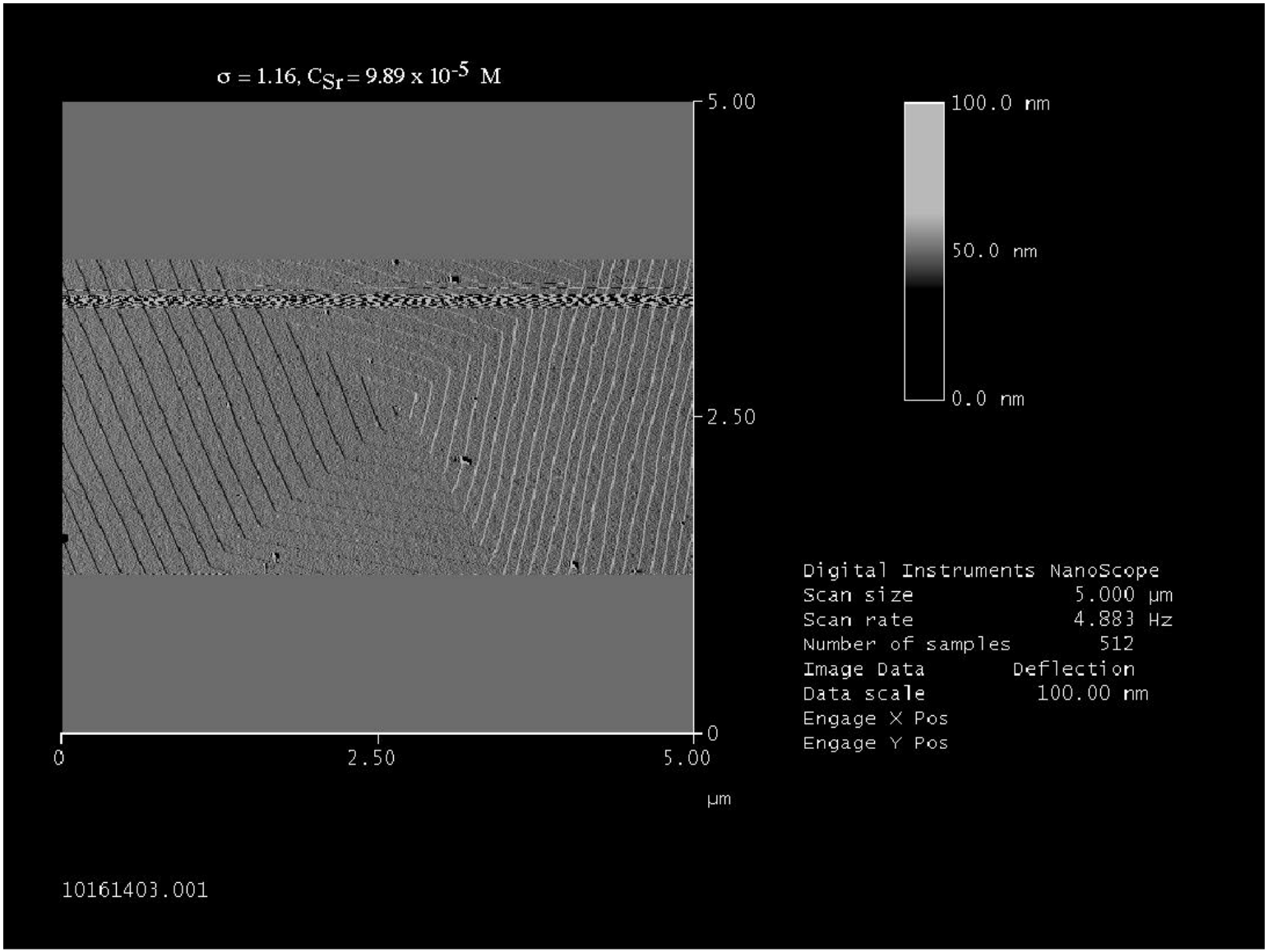
σ = 1.16, C_{Sr} = 9.89 x 10^{-5} M
5.00
2.50
0
0
2.50
5.00
µm
100.0 nm
50.0 nm
0.0 nm
Digital Instruments NanoScope
Scan size 5.000 µm
Scan rate 4.883 Hz
Number of samples 512
Image Data Deflection
Data scale 100.00 nm
Engage X Pos
Engage Y Pos
10161403.001

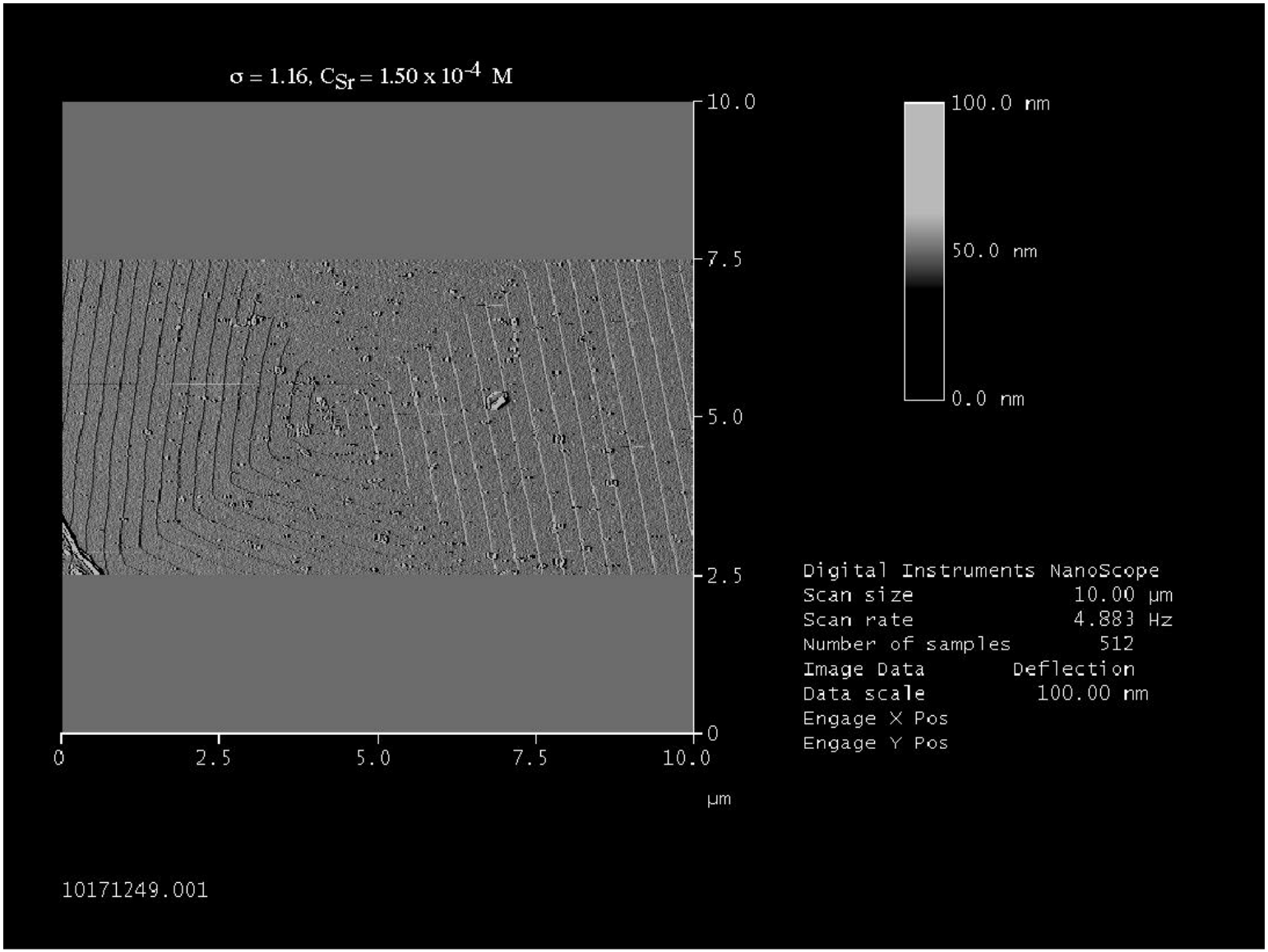
σ = 1.16, C_{Sr} = 1.50 x 10^{-4} M
10.0
7.5
5.0
2.5
0
0
2.5
5.0
7.5
10.0
µm
100.0 nm
50.0 nm
0.0 nm
Digital Instruments NanoScope
Scan size 10.00 µm
Scan rate 4.883 Hz
Number of samples 512
Image Data Deflection
Data scale 100.00 nm
Engage X Pos
Engage Y Pos
10171249.001

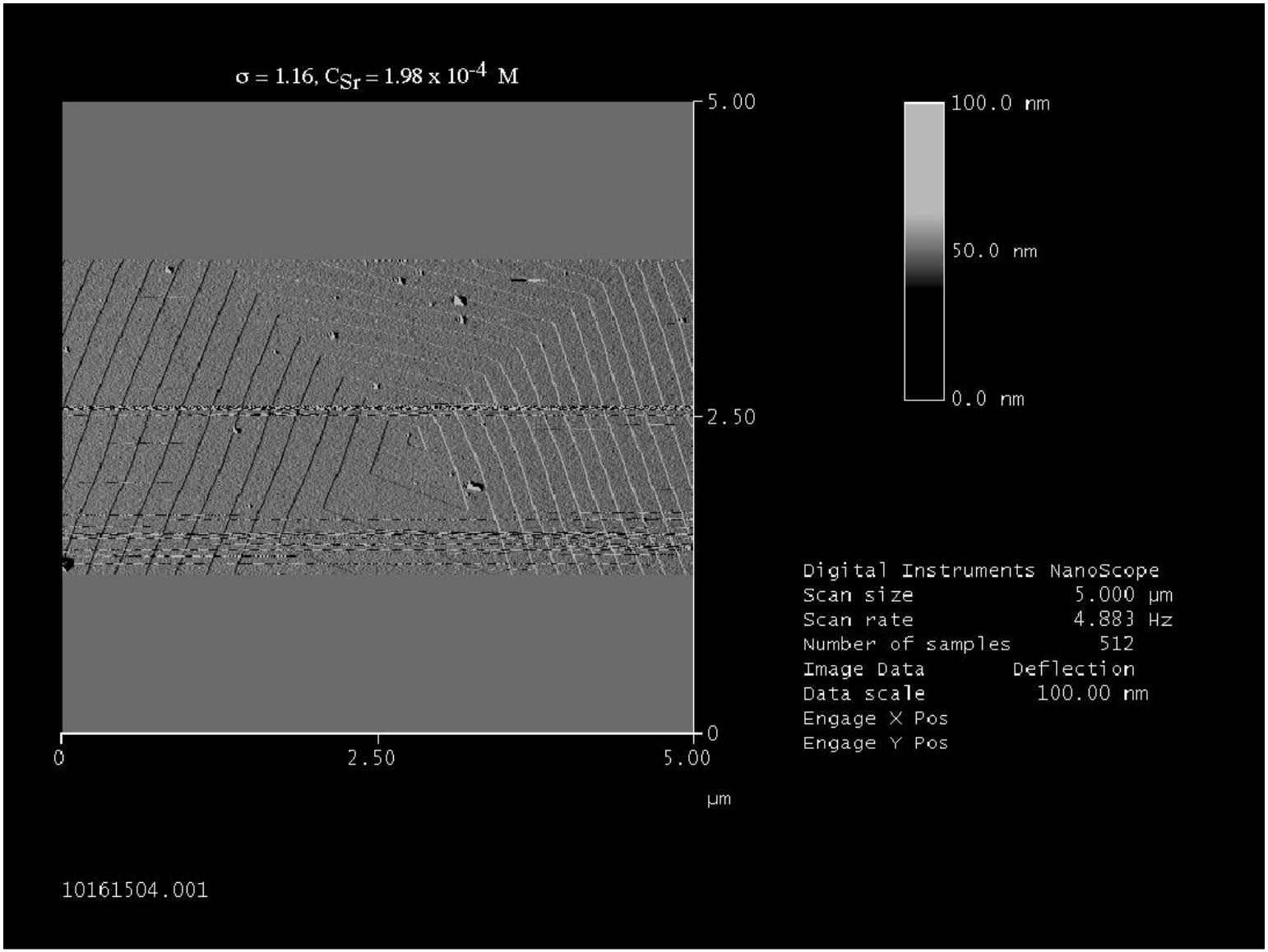
σ = 1.16, C_{Sr} = 1.98 x 10^{-4} M
5.00
2.50
0
0
2.50
5.00
µm
100.0 nm
50.0 nm
0.0 nm
Digital Instruments NanoScope
Scan size 5.000 µm
Scan rate 4.883 Hz
Number of samples 512
Image Data Deflection
Data scale 100.00 nm
Engage X Pos
Engage Y Pos
10161504.001

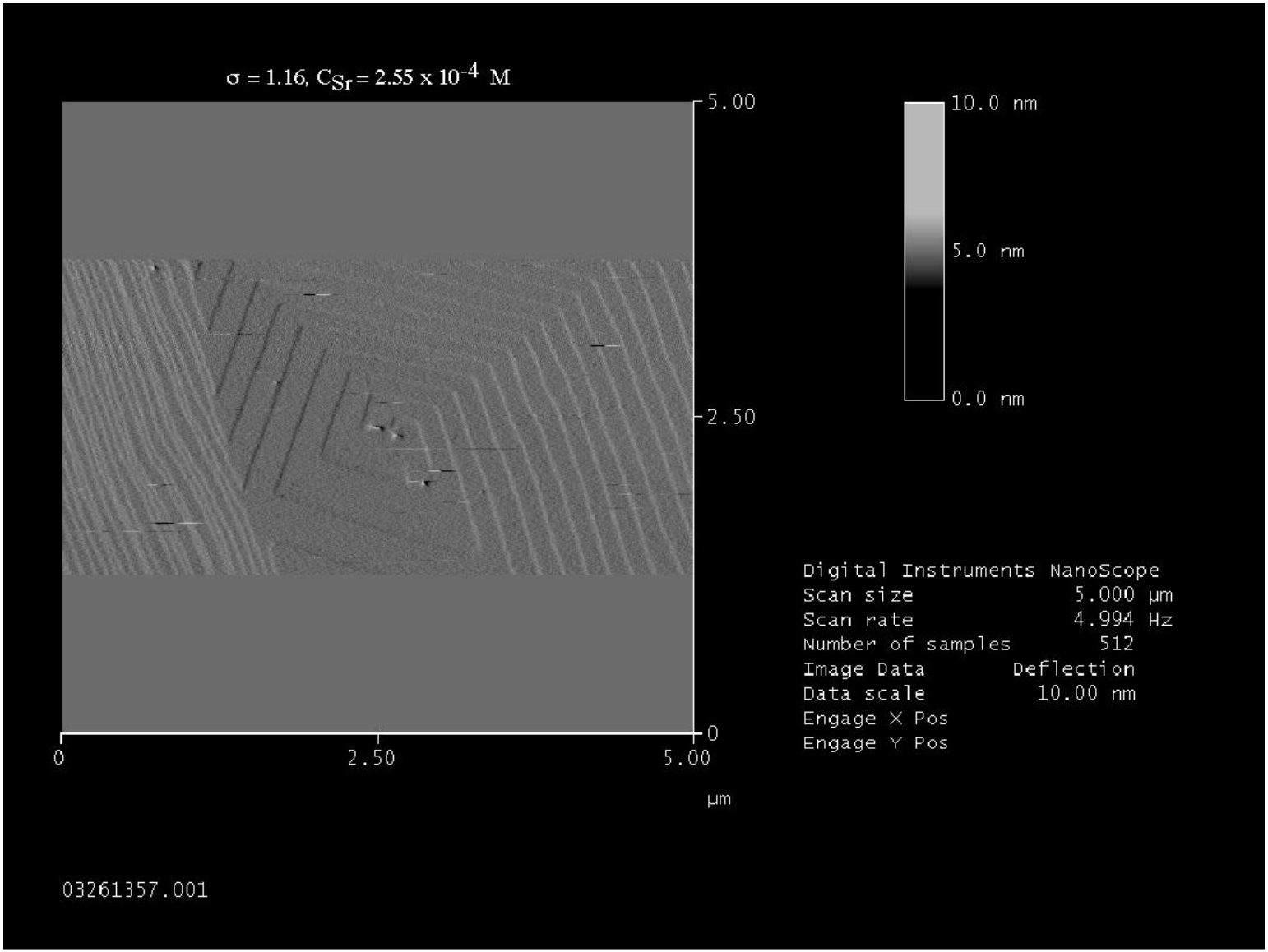
σ = 1.16, C_{Sr} = 2.55 x 10^{-4} M
5.00
2.50
0
0
2.50
5.00
µm
10.0 nm
5.0 nm
0.0 nm
Digital Instruments NanoScope
Scan size 5.000 µm
Scan rate 4.994 Hz
Number of samples 512
Image Data Deflection
Data scale 10.00 nm
Engage X Pos
Engage Y Pos
03261357.001

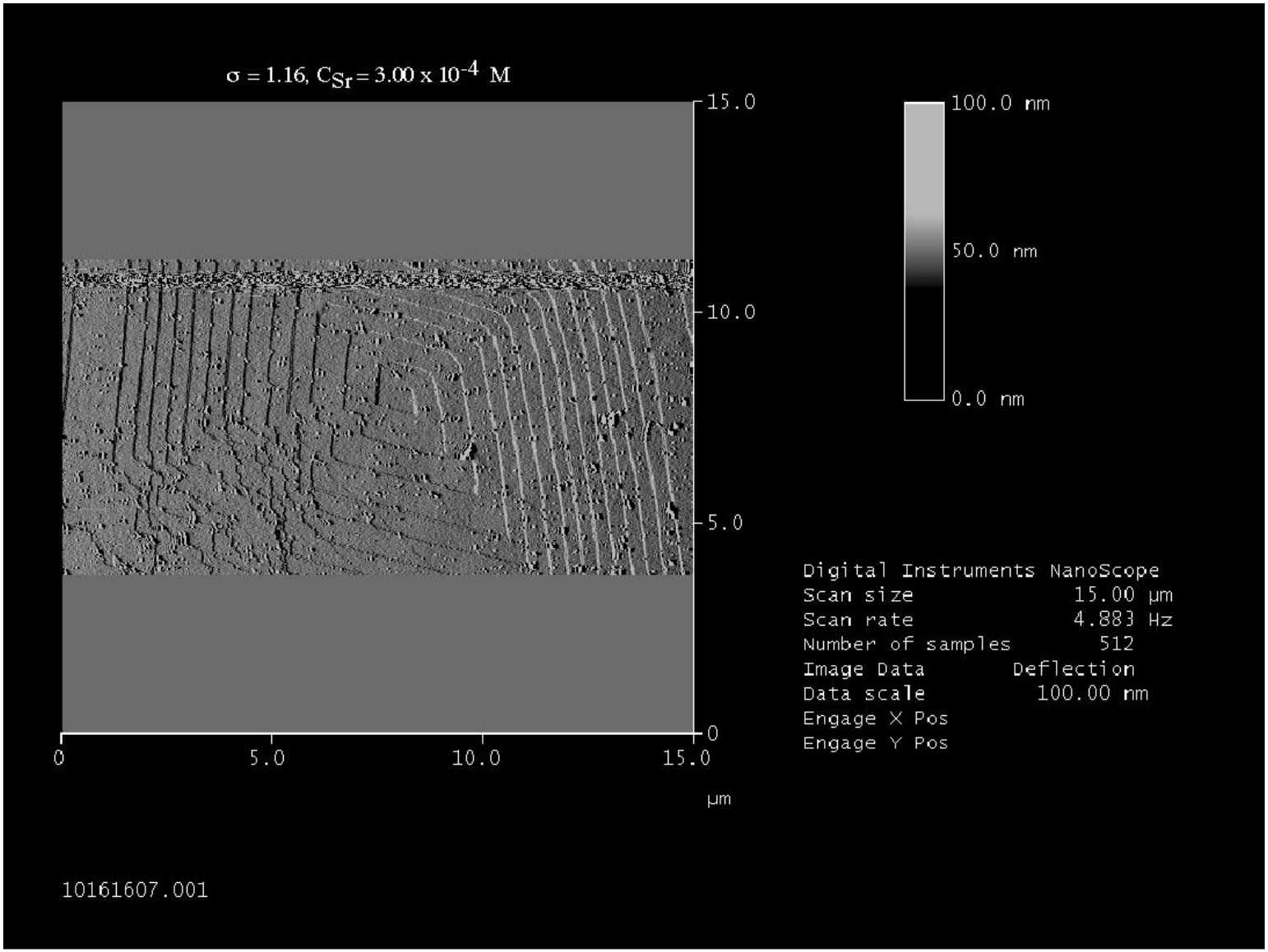
σ = 1.16, C_{Sr} = 3.00 x 10^{-4} M
15.0
10.0
5.0
0
0
5.0
10.0
15.0
µm
100.0 nm
50.0 nm
0.0 nm
Digital Instruments NanoScope
Scan size 15.00 µm
Scan rate 4.883 Hz
Number of samples 512
Image Data Deflection
Data scale 100.00 nm
Engage X Pos
Engage Y Pos
10161607.001

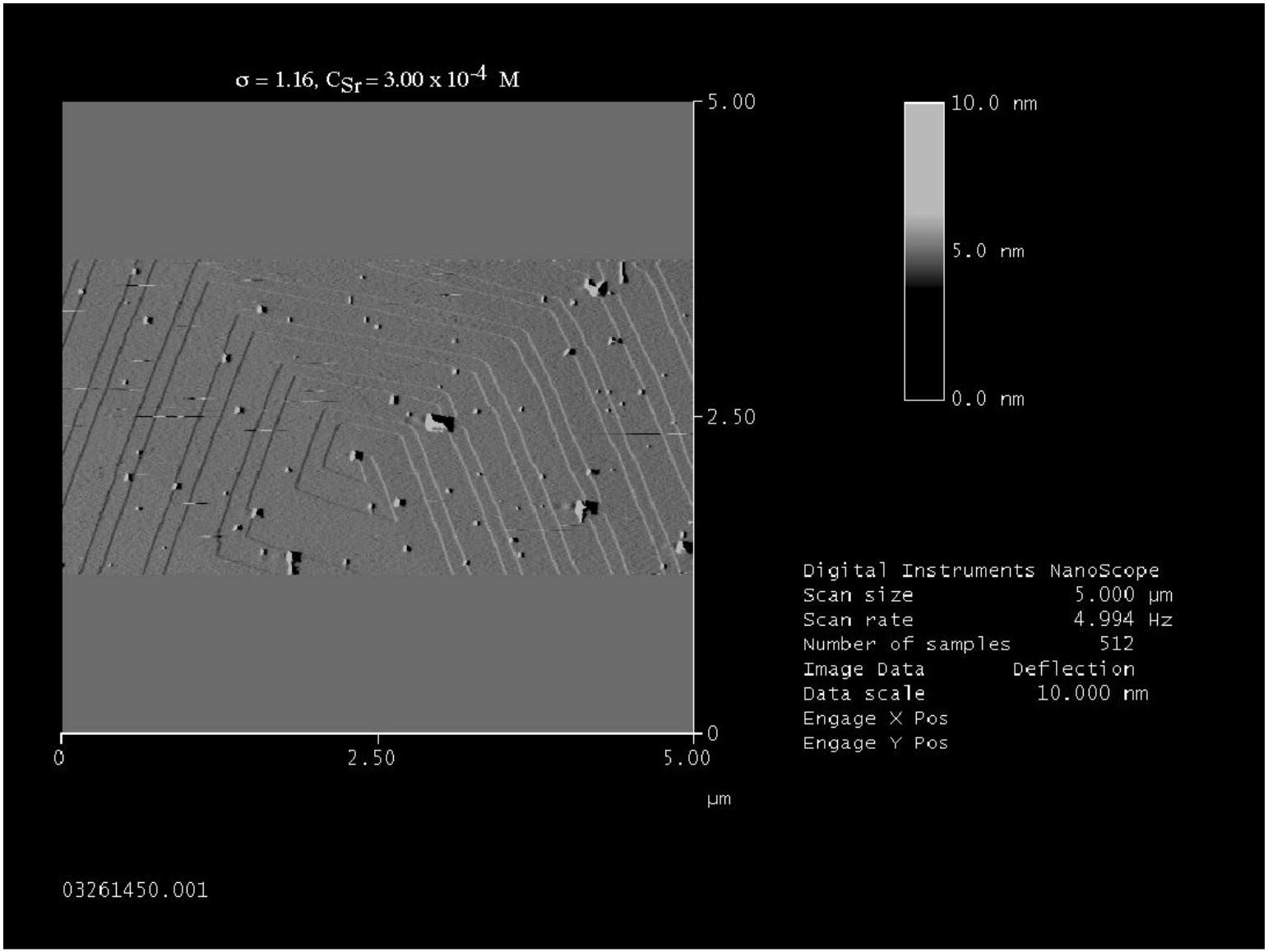
σ = 1.16, C_{Sr} = 3.00 x 10^{-4} M
5.00
2.50
0
0
2.50
5.00
µm
10.0 nm
5.0 nm
0.0 nm
Digital Instruments NanoScope
Scan size 5.000 µm
Scan rate 4.994 Hz
Number of samples 512
Image Data Deflection
Data scale 10.000 nm
Engage X Pos
Engage Y Pos
03261450.001

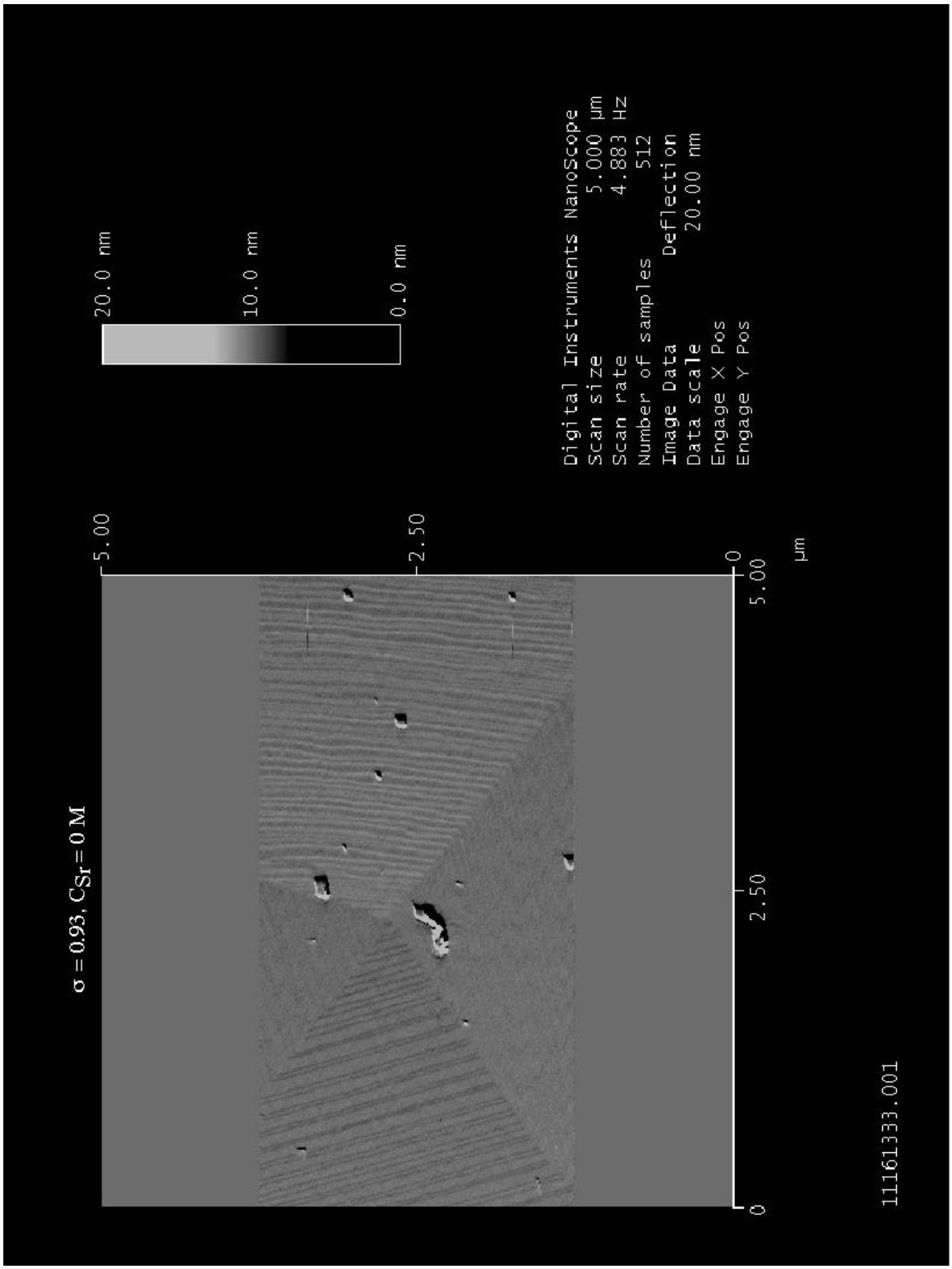
σ = 0.93, C_{Sr} = 0 M
20.0 nm
10.0 nm
0.0 nm
Digital Instruments NanoScope
Scan size 5.000 µm
Scan rate 4.883 Hz
Number of samples 512
Image Data Deflection
Data scale 20.00 nm
Engage X Pos
Engage Y Pos
5.00
2.50
0
2.50
5.00
µm
11161333.001

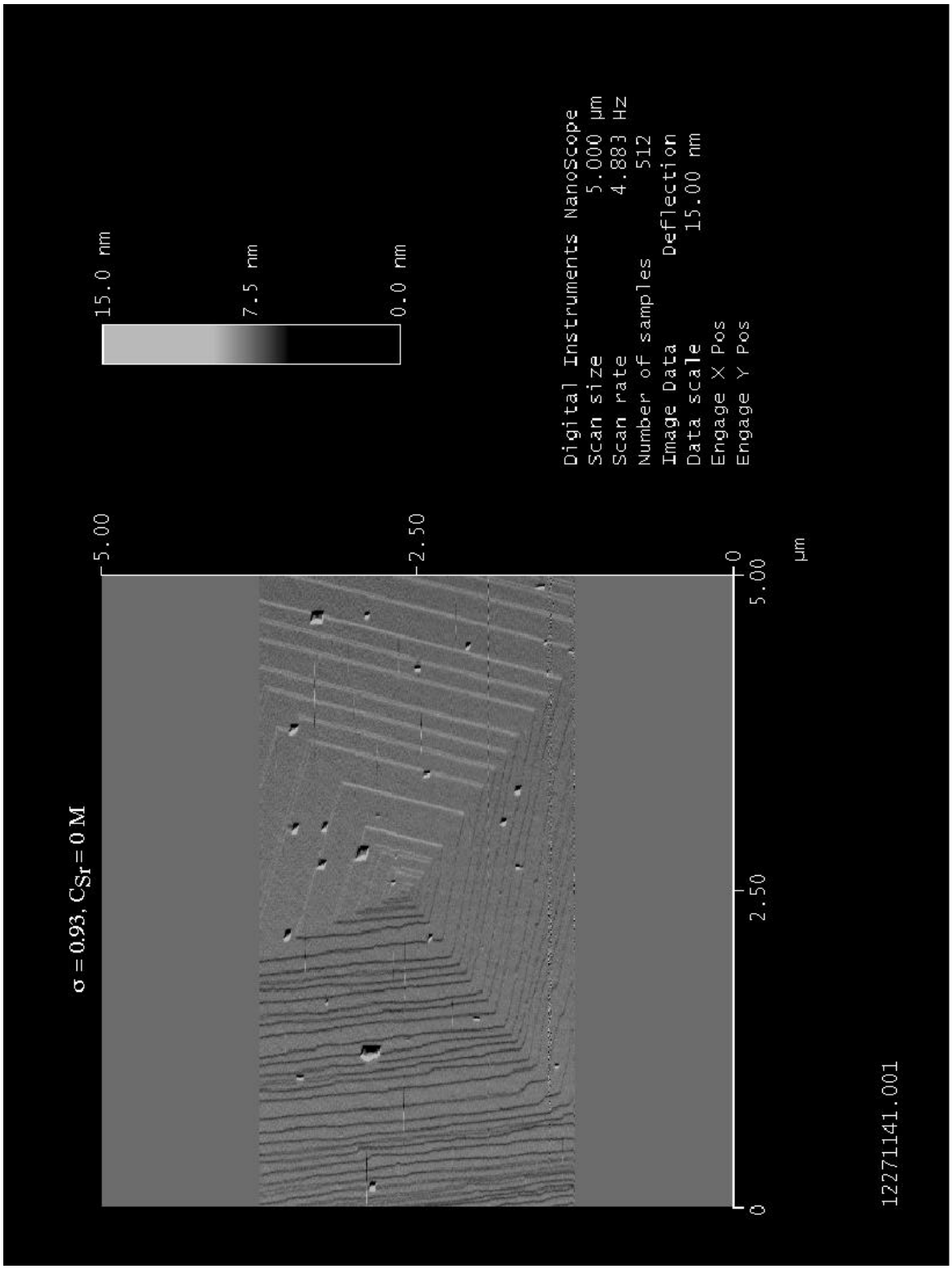
σ = 0.93, CSr = 0 M
15.0 nm
7.5 nm
0.0 nm
Digital Instruments NanoScope
Scan size 5.000 µm
Scan rate 4.883 Hz
Number of samples 512
Image Data Deflection
Data scale 15.00 nm
Engage X Pos
Engage Y Pos
5.00
2.50
0
0
2.50
5.00
µm
12271141.001

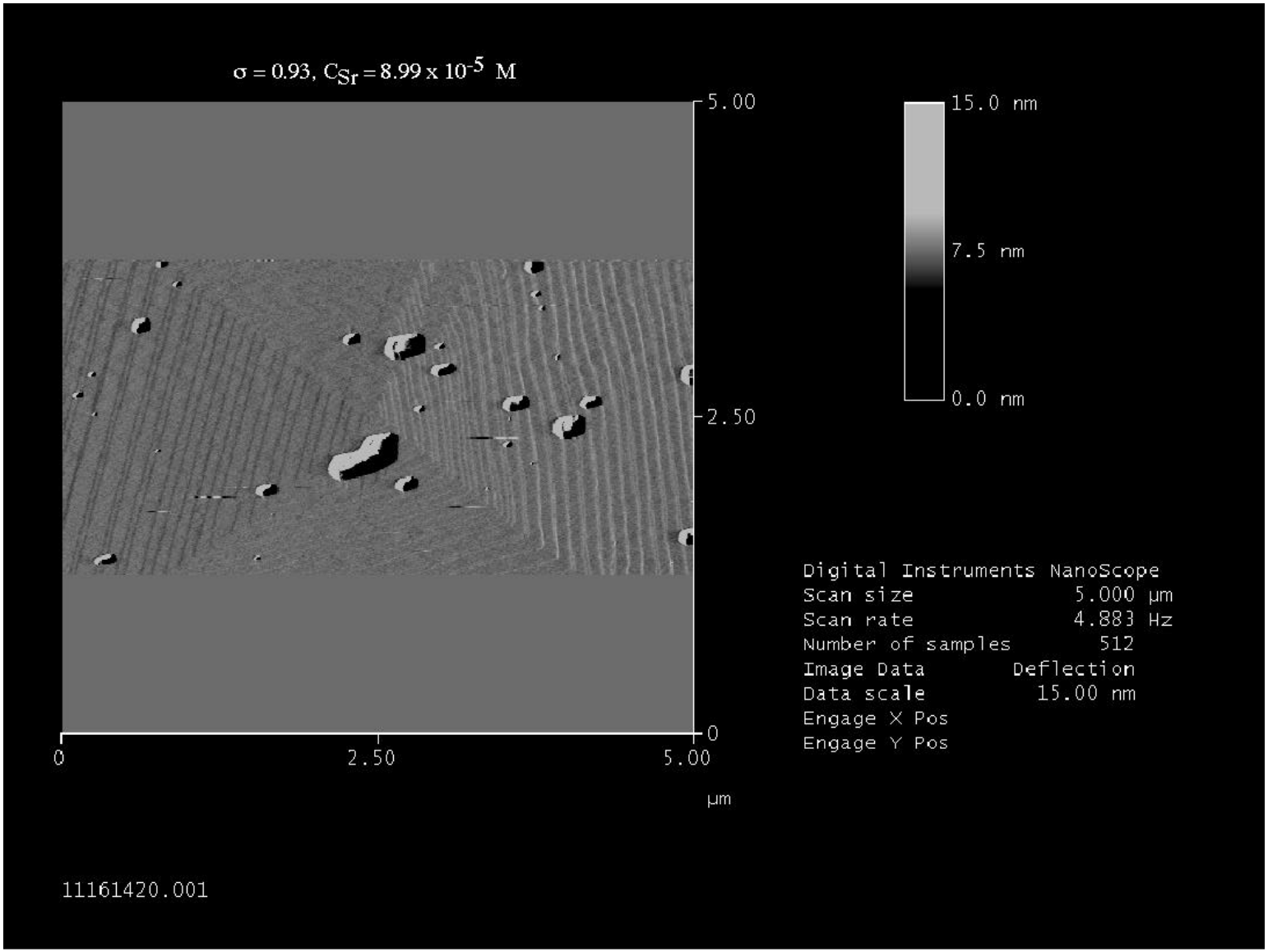
σ = 0.93, C_{Sr} = 8.99 x 10^{-5} M
5.00
2.50
0
0
2.50
5.00
µm
15.0 nm
7.5 nm
0.0 nm
Digital Instruments NanoScope
Scan size 5.000 µm
Scan rate 4.883 Hz
Number of samples 512
Image Data Deflection
Data scale 15.00 nm
Engage X Pos
Engage Y Pos
11161420.001

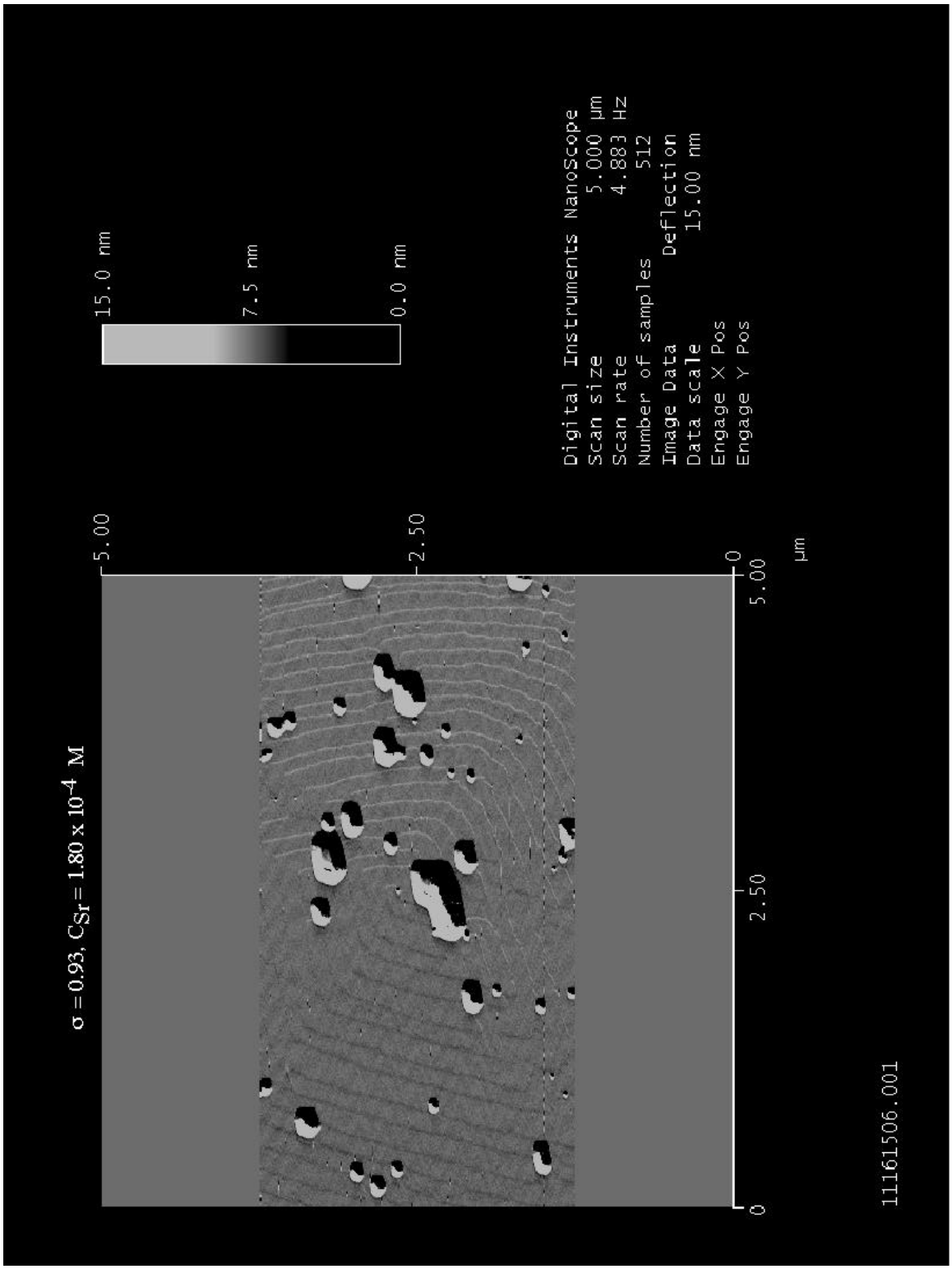
σ = 0.93, CSr = 1.80 x 10-4 M
15.0 nm
7.5 nm
0.0 nm
Digital Instruments NanoScope
Scan size 5.000 µm
Scan rate 4.883 Hz
Number of samples 512
Image Data Deflection
Data scale 15.00 nm
Engage X Pos
Engage Y Pos
5.00
2.50
0
0
2.50
5.00
µm
11161506.001

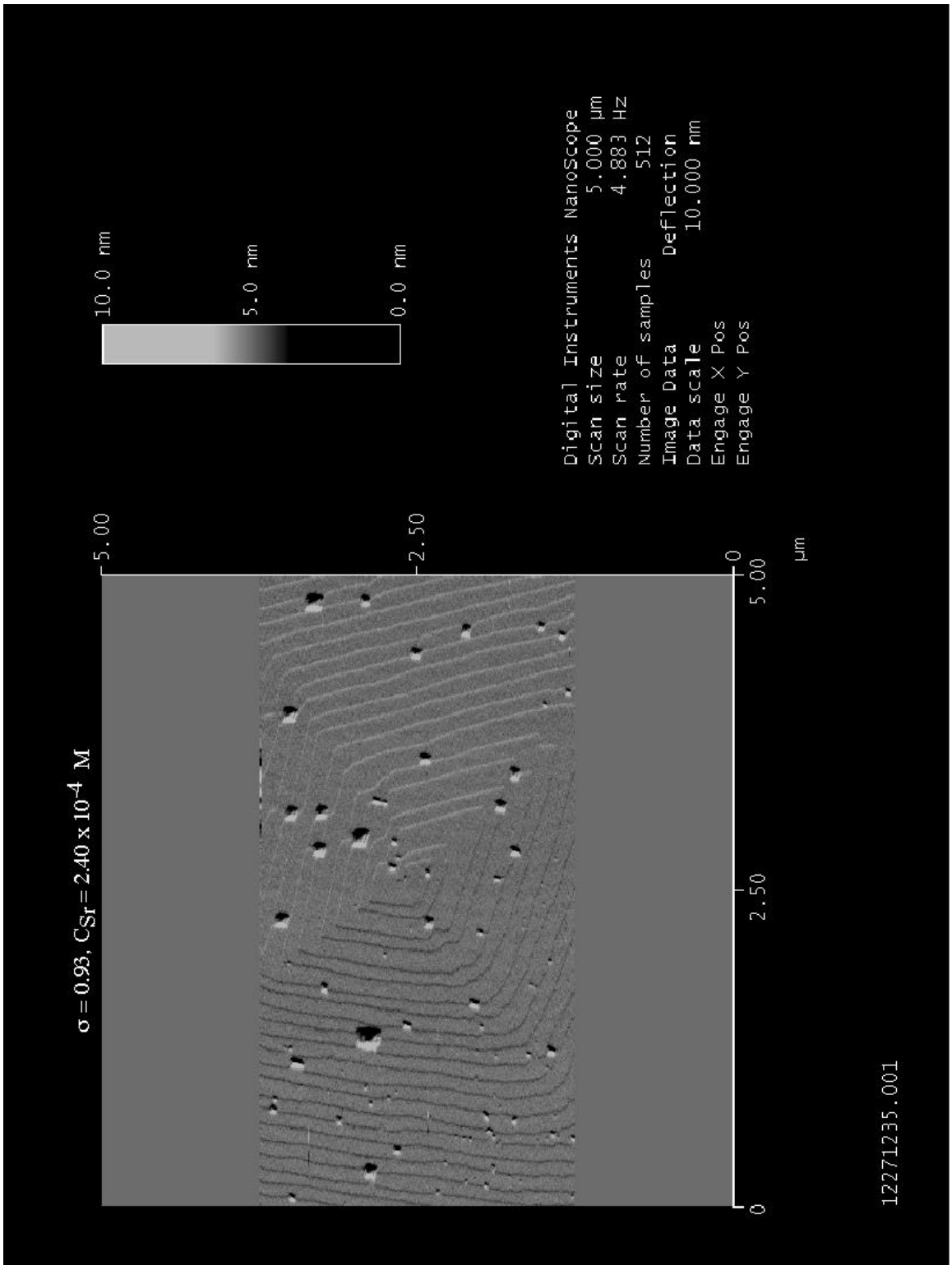
σ = 0.93, C_{Sr} = 2.40 x 10^{-4} M
10.0 nm
5.0 nm
0.0 nm
Digital Instruments NanoScope
Scan size 5.000 µm
Scan rate 4.883 Hz
Number of samples 512
Image Data Deflection
Data scale 10.000 nm
Engage X Pos
Engage Y Pos
5.00
2.50
0
0
2.50
5.00
µm
12271235.001

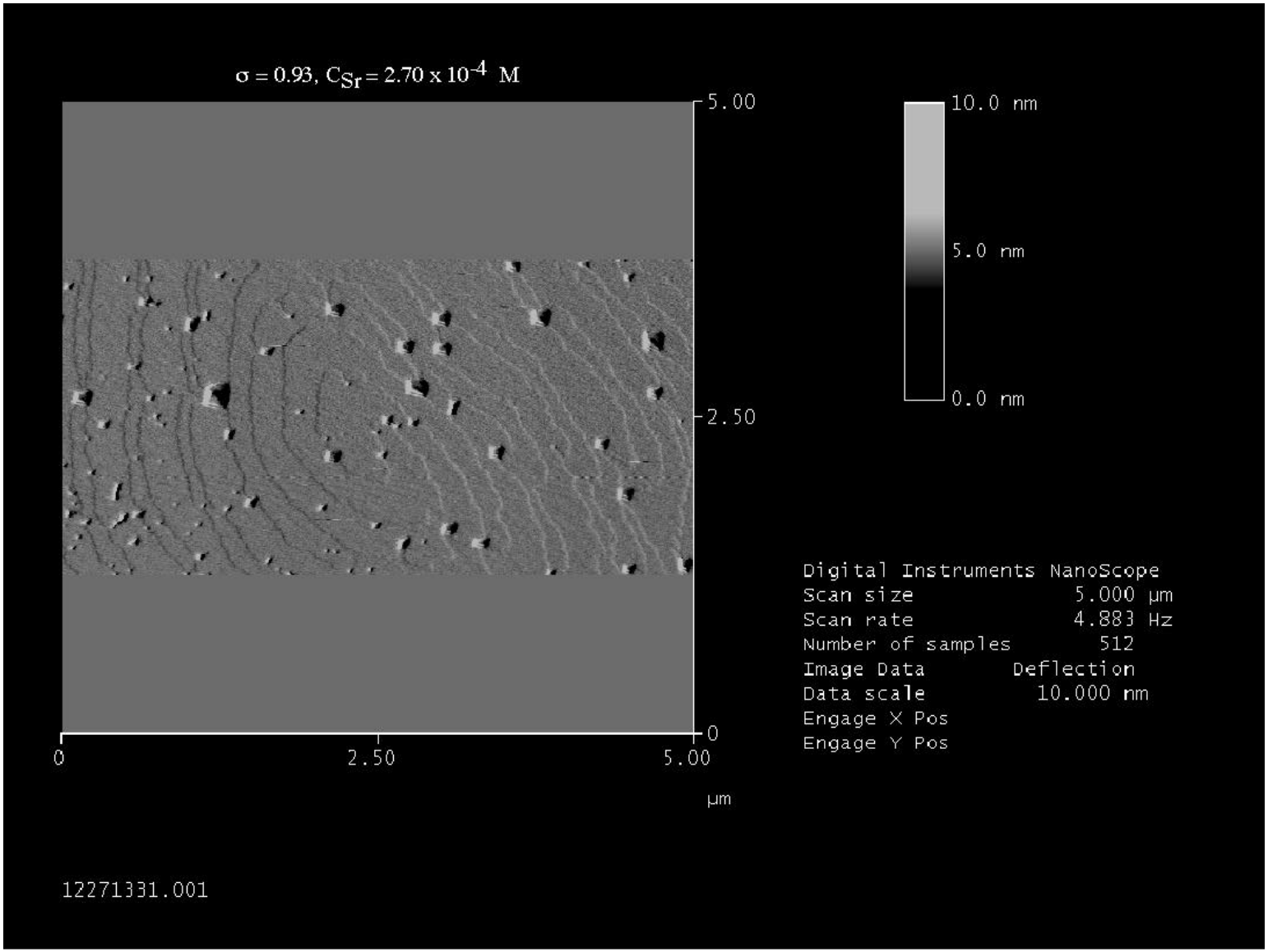
σ = 0.93, C_{Sr} = 2.70 x 10^{-4} M
5.00
2.50
0
0
2.50
5.00
µm
10.0 nm
5.0 nm
0.0 nm
Digital Instruments NanoScope
Scan size 5.000 µm
Scan rate 4.883 Hz
Number of samples 512
Image Data Deflection
Data scale 10.000 nm
Engage X Pos
Engage Y Pos
12271331.001

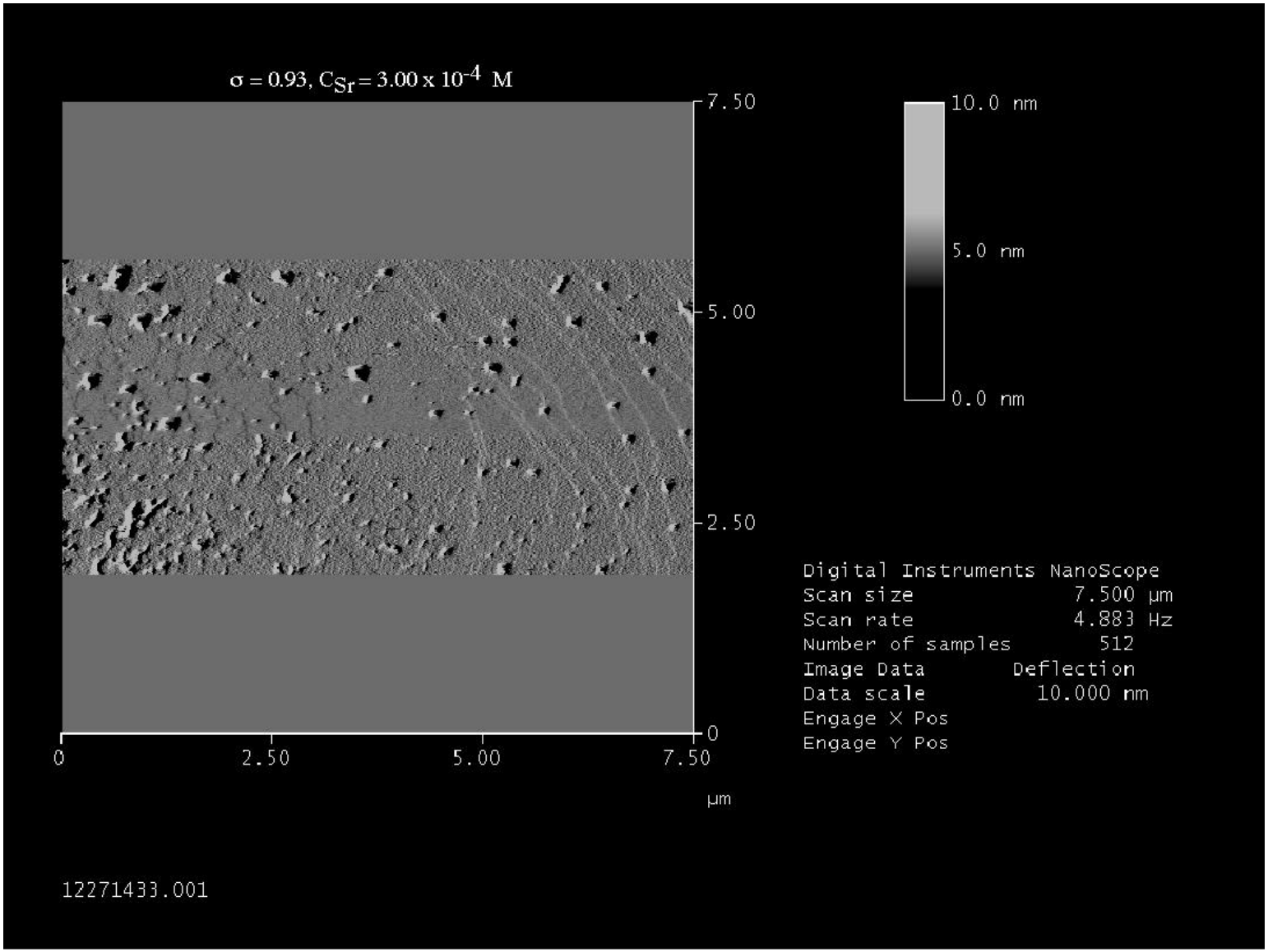
σ = 0.93, C_{Sr} = 3.00 x 10^{-4} M
7.50
5.00
2.50
0
0
2.50
5.00
7.50
µm
10.0 nm
5.0 nm
0.0 nm
Digital Instruments NanoScope
Scan size 7.500 µm
Scan rate 4.883 Hz
Number of samples 512
Image Data Deflection
Data scale 10.000 nm
Engage X Pos
Engage Y Pos
12271433.001

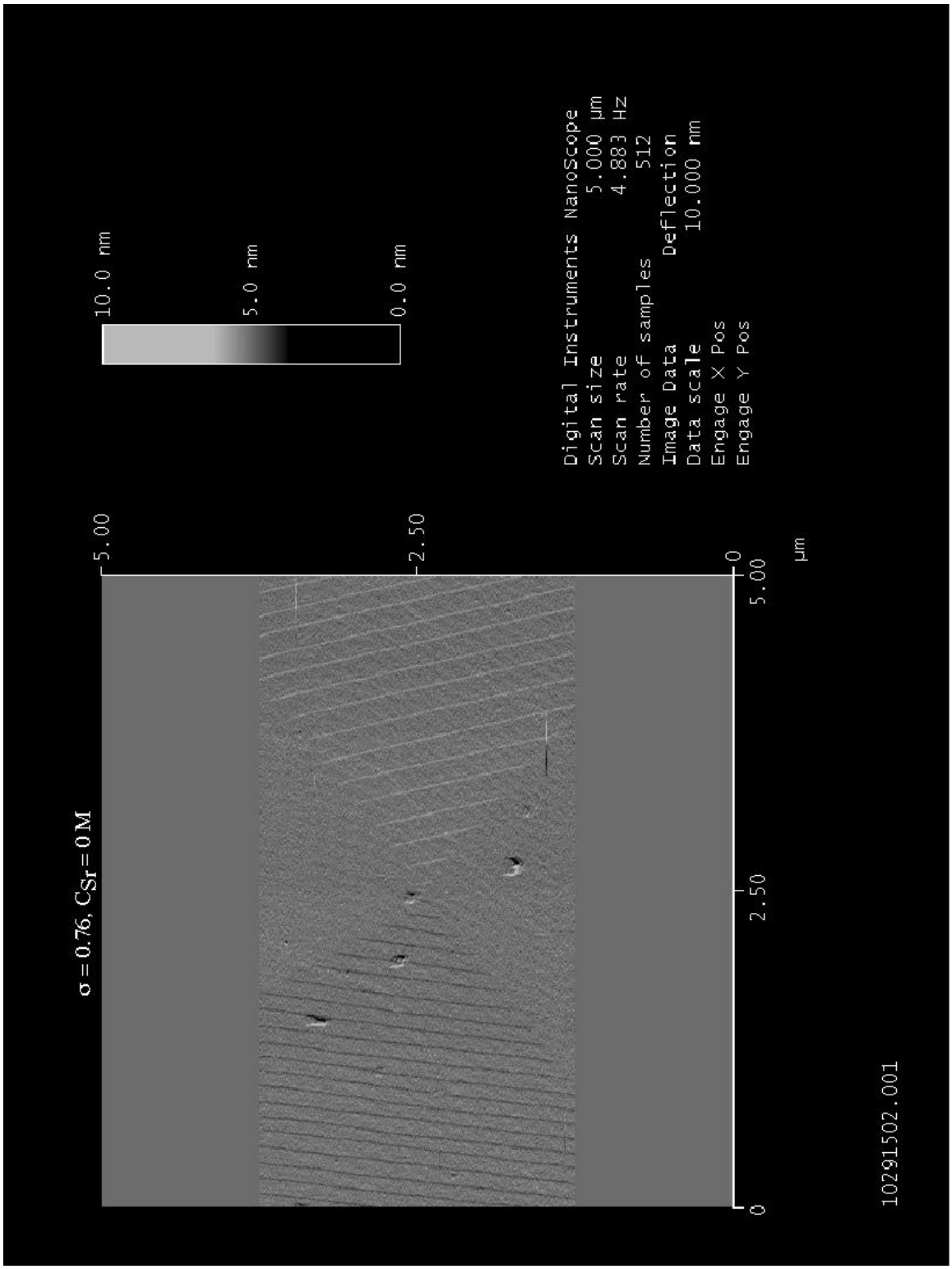
σ = 0.76, C_{Sr} = 0 M
10.0 nm
5.0 nm
0.0 nm
Digital Instruments NanoScope
Scan size 5.000 µm
Scan rate 4.883 Hz
Number of samples 512
Image Data Deflection
Data scale 10.000 nm
Engage X Pos
Engage Y Pos
5.00
2.50
0
2.50
5.00
µm
10291502.001

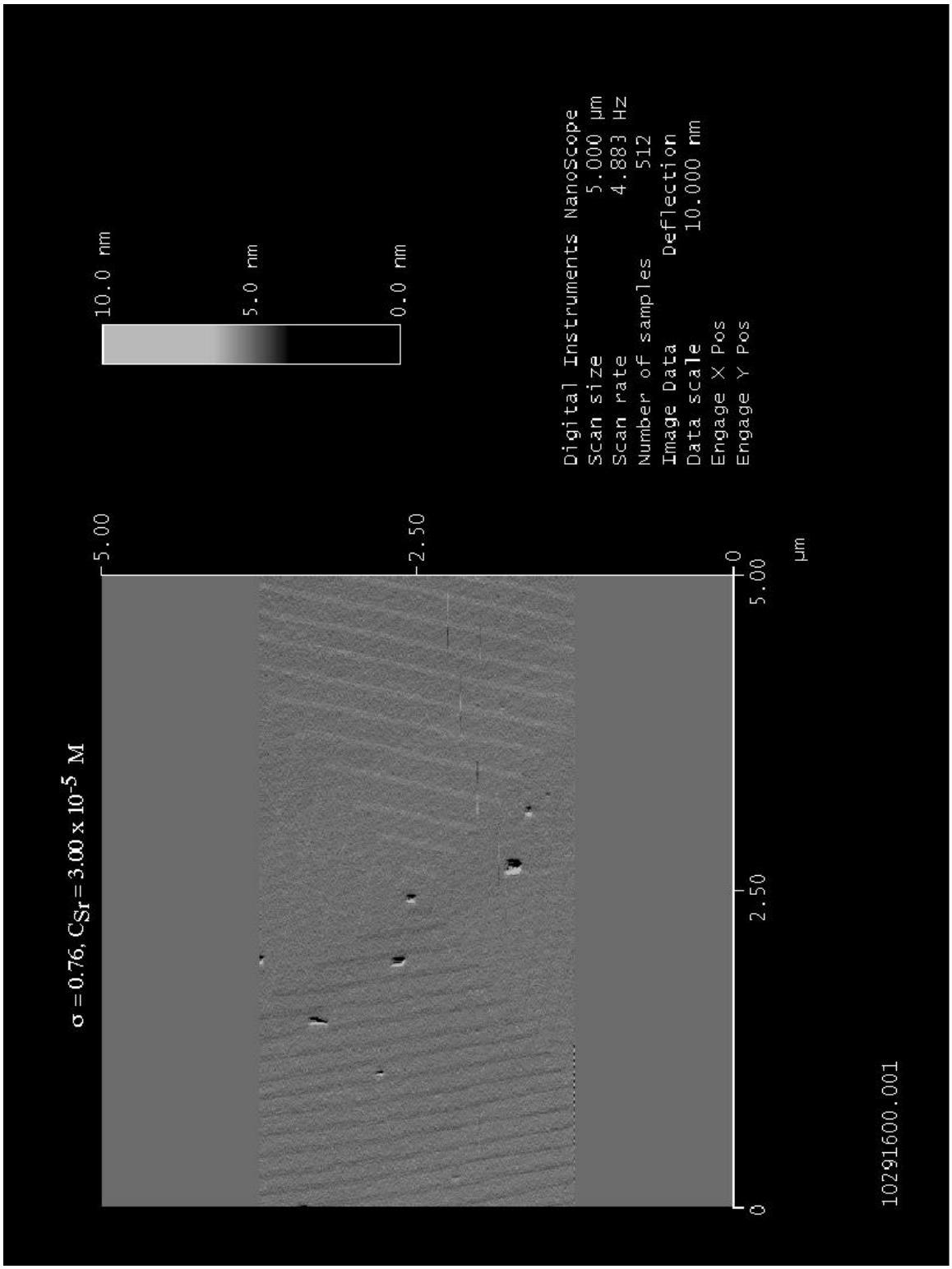
σ = 0.76, C_{Sr} = 3.00 x 10^{-5} M
10.0 nm
5.0 nm
0.0 nm
Digital Instruments NanoScope
Scan size 5.000 µm
Scan rate 4.883 Hz
Number of samples 512
Image Data Deflection
Data scale 10.000 nm
Engage X Pos
Engage Y Pos
5.00
2.50
0
2.50
5.00
µm
10291600.001

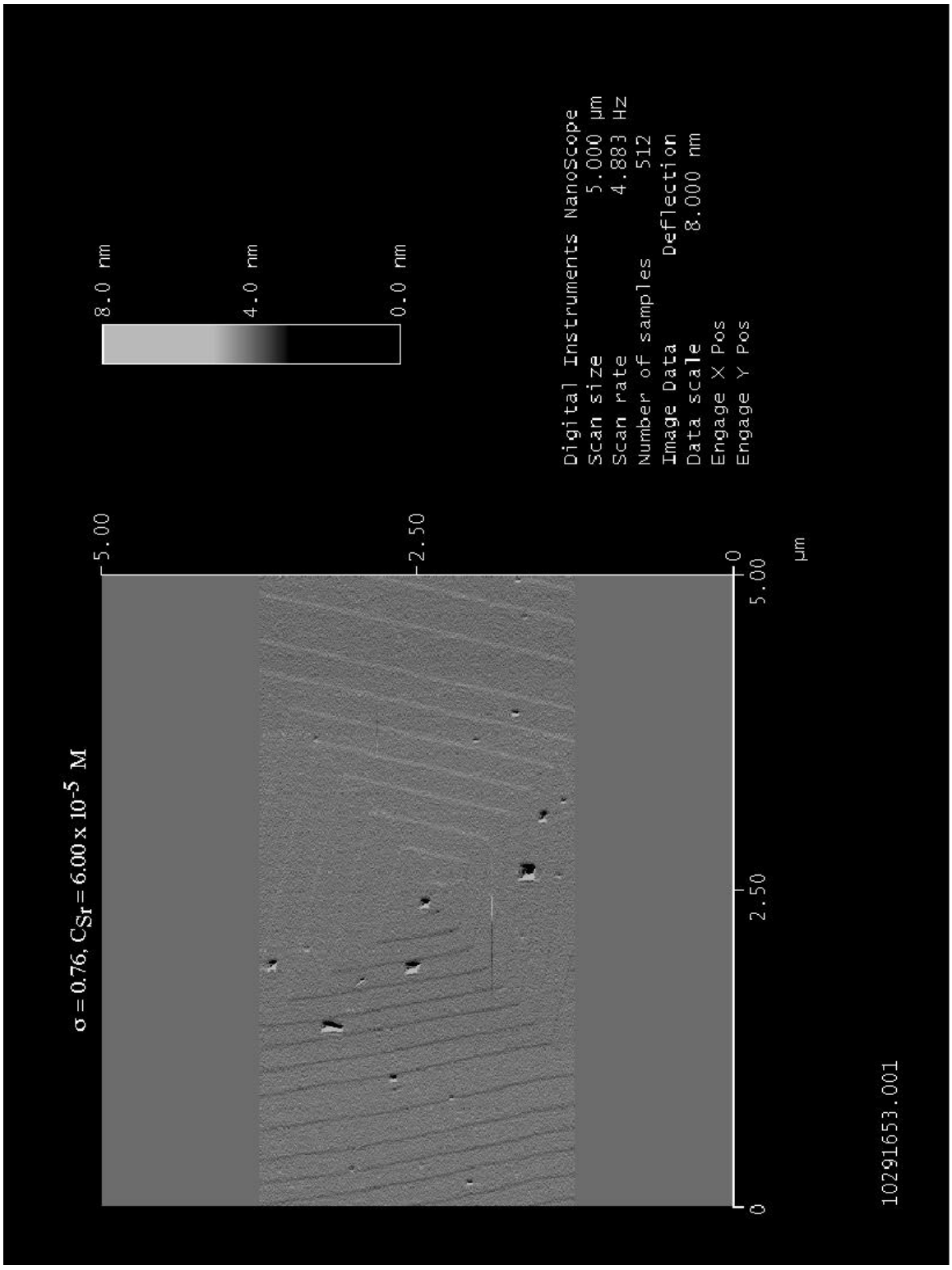
σ = 0.76, C_{Sr} = 6.00 x 10^{-5} M
8.0 nm
4.0 nm
0.0 nm
Digital Instruments NanoScope
Scan size 5.000 µm
Scan rate 4.883 Hz
Number of samples 512
Image Data Deflection
Data scale 8.000 nm
Engage X Pos
Engage Y Pos
5.00
2.50
0
2.50
5.00
µm
10291653.001

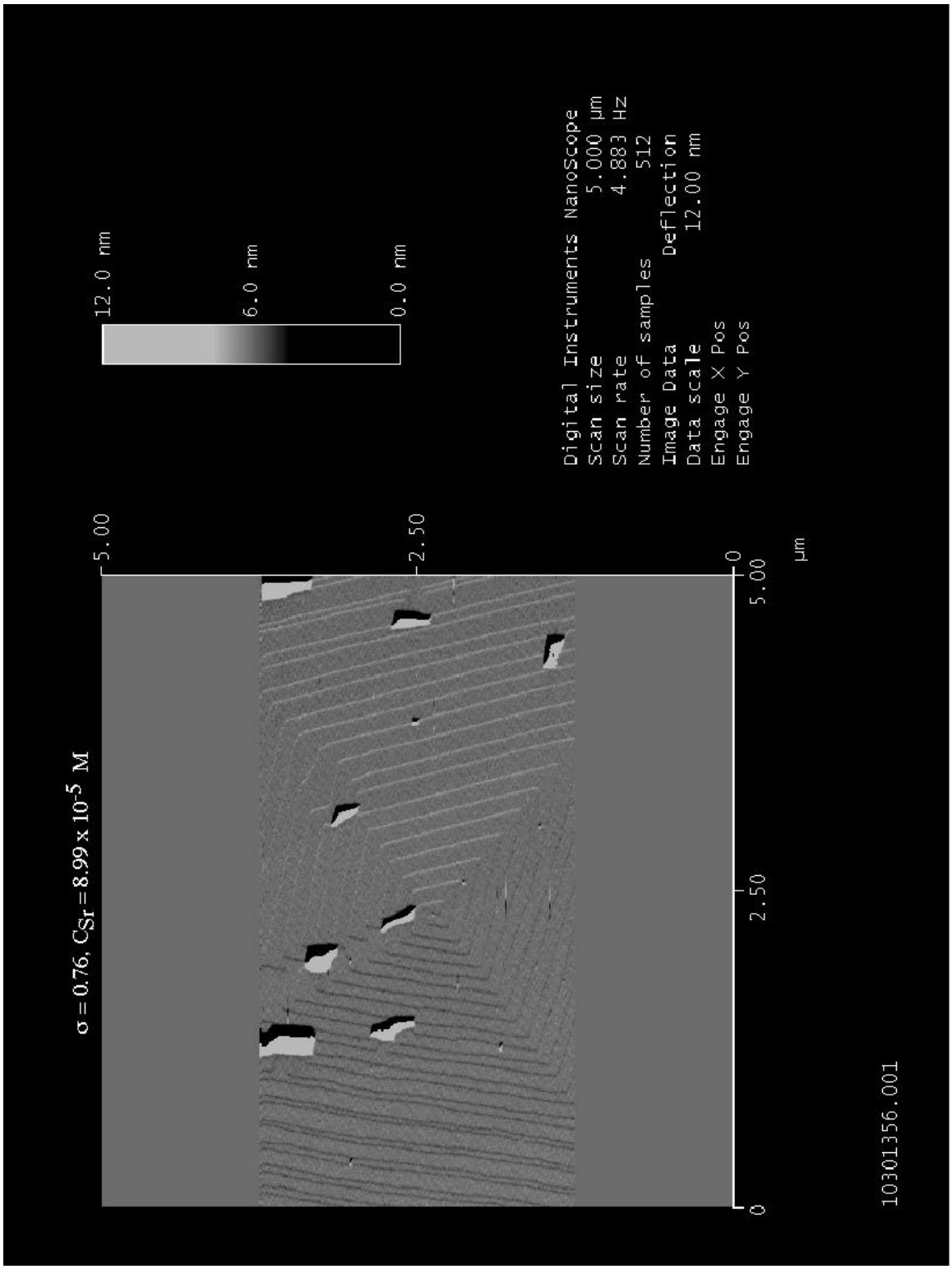
σ = 0.76, $C_{Sr} = 8.99 \times 10^{-5}$ M
12.0 nm
6.0 nm
0.0 nm
Digital Instruments NanoScope
Scan size 5.000 µm
Scan rate 4.883 Hz
Number of samples 512
Image Data Deflection
Data scale 12.00 nm
Engage X Pos
Engage Y Pos
5.00
2.50
0
0
2.50
5.00
µm
10301356.001

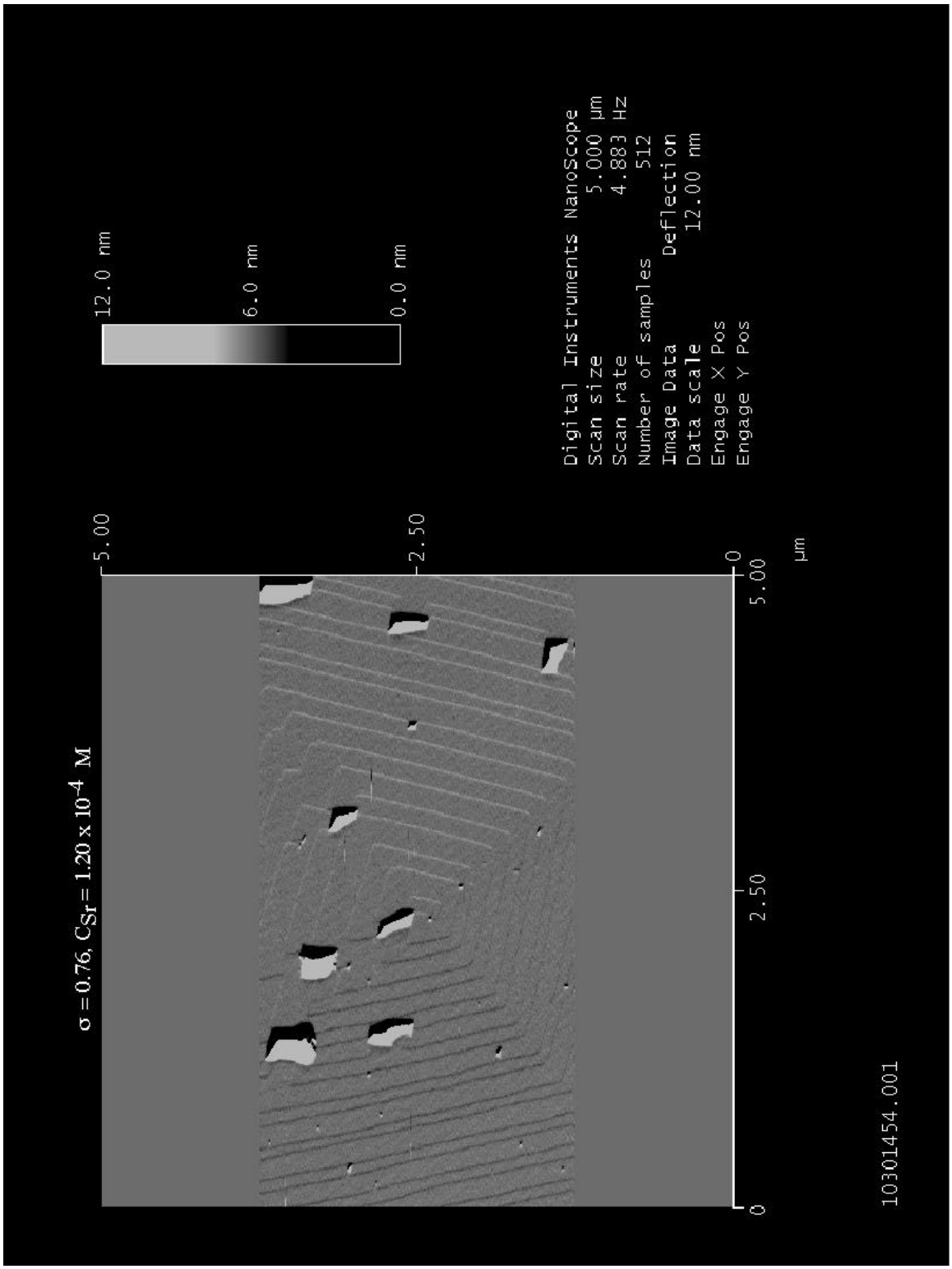
σ = 0.76, C_{Sr} = 1.20 x 10^{-4} M
12.0 nm
6.0 nm
0.0 nm
Digital Instruments NanoScope
Scan size 5.000 µm
Scan rate 4.883 Hz
Number of samples 512
Image Data Deflection
Data scale 12.00 nm
Engage X Pos
Engage Y Pos
5.00
2.50
0
2.50
5.00
µm
10301454.001

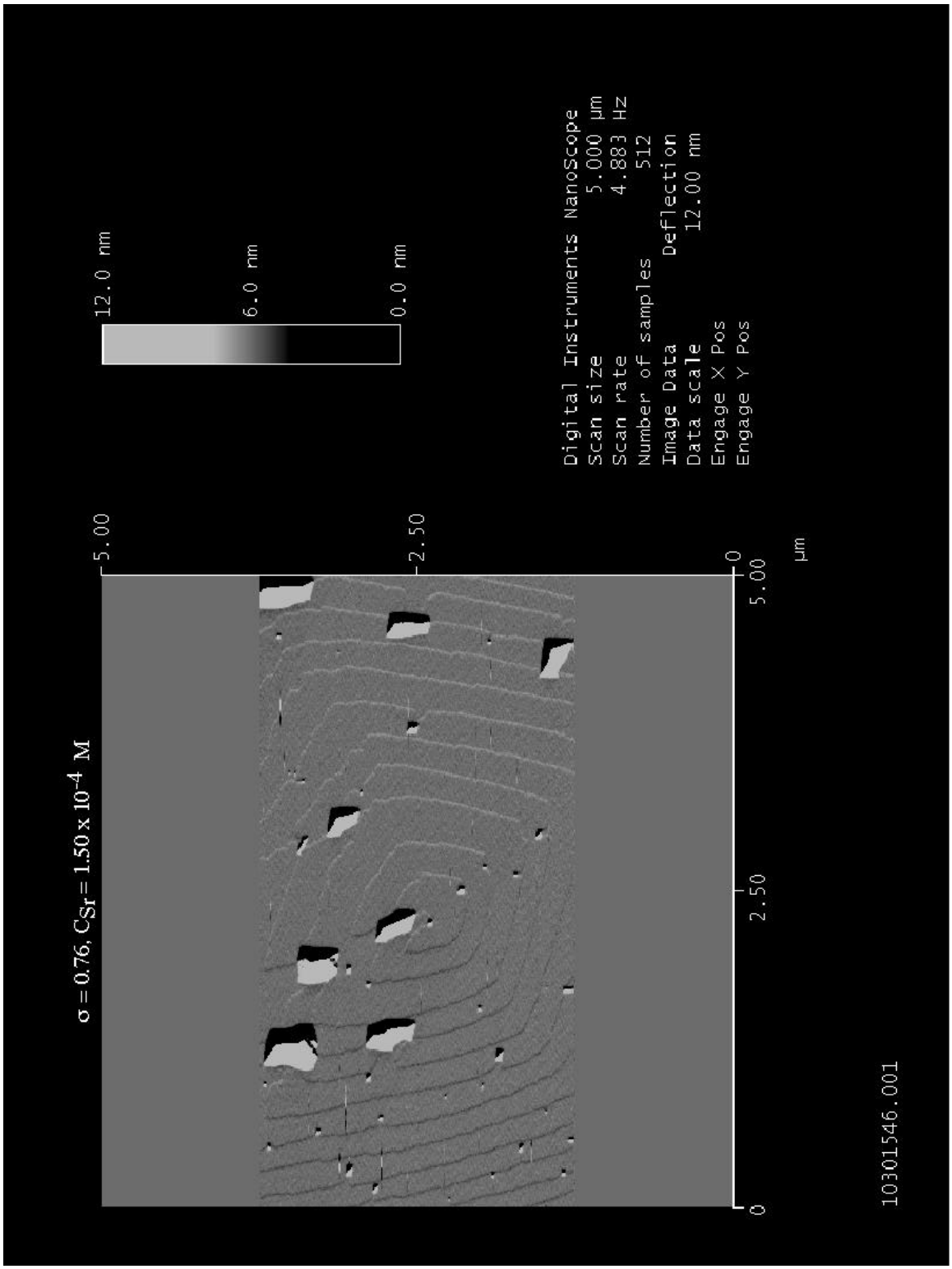
σ = 0.76, C_{Sr} = 1.50 x 10^{-4} M
12.0 nm
6.0 nm
0.0 nm
Digital Instruments NanoScope
Scan size 5.000 µm
Scan rate 4.883 Hz
Number of samples 512
Image Data Deflection
Data scale 12.00 nm
Engage X Pos
Engage Y Pos
5.00
2.50
0
2.50
5.00
µm
10301546.001

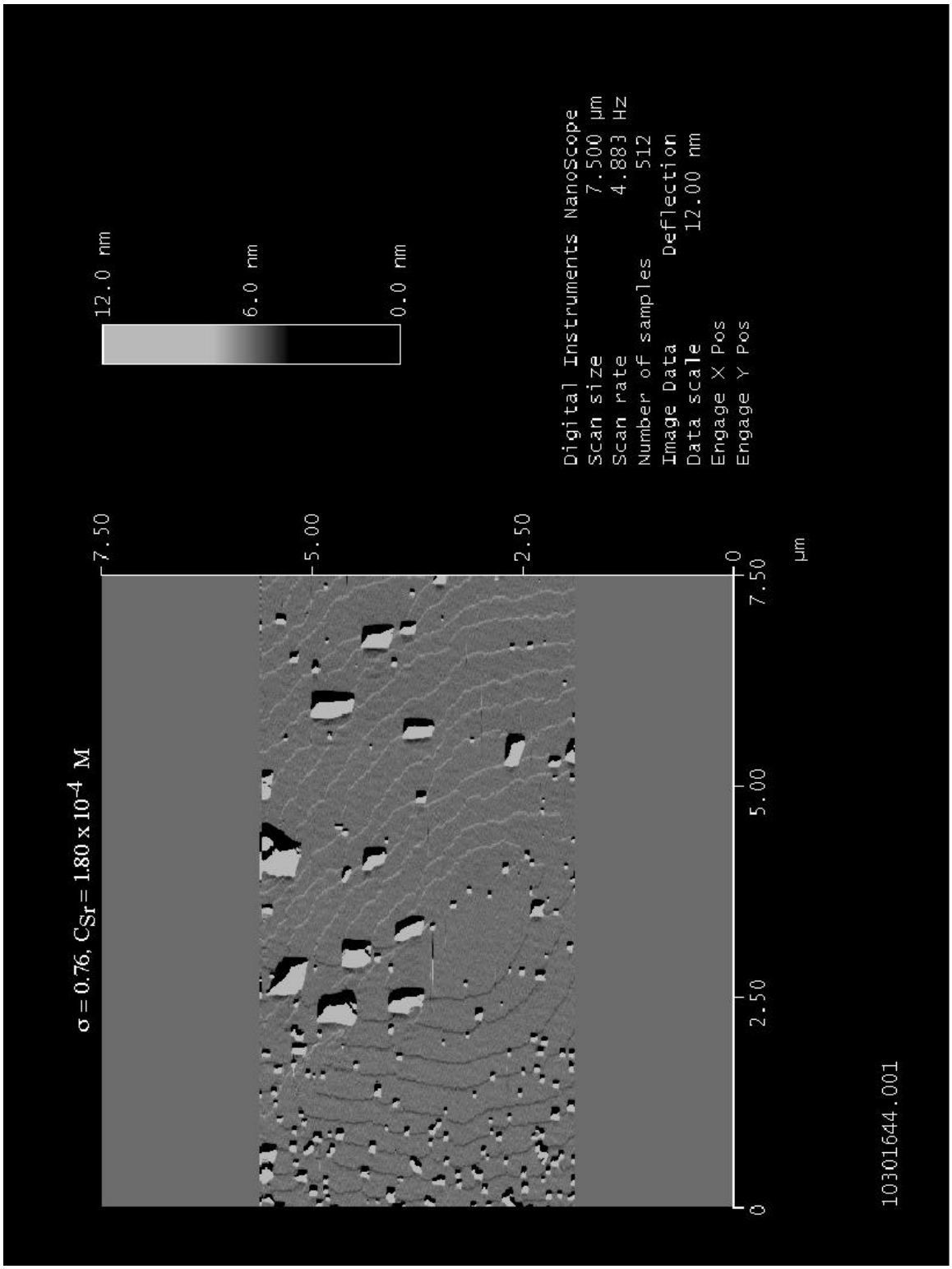
σ = 0.76, C_{Sr} = 1.80 x 10^{-4} M
12.0 nm
6.0 nm
0.0 nm
Digital Instruments NanoScope
Scan size 7.500 µm
Scan rate 4.883 Hz
Number of samples 512
Image Data Deflection
Data scale 12.00 nm
Engage X Pos
Engage Y Pos
7.50
5.00
2.50
0
µm
10301644.001

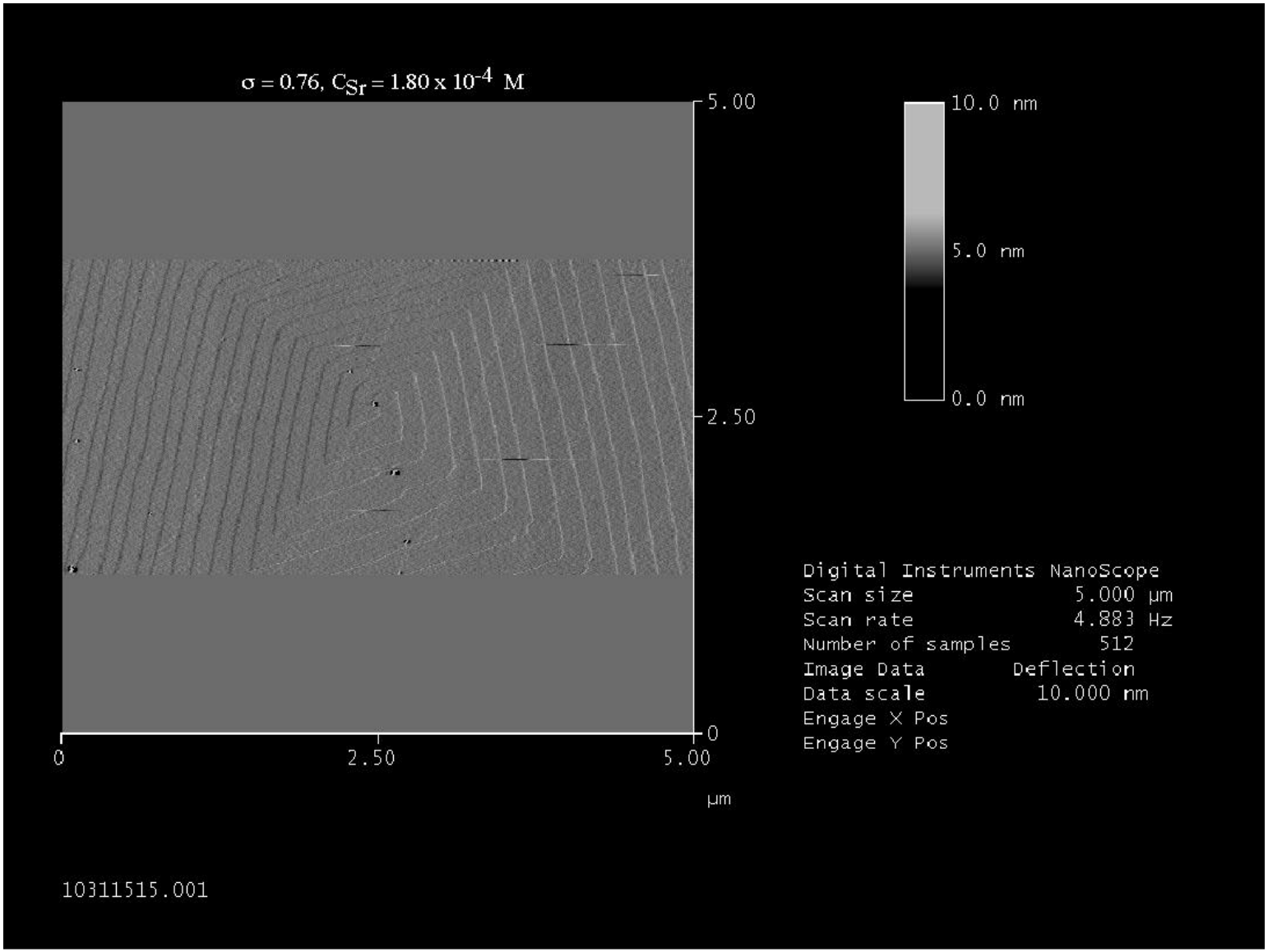
σ = 0.76, C_{Sr} = 1.80 x 10^{-4} M
5.00
2.50
0
0
2.50
5.00
µm
10.0 nm
5.0 nm
0.0 nm
Digital Instruments NanoScope
Scan size 5.000 µm
Scan rate 4.883 Hz
Number of samples 512
Image Data Deflection
Data scale 10.000 nm
Engage X Pos
Engage Y Pos
10311515.001

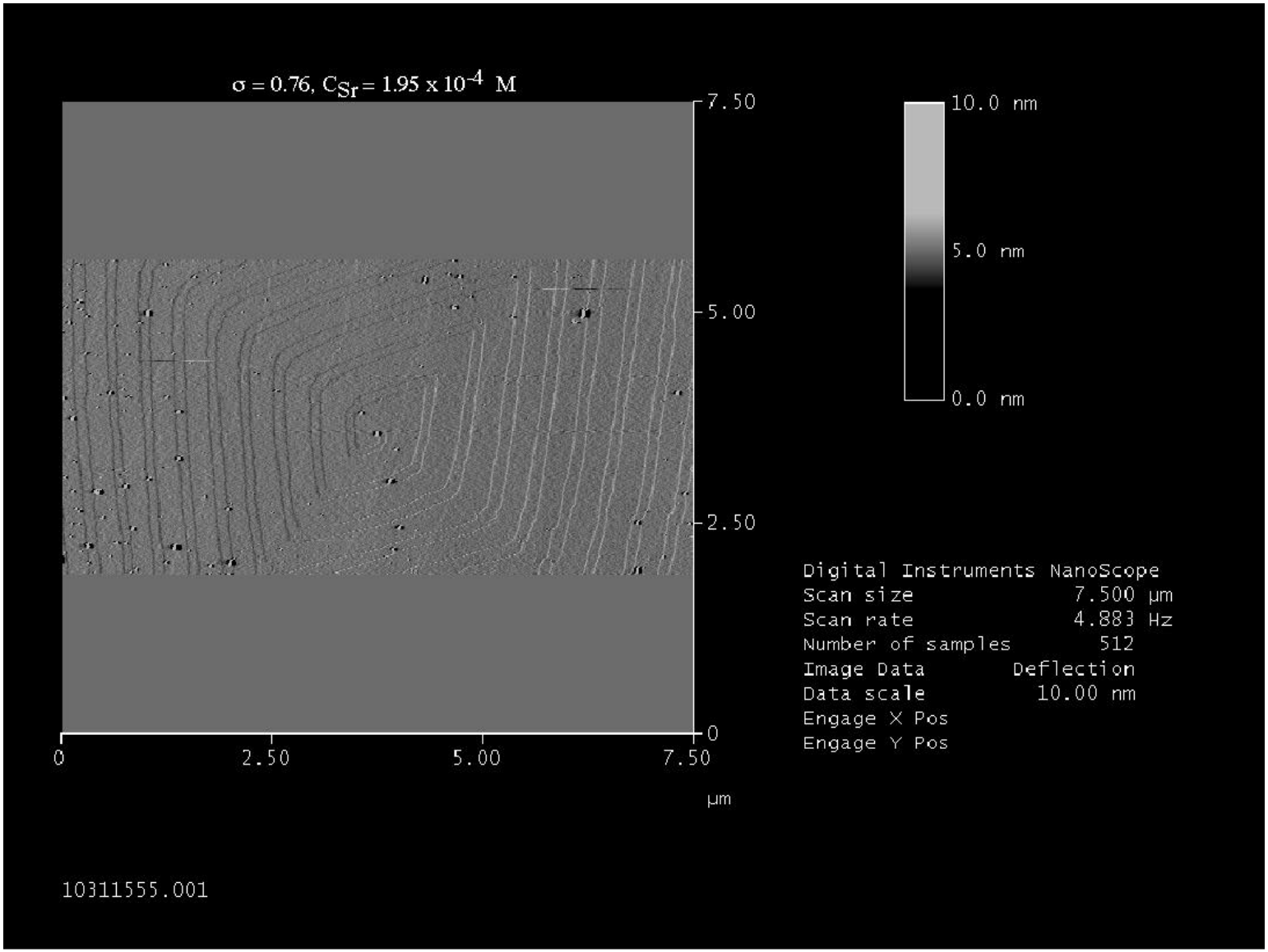
σ = 0.76, C_{Sr} = 1.95 x 10^{-4} M
7.50
5.00
2.50
0
0
2.50
5.00
7.50
µm
10.0 nm
5.0 nm
0.0 nm
Digital Instruments NanoScope
Scan size 7.500 µm
Scan rate 4.883 Hz
Number of samples 512
Image Data Deflection
Data scale 10.00 nm
Engage X Pos
Engage Y Pos
10311555.001

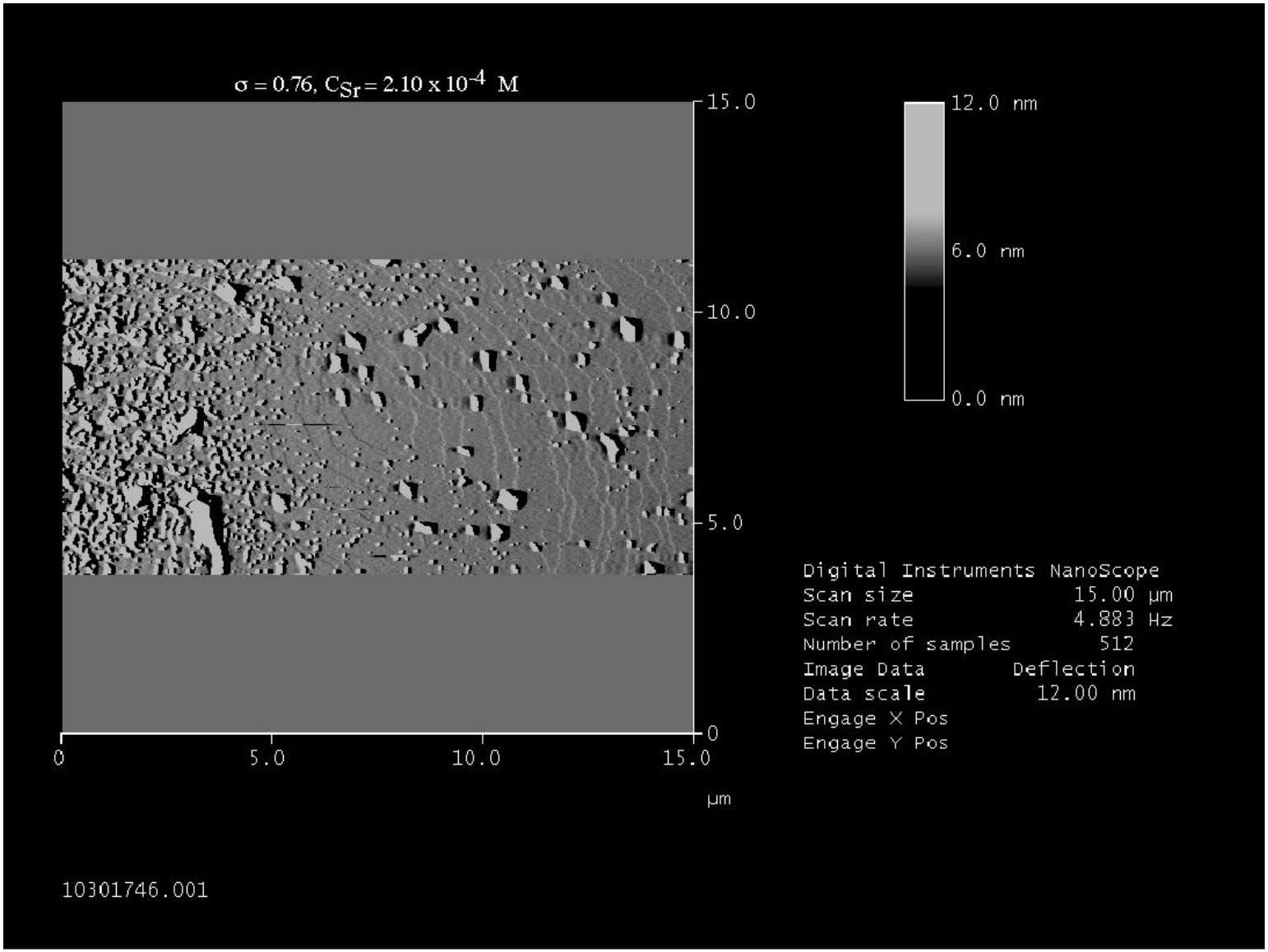
σ = 0.76, C_{Sr} = 2.10 x 10^{-4} M
15.0
10.0
5.0
0
0
5.0
10.0
15.0
µm
12.0 nm
6.0 nm
0.0 nm
Digital Instruments NanoScope
Scan size 15.00 µm
Scan rate 4.883 Hz
Number of samples 512
Image Data Deflection
Data scale 12.00 nm
Engage X Pos
Engage Y Pos
10301746.001

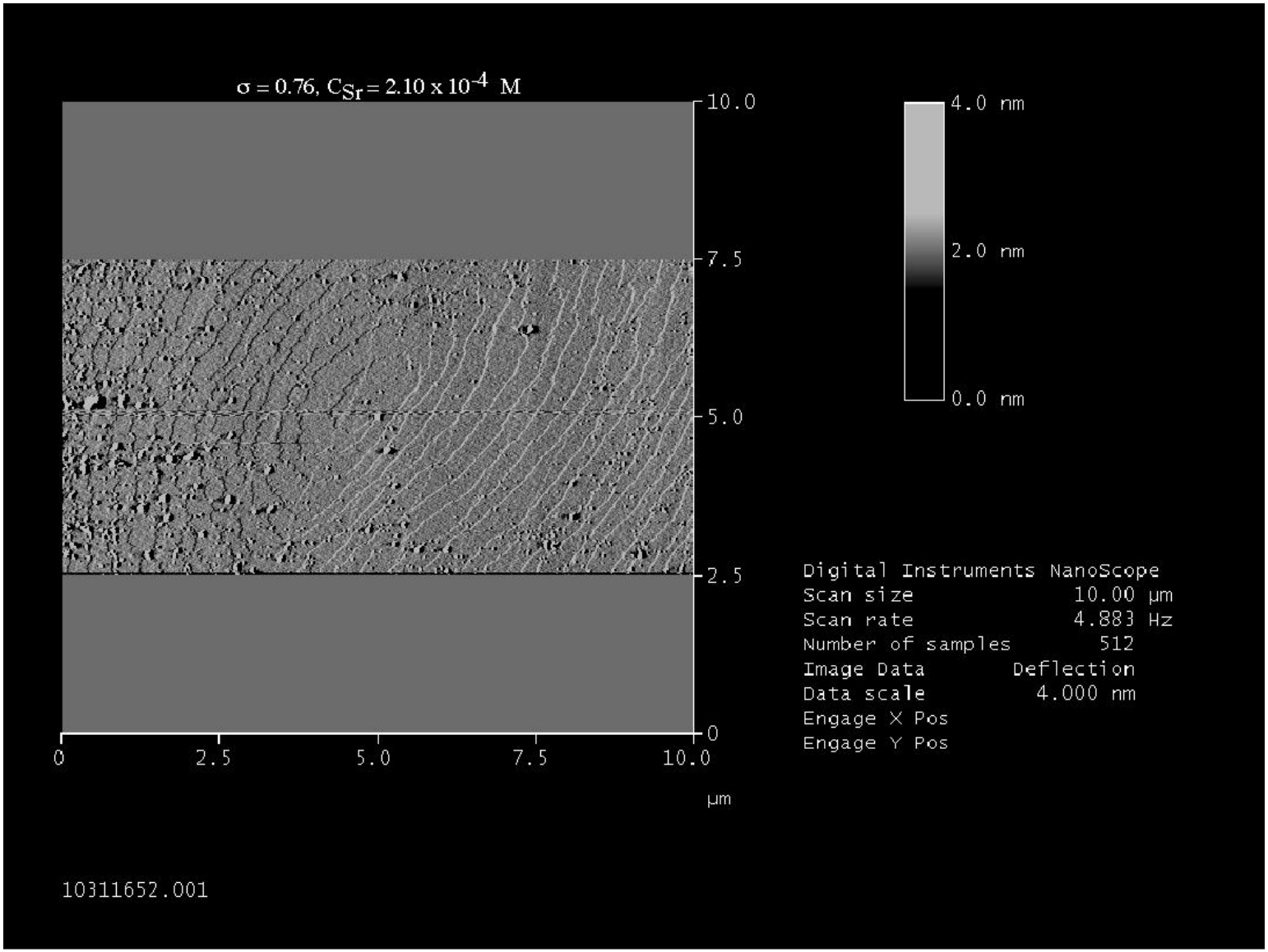
σ = 0.76, C_{Sr} = 2.10 x 10^{-4} M
10.0
7.5
5.0
2.5
0
0
2.5
5.0
7.5
10.0
µm
4.0 nm
2.0 nm
0.0 nm
Digital Instruments NanoScope
Scan size 10.00 µm
Scan rate 4.883 Hz
Number of samples 512
Image Data Deflection
Data scale 4.000 nm
Engage X Pos
Engage Y Pos
10311652.001

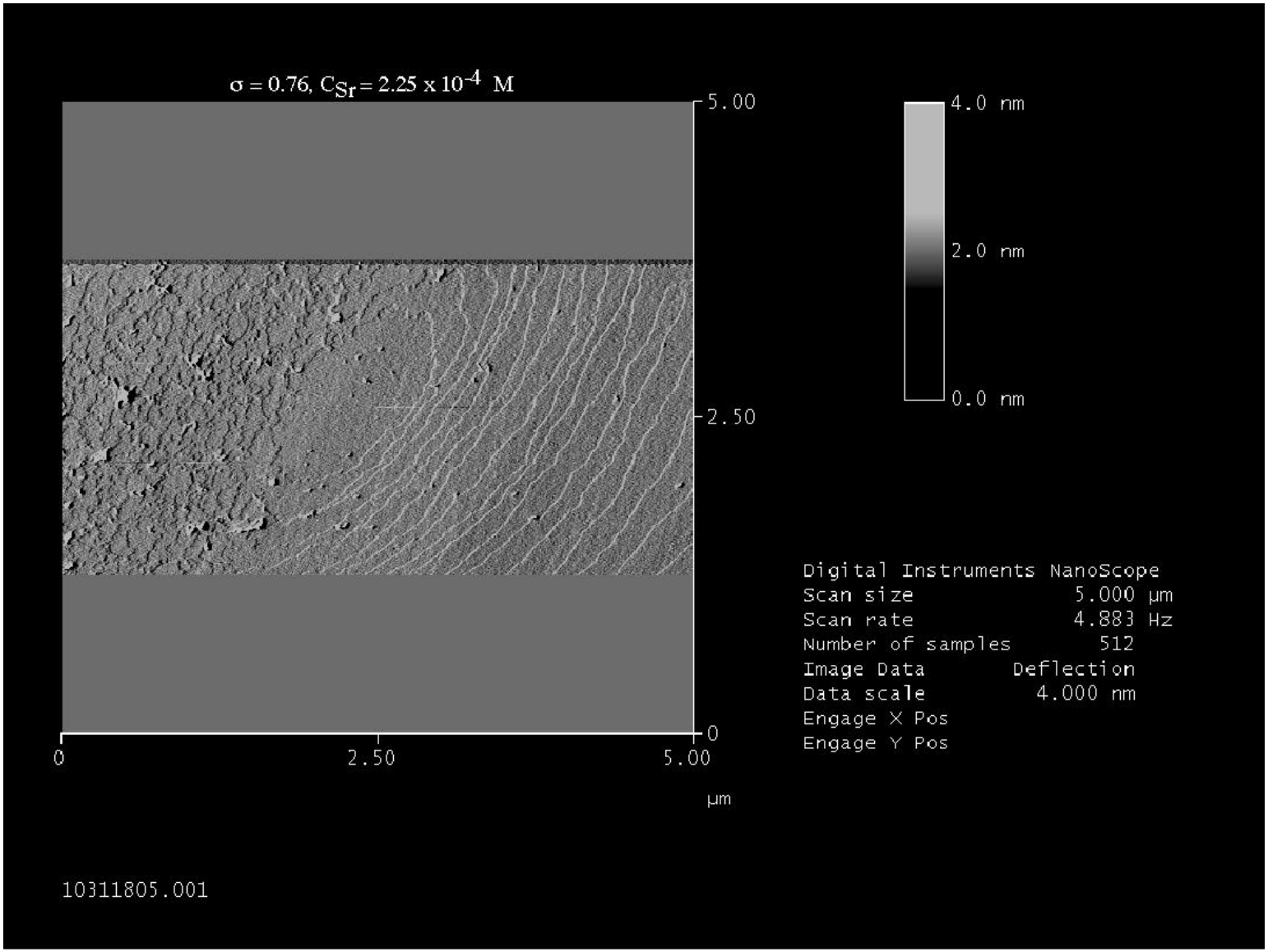
σ = 0.76, C_{Sr} = 2.25 x 10^{-4} M
5.00
2.50
0
0
2.50
5.00
µm
4.0 nm
2.0 nm
0.0 nm
Digital Instruments NanoScope
Scan size 5.000 µm
Scan rate 4.883 Hz
Number of samples 512
Image Data Deflection
Data scale 4.000 nm
Engage X Pos
Engage Y Pos
10311805.001

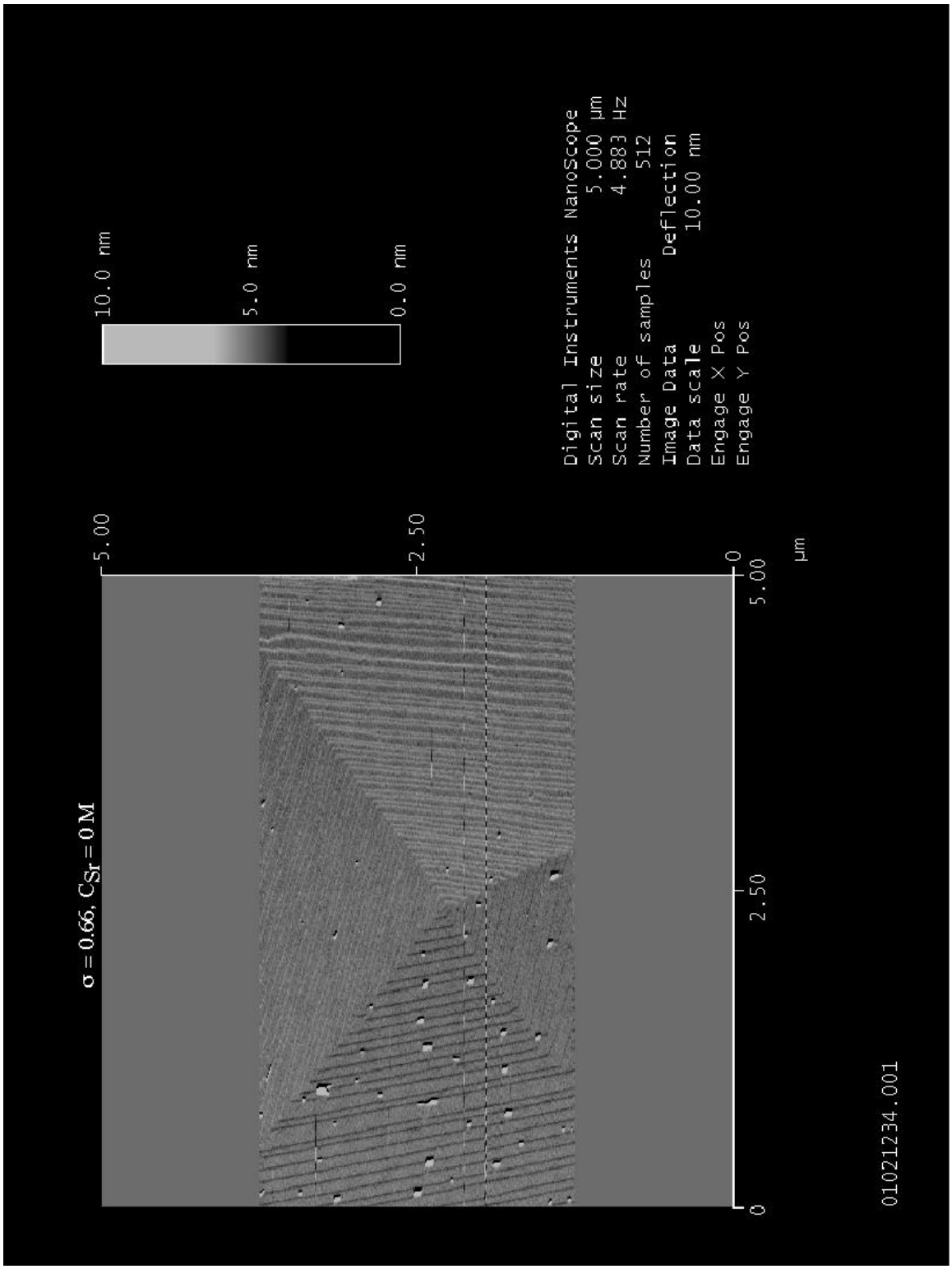
σ = 0.66, C_{Sr} = 0 M
10.0 nm
5.0 nm
0.0 nm
Digital Instruments NanoScope
Scan size 5.000 µm
Scan rate 4.883 Hz
Number of samples 512
Image Data Deflection
Data scale 10.00 nm
Engage X Pos
Engage Y Pos
5.00
2.50
0
2.50
5.00
µm
01021234.001

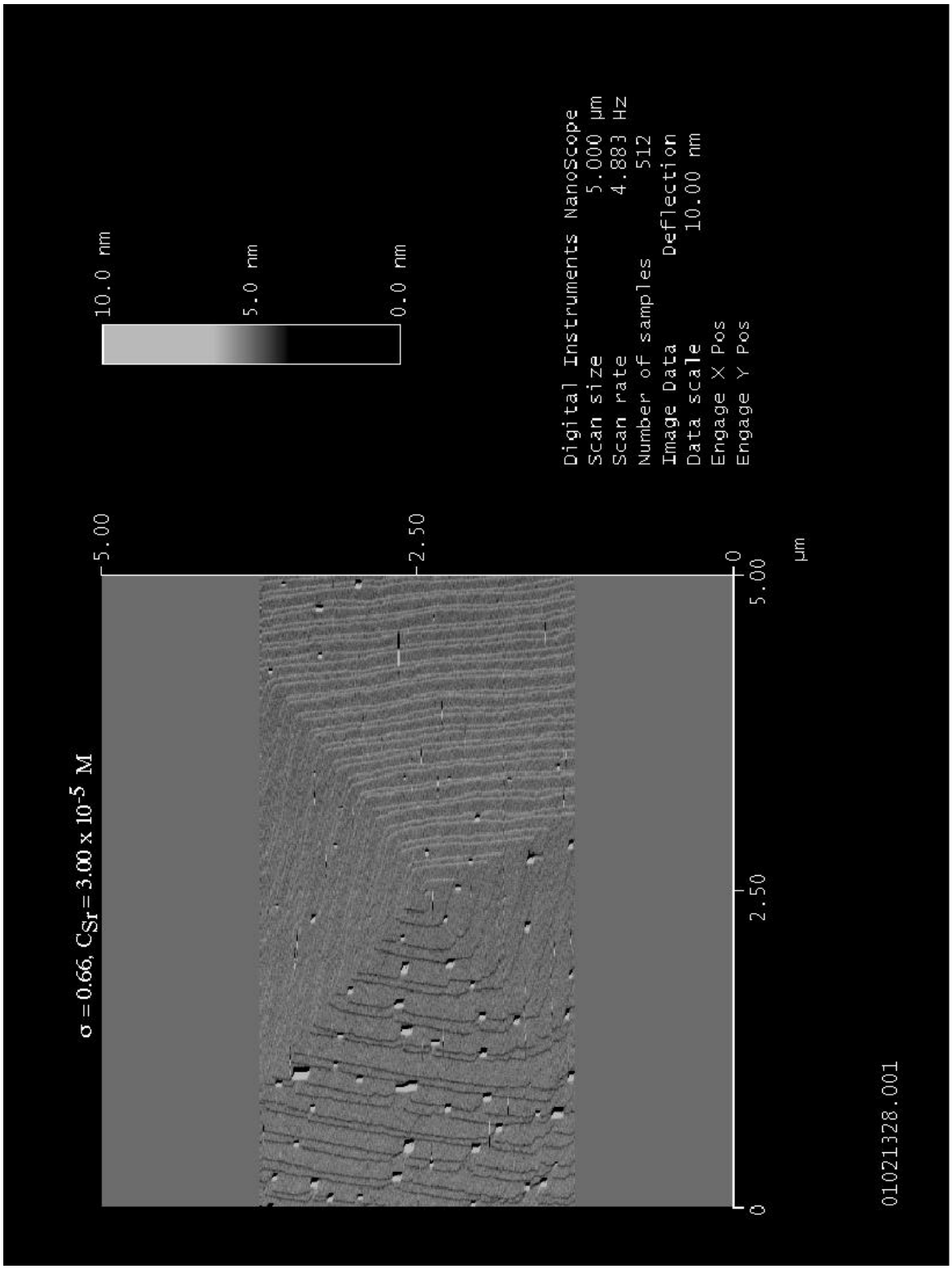
σ = 0.66, C_{Sr} = 3.00 x 10^{-5} M
10.0 nm
5.0 nm
0.0 nm
Digital Instruments NanoScope
Scan size 5.000 µm
Scan rate 4.883 Hz
Number of samples 512
Image Data Deflection
Data scale 10.00 nm
Engage X Pos
Engage Y Pos
5.00
2.50
0
2.50
5.00
µm
01021328.001

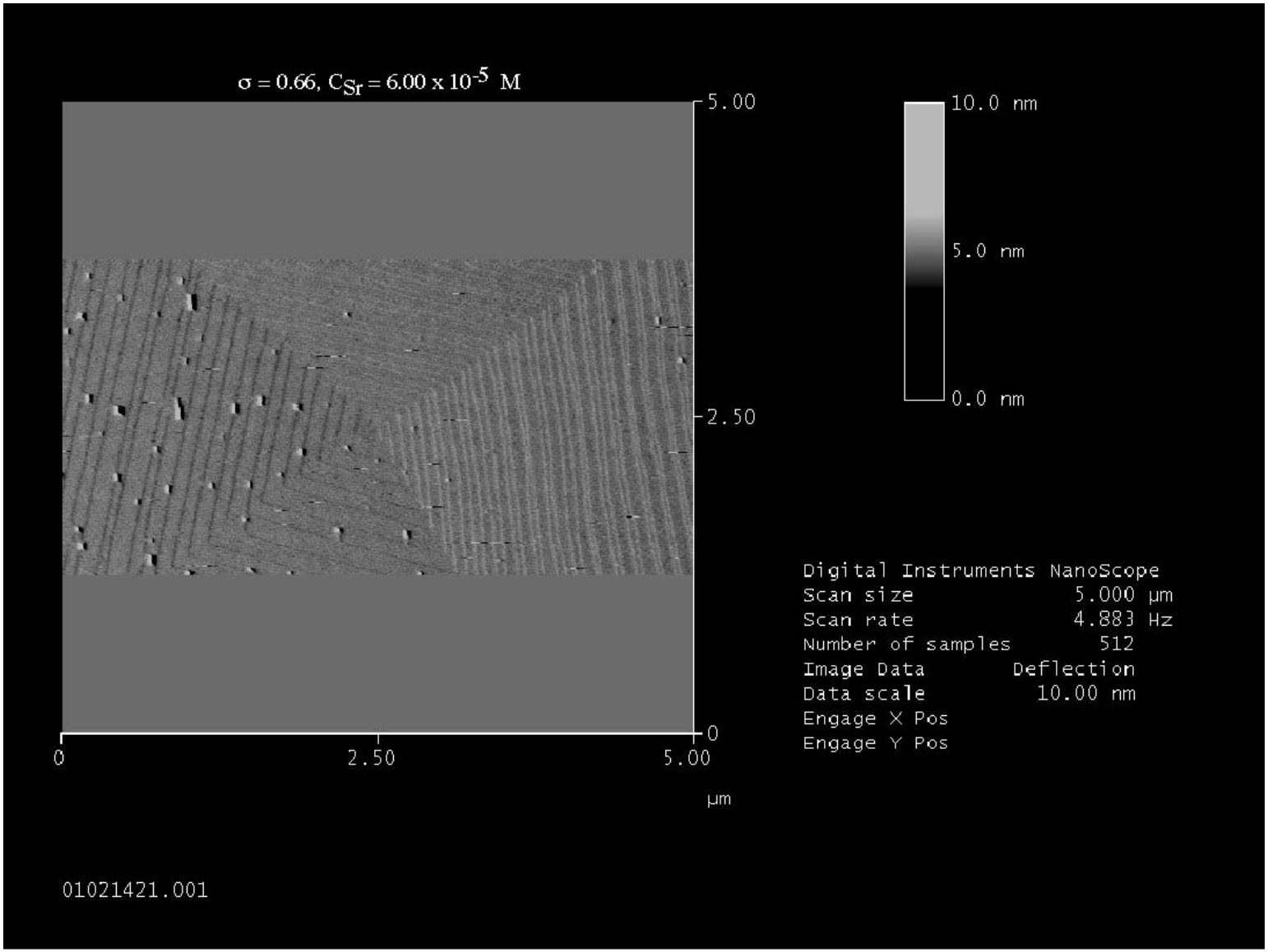
σ = 0.66, C_{Sr} = 6.00 x 10^{-5} M
5.00
2.50
0
0
2.50
5.00
µm
10.0 nm
5.0 nm
0.0 nm
Digital Instruments NanoScope
Scan size 5.000 µm
Scan rate 4.883 Hz
Number of samples 512
Image Data Deflection
Data scale 10.00 nm
Engage X Pos
Engage Y Pos
01021421.001

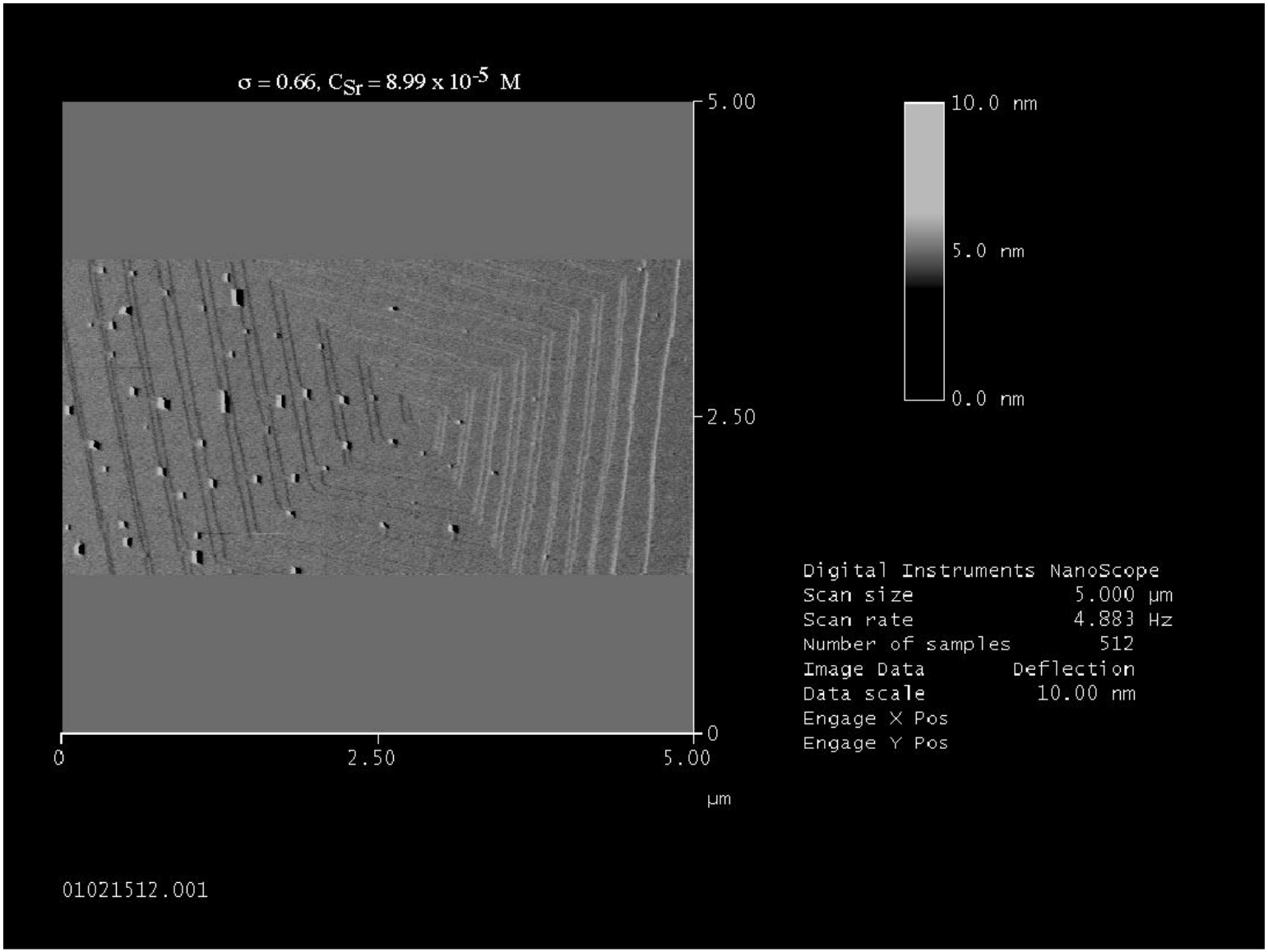
σ = 0.66, C_{Sr} = 8.99 x 10^{-5} M
5.00
2.50
0
0
2.50
5.00
µm
10.0 nm
5.0 nm
0.0 nm
Digital Instruments NanoScope
Scan size 5.000 µm
Scan rate 4.883 Hz
Number of samples 512
Image Data Deflection
Data scale 10.00 nm
Engage X Pos
Engage Y Pos
01021512.001

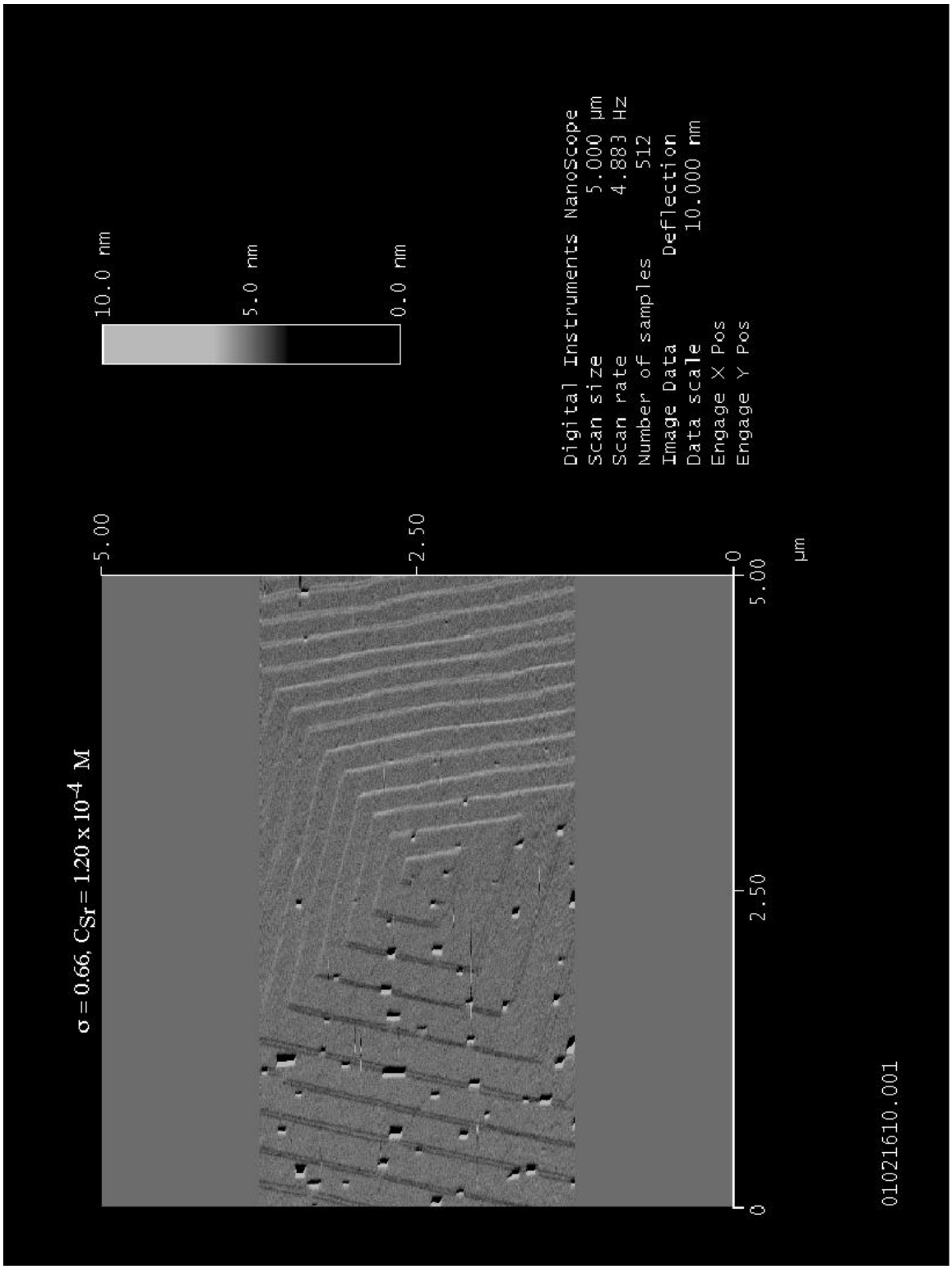
σ = 0.66, C_{Sr} = 1.20 x 10^{-4} M
10.0 nm
5.0 nm
0.0 nm
Digital Instruments NanoScope
Scan size 5.000 µm
Scan rate 4.883 Hz
Number of samples 512
Image Data Deflection
Data scale 10.000 nm
Engage X Pos
Engage Y Pos
5.00
2.50
0
2.50
5.00
µm
01021610.001

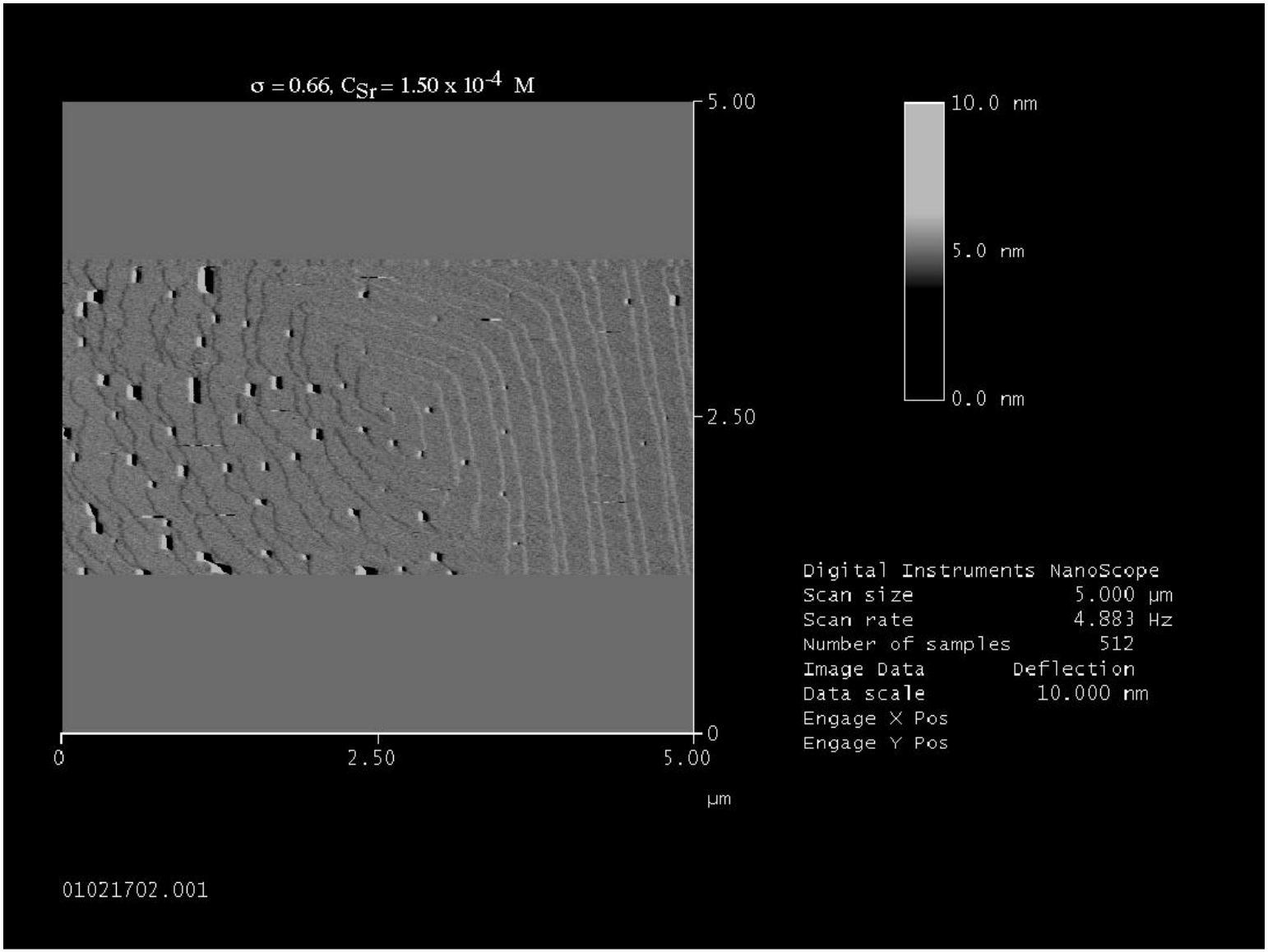
σ = 0.66, C_{Sr} = 1.50 x 10^{-4} M
5.00
2.50
0
0
2.50
5.00
µm
10.0 nm
5.0 nm
0.0 nm
Digital Instruments NanoScope
Scan size 5.000 µm
Scan rate 4.883 Hz
Number of samples 512
Image Data Deflection
Data scale 10.000 nm
Engage X Pos
Engage Y Pos
01021702.001

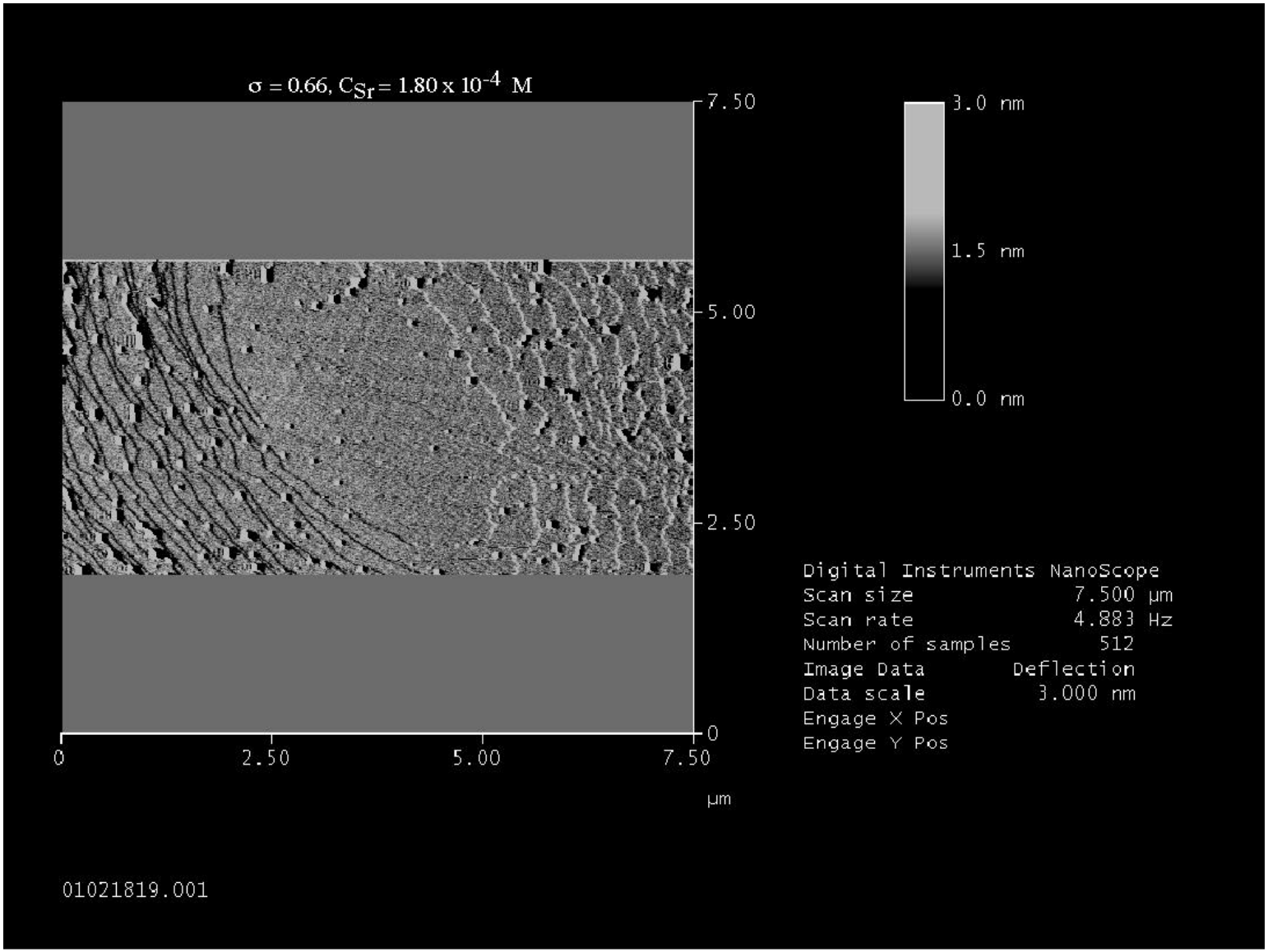
σ = 0.66, C_{Sr} = 1.80 x 10^{-4} M
7.50
5.00
2.50
0
0
2.50
5.00
7.50
µm
3.0 nm
1.5 nm
0.0 nm
Digital Instruments NanoScope
Scan size 7.500 µm
Scan rate 4.883 Hz
Number of samples 512
Image Data Deflection
Data scale 3.000 nm
Engage X Pos
Engage Y Pos
01021819.001

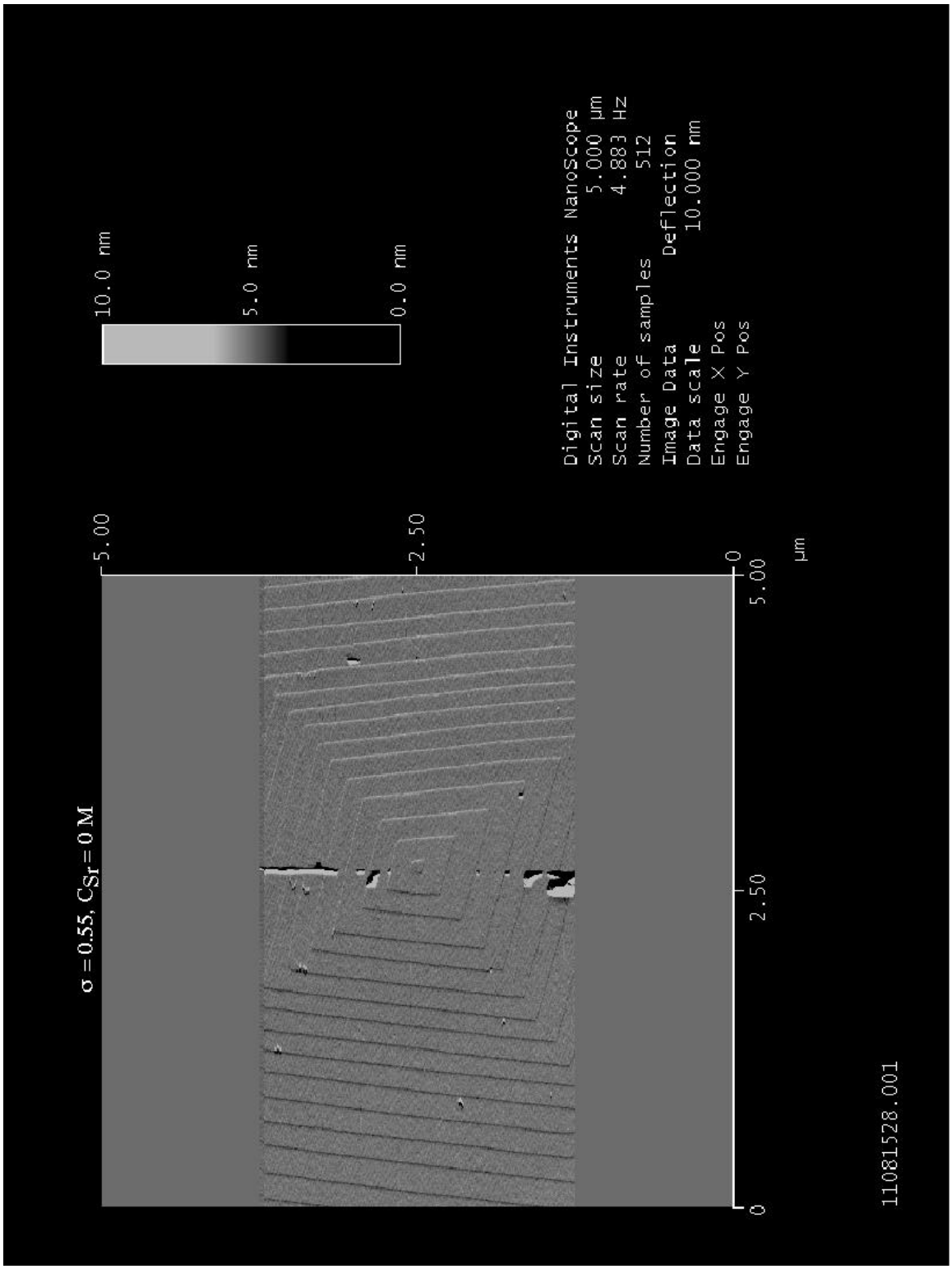
σ = 0.55, C_{Sr} = 0 M
10.0 nm
5.0 nm
0.0 nm
Digital Instruments NanoScope
Scan size 5.000 µm
Scan rate 4.883 Hz
Number of samples 512
Image Data Deflection
Data scale 10.000 nm
Engage X Pos
Engage Y Pos
5.00
2.50
0
0
2.50
5.00
µm
11081528.001

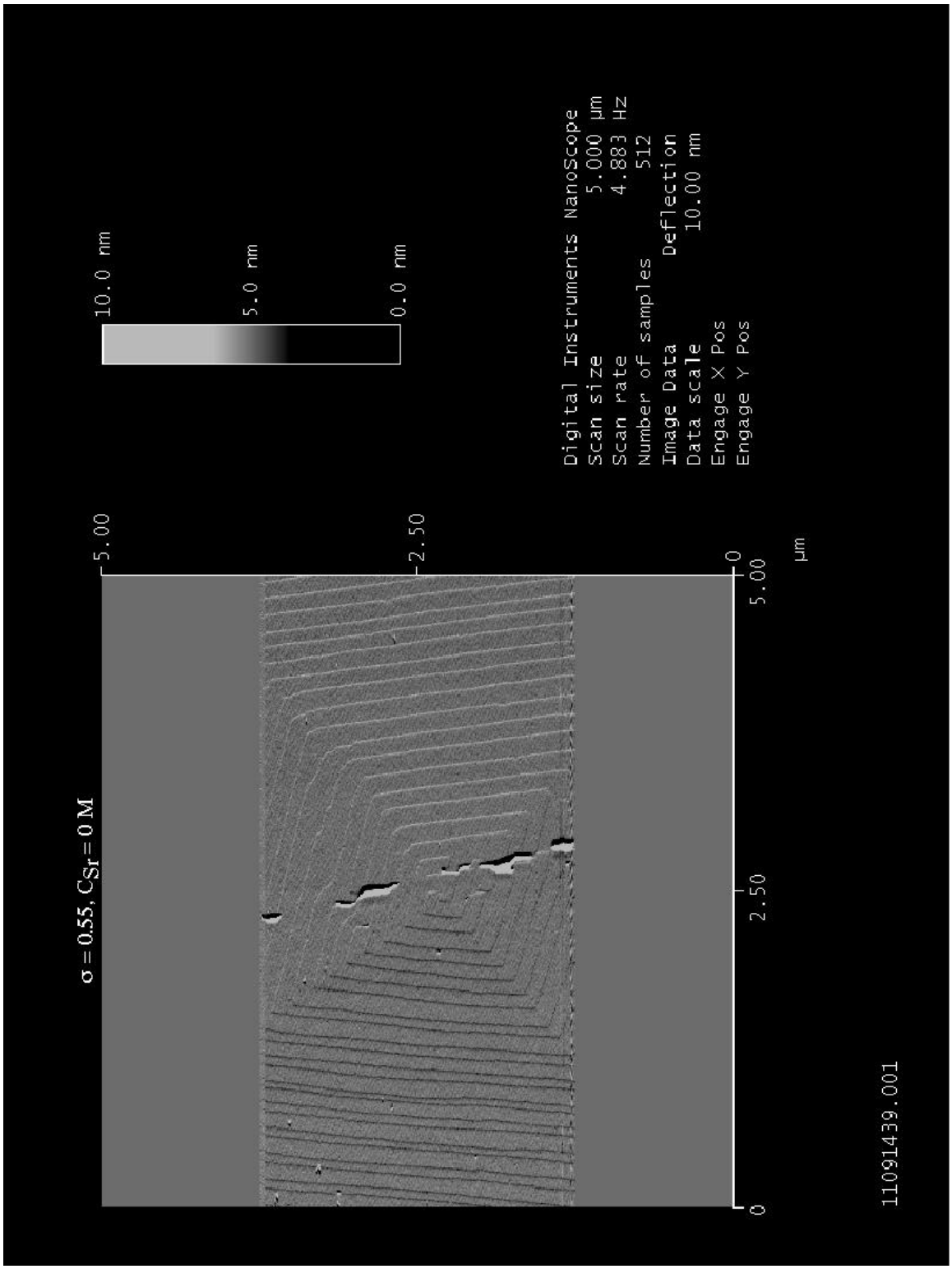
σ = 0.55, CSr = 0 M
10.0 nm
5.0 nm
0.0 nm
Digital Instruments NanoScope
Scan size 5.000 µm
Scan rate 4.883 Hz
Number of samples 512
Image Data Deflection
Data scale 10.00 nm
Engage X Pos
Engage Y Pos
5.00
2.50
0
0
2.50
5.00
µm
11091439.001

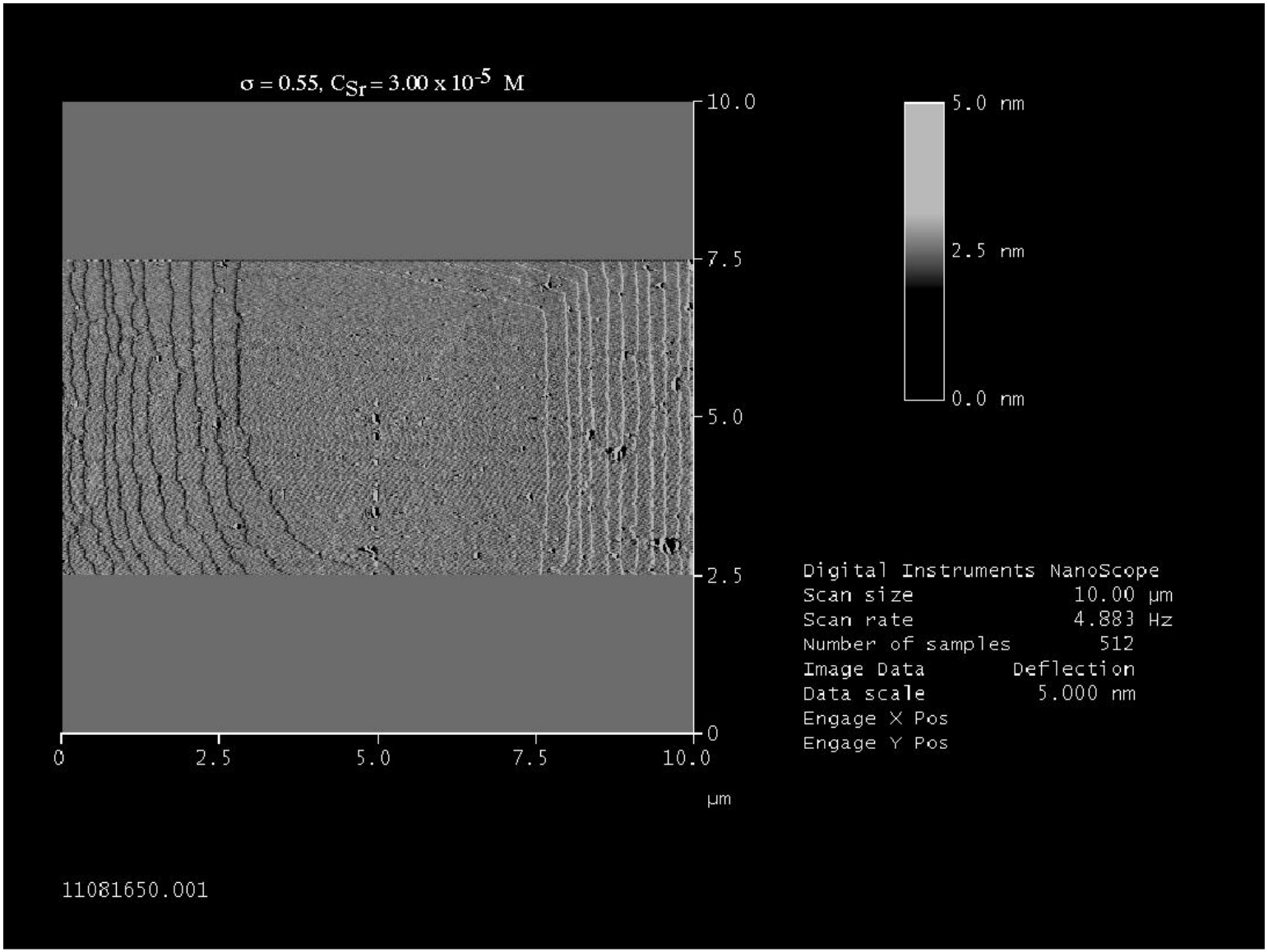
σ = 0.55, C_{Sr} = 3.00 x 10^{-5} M
10.0
7.5
5.0
2.5
0
0
2.5
5.0
7.5
10.0
µm
5.0 nm
2.5 nm
0.0 nm
Digital Instruments NanoScope
Scan size 10.00 µm
Scan rate 4.883 Hz
Number of samples 512
Image Data Deflection
Data scale 5.000 nm
Engage X Pos
Engage Y Pos
11081650.001

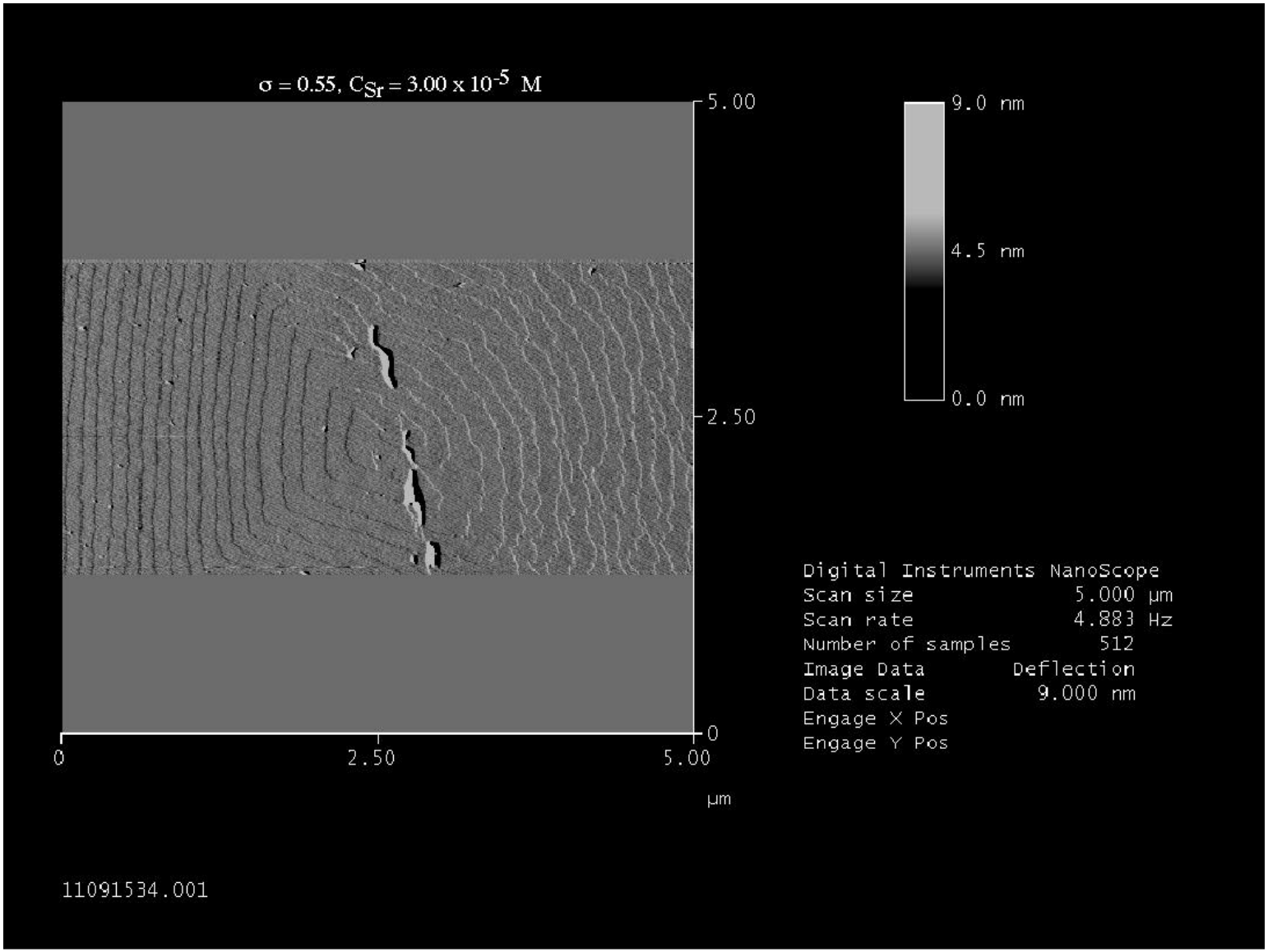
σ = 0.55, C_{Sr} = 3.00 x 10^{-5} M
5.00
2.50
0
0
2.50
5.00
µm
9.0 nm
4.5 nm
0.0 nm
Digital Instruments NanoScope
Scan size 5.000 µm
Scan rate 4.883 Hz
Number of samples 512
Image Data Deflection
Data scale 9.000 nm
Engage X Pos
Engage Y Pos
11091534.001

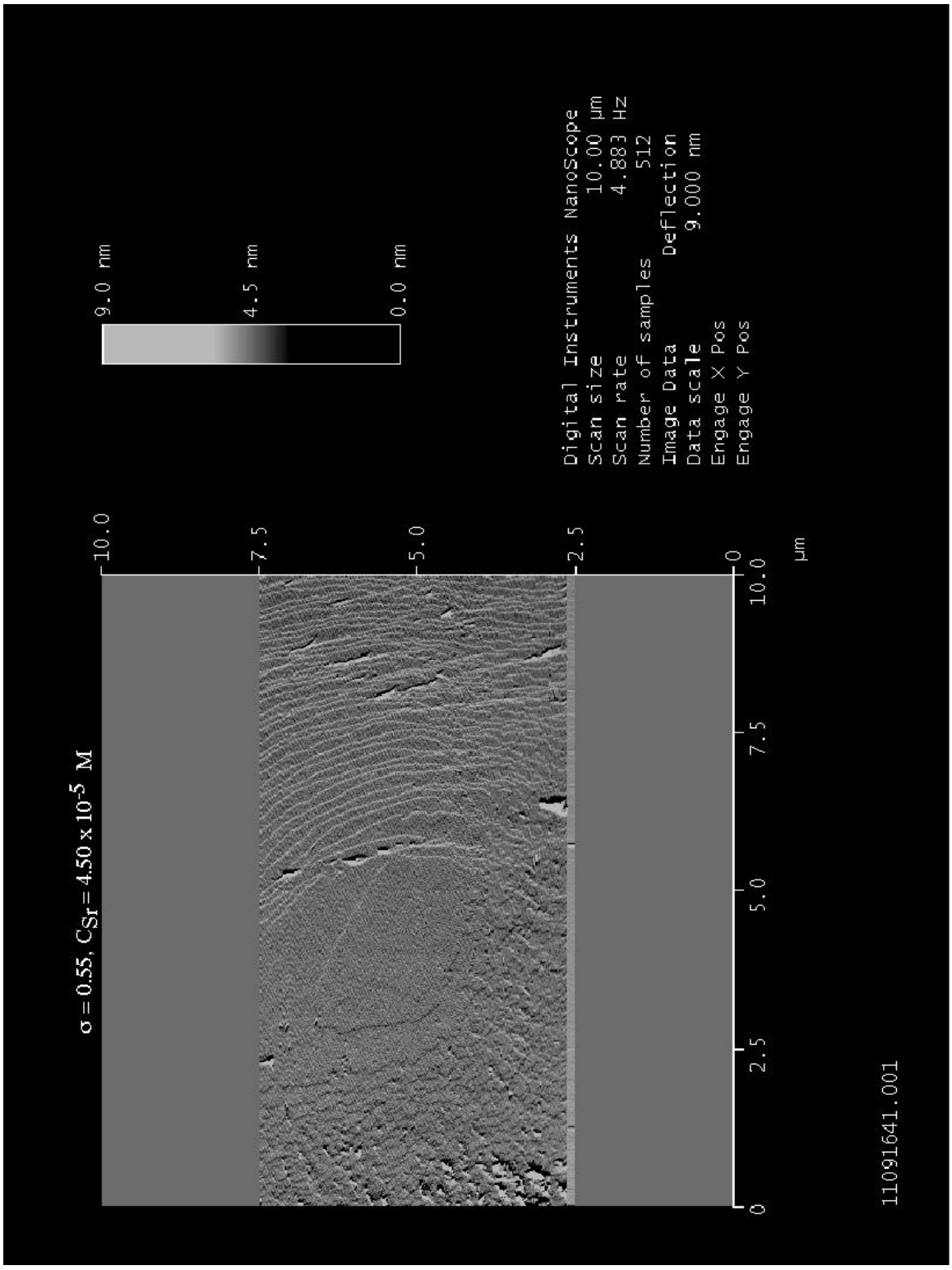
σ = 0.55, C_{Sr} = 4.50 x 10^{-5} M
9.0 nm
4.5 nm
0.0 nm
Digital Instruments NanoScope
Scan size 10.00 µm
Scan rate 4.883 Hz
Number of samples 512
Image Data Deflection
Data scale 9.000 nm
Engage X Pos
Engage Y Pos
10.0
7.5
5.0
2.5
0
0
2.5
5.0
7.5
10.0
µm
11091641.001

Darren Wilson

Department of Geological Sciences
4044 Derring Hall
Virginia Polytechnic Institute and State University
Blacksburg, Virginia 24061
Email: dsw@vt.edu
Voice: 540.231.8074

Education

2001 – Present	**Master of Science, Geochemistry** Virginia Polytechnic Institute & State University Thesis Project: Nanoscale Effects of Strontium on Calcite Growth: A Baseline for Understanding Biomineralization in the Absence of Vital Effects
2001	40-hour OSHA HAZWOPER training certification
1993 – 1998	**Bachelor of Science, Earth and Atmospheric Sciences** Georgia Institute of Technology Concentration in Environmental Chemistry

Work Experience

Research Scientist and Teaching Assistant
Virginia Polytechnic Institute & State University, Blacksburg, VA
2001 - Present

- Experimental research using in situ Fluid Cell Atomic Force Microscopy to observe mineral surface-fluid interactions.
- Protocol development and problem solving for AFM experiments.
- Offline analysis of AFM images to calculate kinetic and thermodynamic factors.
- Prepare high precision solutions.
- Perform various daily laboratory techniques and operate a variety of laboratory equipment.
- Poster session and Power Point presentations of research.
- Technical writing.
- Instructor for GEOL/GEOG 3114 Meteorology Laboratory.
- Prepare laboratory experiments and lesson plans.
- Grade laboratory exercises, quizzes, homework assignments and research papers.

Hydrogeologist
EnviroTrac, Ltd., Ronkonkoma, NY
2000-2001

- Project management including technical writing, system evaluation, field work scheduling and technical data analysis.
- Oversight of well installations, geophysical investigations, storm drain and cesspool cleaning and UST removals.
- Field work including Phase I Site Assessments, maintenance and monitoring of air sparge, soil vapor extraction and pump & treat systems, AS/SVE pilot testing, ground/potable water sampling and product recovery.
- Operate PID, GC, well gauging probe, manometer, laser surveying equipment, dissolved oxygen, temperature, pH, ORP and conductivity meters.

Product Specialist
Misonix, Inc., Farmingdale, NY
1998-1999

- Technical support, sales and applications assistance of ultrasonic laboratory equipment
- Managed a team of outside sales representatives to meet sales goals.
- Worked as project leader in the development of new technical manuals for ultrasonic equipment.

Student Assistant
Georgia Institute of Technology, Atlanta, GA
March 1998 – June 1998

- Website development and design.
- Use of Microsoft Office applications in daily administrative tasks.

Research Assistant
Volt Information Sciences, Inc., Syosset, NY
June 1997 – September 1997

- Maintenance and support supervisor for the Bell Atlantic Yellow Page database.

Computer Skills

Platforms	Applications	Internet	Programming
Windows	Word	Internet Explorer	HTML
Windows NT	Excel	Netscape	Fortran
Macintosh	Power Point		
UNIX	Outlook		
	Word Perfect		
	Adobe Photoshop		
	ACT!		
	Canvas		